

High-Efficiency Al(Ga)N Ultraviolet Optoelectronics and Integrated Photonics

by

Walter Jin Shin

A dissertation submitted in partial fulfillment
of the requirements for the degree of
Doctor of Philosophy
(Electrical and Computer Engineering)
in the University of Michigan
2022

Doctoral Committee:

Professor Zetian Mi, Chair
Assistant Professor Parag Deotare
Associate Professor Emmanouil Kioupakis
Professor Pei-Cheng Ku

Walter J. Shin

walterjs@umich.edu

ORCID iD: 0000-0002-6914-5940

© Walter J. Shin 2022

Acknowledgments

First, I truly want to thank my doctoral advisor, Professor Zetian Mi, for all the support and guidance. I started working with him in mid-2017 as a Ph.D. student, and for years he has taken care of me, not only limited to the research but also my personal life. Among all the projects I joined, he was always welcome to have in-depth discussions and gave me excellent advice that broadened my knowledge and understanding of this field. Furthermore, his financial and physical support helped me realize the theoretical ideas into practical devices. I am lucky to meet him as my doctoral advisor and truly respect his passion for research.

I want to thank the members of my dissertation committees – Professor Pei-Cheng Ku, Professor Emmanouil Kioupakis, and Professor Parag Deotare. Regarding my research, they were grateful collaborators in several projects, and their valuable suggestions helped me conduct future works.

I also want to express my gratitude to current and former group members who provided all the knowledge, skills, and efforts that helped me to finish the Ph.D. degree. I enjoyed working with early mentors, including Dr. Xianhe Liu, Dr. David Laleyan, Dr. Ayush Pandey, and Dr. Yuanpeng Wu. From them, I learned a lot of techniques and knowledge that were directly related to my research. Other group members who joined with me or after helped me expand my research area and broaden my insight on this field by collaborating with several works and performing the experiments together. I want to thank Dr. Ping Wang, Dr. Yi Sun, Dr. Debabrata Das, Dr. Tinh Tran, Dr. Ding Wang, Dr. Baowen Zhu, Eric Reid, Kishwar Mashooq, Heewoo

Kim, Yakshita Malhotra, Majid Aalizadeh, Ishtiaque Navid, Chiyo Ahn, Boyu Wang, Zhenwei Ye, Dr. Wan Jae Dong, Peng Zhou, Nick Pant, Chan Ho Soh, Yongbum Park, Yongjin Ma, and Yixin Zhao. Especially, I had a great time with Kishwar Mashooq, who came to Ann Arbor and started his Ph.D. with me. I enjoyed the days when we took the classes together and performed the research, which helped me settle and adapt to a new circumstance.

To achieve fascinating results in this fast-paced research area, collaborators are necessary. I want to give my special thanks to Moe Soltani from Raytheon BBN, who guided me and trained me to become a theoretically and experimentally expert on a photonic integrated circuit. Along with Prof. Mi, his passionate support in many aspects made me push forward the work with confidence and realize the ideas much faster than they should be. Also, I would like to thank Dr. Jiseok Gim, Suk Hyun Sung, and Professor Robert Hovden from the Materials Science and Engineering Department at the University of Michigan for their contributions.

Talking about my Ph.D. life, it is not an exaggeration to say that I spent several years in Lurie Nanofabrication Facility, which provides the best service based on skilled engineers and the latest fabrication equipment. Tool engineers maintained and calibrated all equipment in perfect condition, which helped me achieve fascinating results. I am grateful to Dr. Sandrine Martin, Dr. Pilar Herrera-Fierro, Dennis Schweiger, Vishva Ray, Brain Armstrong, Katharine Beach, Matthew Oonk, David Sebastian, Kevin Owen, Shawn Wright, Steven Sostrom, Jorge Barreda, Tony Sebastian, Samuel Edwards, Brandon Woo. I am also grateful to Ying Qi at the X-Ray Micro-Analysis Laboratory for training and helping me to operate the X-ray diffraction equipment.

I would also like to thank all the friends I made in Ann Arbor, especially those who went through the Ph.D. course together. They always gave me the mental support and entertained me

whenever I struggled with the research or others. Without their help, I couldn't overcome all the adversity I faced and finish my Ph.D.

Most of All, I would like to thank my family and my girlfriend as much as I can. The ocean separation could not stop their love, and despite that we couldn't see each other for a long time, we were always together. Their endless love and support helped me withstand and overcome all the hardship I faced, and their trust in my decision made me push forward with confidence.

Table of Contents

Acknowledgments.....	ii
List of Tables	ix
List of Figures	x
List of Appendices	xv
Abstract.....	xvi
Chapter 1 Introduction	1
1.1 III-Nitride Semiconductor	1
1.1.1 Impact of Polarization Field in Optical Devices	4
1.1.2 Polarization-Induced Tunnel Junctions	5
1.2 Light Emitting Diodes (LEDs)	7
1.3 AlGaIn based UV LEDs and Challenges.....	9
1.3.1 Low Internal Quantum Efficiency.....	10
1.3.2 Inefficient P-type Doping	11
1.3.3 Electron Overflow due to Asymmetric Charge Carrier Transport	15
1.3.4 Low Light Extraction of TM-Polarized Light	16
1.4 III-N Semiconductor based Photonic Integrated Circuit and Its Challenges	18
1.5 Mechanism of Microring Resonator (MRR).....	22
1.6 Electro-Optic Modulator Based on MRR.....	25
1.7 Dissertation Overview.....	27
Chapter 2 Methods	30
2.1 Overview	30

2.2 Molecular Beam Epitaxy (MBE)	30
2.3 Optical Characterization Techniques	31
2.3.1 Photoluminescence Spectroscopy	31
2.3.2 Spectroscopic Ellipsometry	32
2.4 Structural Characterization Techniques	33
2.4.1 X-Ray Diffraction.....	33
2.4.2 Scanning Electron Microscopy.....	34
2.5 Light Emitting Diode Characterization Techniques.....	35
2.5.1 Current-Voltage Measurement	35
2.5.2 Electroluminescence Spectroscopy	35
2.5.3 LED Power Measurement	36
2.6 Microring Resonator and Modulator Characterization Techniques	36
2.6.1 Transmission Characterization of Microring Resonator	36
2.6.2 Electro-Optic Modulation Measurement in Frequency Domain	37
Chapter 3 High-Efficiency Tunnel Junction AlGaIn UV LEDs	38
3.1 Author Contribution and Copyright Disclaimer.....	38
3.2 Introduction	38
3.3 Epitaxy of UV LED Structures	41
3.4 Characterization of the UV LED structure.....	43
3.5 Tunnel Junction Design Optimization and Characterization	44
3.6 Summary	51
Chapter 4 Photonic Crystal Tunnel Junction Deep UV LEDs with Enhanced Light Extraction Efficiency	53
4.1 Author Contribution and Copyright Disclaimer.....	53
4.2 Introduction	53
4.3 Device Structure and Photonic Crystal Simulation.....	56

4.4 Device Fabrication and Measurement.....	59
4.5 Summary	62
Chapter 5 Ultrahigh Q Microring Resonator Using a Single Crystal AlN on Sapphire Platform	64
5.1 Author Contribution and Copyright Disclaimer.....	64
5.2 Introduction	64
5.3 Characterization, Design and Fabrication of Microring Resonator	66
5.4 Measurement of Demonstrated Microring Resonator	70
5.5 Summary	72
Chapter 6 Demonstration of Green and UV Wavelengths High Q Aluminum Nitride on Sapphire Microring Resonators Integrated with Microheaters	73
6.1 Author Contribution and Copyright Disclaimer.....	73
6.2 Introduction	73
6.3 Characterization, Design and Fabrication	74
6.4 Transmission Characterization of Demonstrated Microring Resonators	77
6.5 Summary	81
Chapter 7 Enhanced Pockels Effect AlN Microring Resonator Modulator Based on AlGa _N /AlN Multiple Quantum Wells.....	83
7.1 Author Contribution and Copyright Disclaimer.....	83
7.2 Introduction	83
7.3 Material Growth and Characterization	86
7.4 Design and Fabrication of Microring Resonator Modulator	88
7.5 Experimental Result	93
7.6 Summary	100
Chapter 8 Summary and Future Work	101
8.1 Summary	101
8.2 Overview and Perspective on Al(Ga)N based Optoelectronics and Integrated Photonics	103

8.3 Future Work	105
8.3.1 Mode-locked Frequency Comb Based on AlN Microring Resonator	105
8.3.2 Broadband IR to Visible Up-conversion based on III-N Semiconductors	108
8.3.3 Investigation of Enhanced Nonlinearity of III-N Semiconductors.....	109
Appendices.....	110
Appendix A Fabrication Procedure for AlGaIn Epilayer LEDs	111
Appendix B Fabrication Procedure for AlN Microring Resonator and Modulator	114
Bibliography	123

List of Tables

Table 1-1: Material Properties of wurtzite III-N semiconductors [3-6].....	2
Table 3-1: List of tunnel junction LED structures.	42
Table 4-1: List of refractive indices for tunnel junction deep UV LED structure	58
Table 6-1: Parameter values for calibrating resonance characteristics at green and UV wavelengths.....	80
Table 7-1: Specifications of regrown MQWs on the AlN samples.....	88
Table 7-2: Parameter values to extract $\chi(2)$ of Sample A, B, and bare AlN at telecom wavelength	96
Table 7-3: Parameter values to extract $\chi(2)$ of Sample C and bare AlN at 780nm wavelength .	99

List of Figures

Figure 1.1: (a) Bandgap and lattice constants of III-N semiconductors [1]. (b) Schematic of wurtzite crystal structure [2].	1
Figure 1.2: Polarization direction and sheet charge density for AlGa _N /Ga _N heterostructure with different crystal polarities. For Ga (Al)-face: (a) AlGa _N on Ga _N heterostructure with relaxed AlGa _N . (b) AlGa _N on Ga _N heterostructure with tensile strained AlGa _N . (c) Ga _N on AlGa _N heterostructure with compressive strained Ga _N . For N-face: (d) AlGa _N on Ga _N heterostructure with relaxed AlGa _N . (e) AlGa _N on Ga _N with tensile strained AlGa _N . (f) Ga _N on AlGa _N heterostructure with compressive strained Ga _N [7]	3
Figure 1.3: Electronic band structure of QW under applied bias condition [6]......	5
Figure 1.4: Energy band diagram of a typical p-n junction (top) and a polarization-induced tunneling p-n junction (bottom) [13].	6
Figure 1.5: Schematic of typical LED [15]......	7
Figure 1.6: Plot of EQE of UV LEDs vs. emission wavelengths [23].	10
Figure 1.7: The effect of dislocation density on maximum IQE at different wavelengths [25]. ..	11
Figure 1.8: Formation energies and ionization level for the studied defect in (a) Ga _N for the Ga-rich case and (b) AlN for the Al-rich case [31].	12
Figure 1.9: Formation enthalpies of Mg _{Ga} and Mg _{Al} of AlGa _N films (a) in bulk and (b) on the surface of AlGa _N film with different Al compositions [24, 32]......	13
Figure 1.10: Activation energy of Mg acceptor dopant for different Al composition AlGa _N [33].	14
Figure 1.11: Optical transition between valence bands to conduction band at the Γ point of (a) AlN and (b) Ga _N [46]......	16
Figure 1.12: (a) Cross-section of stripe PSS after inductive coupled plasma dry etching and LED full structure [47]. (b) LED with surface roughness. (c) Schematic of UV LED with reflective contact and PSS [51]......	17
Figure 1.13: Applications for UV/Vis PIC platform [57]......	18

Figure 1.14: Comparison of AlN and other wide bandgap materials for PIC platform [57].	19
Figure 1.15: EO coefficient (r_{13} and r_{33}) for different materials; AlN [65-67], GaN [73], LiNbO3 [74-81], GaN/AlGaN MQWs [71, 72] and AlGaN/AlN MQWs (This work, discussed in Ch.7).	21
Figure 1.16: (a) Schematic of all-pass microring resonator with the time constant of round-trip loss (τ_i) and coupling loss (τ_c). (b) Example of transmission characteristics of microring resonator.	22
Figure 1.17: Variation of $ T ^2$ at resonance wavelength as a function of Q_L/Q_i .	25
Figure 1.18: Simulated electric-field distribution induced by the ground-signal-ground electrode.	26
Figure 1.19: Example of the transmission spectrum of MRM under different bias conditions.	27
Figure 2.1: The schematic of reflection high-energy electron diffraction (RHEED) operation [91].	31
Figure 2.2: Schematic of the PL process with direct and indirect bandgap materials [92].	32
Figure 2.3: Spectroscopic ellipsometry technique [93].	33
Figure 2.4: (a) Mechanism of XRD experiment [94]. (b) A Rigaku SmartLab XRD system.	34
Figure 2.5: Measurement setup for MRR transmission characteristics.	37
Figure 2.6: Measurement setup for MRM frequency response measurement.	37
Figure 3.1: (a) Schematic illustration of the tunnel junction LED structures. (b) Simulated equilibrium band diagram for a representative LED using a 5nm GaN layer. The different layers used in the structure are labeled and shown with different colors.	41
Figure 3.2: (a) HAADF-STEM overview of cross-sectional AlGaIn multilayers shows the complete device structure. (b) The high-resolution HAADF-STEM of the p-AlGaIn/GaN/n-AlGaIn tunnel junction shows crystalline epitaxial growth with sharp interfaces for enhanced hole injection by tunneling. (c) Atomic-resolution HAADF-STEM of Al _{0.6} Ga _{0.4} N quantum wells coupled to Al _{0.85} Ga _{0.15} N barriers with sharp epitaxial interfaces for carrier confinement.	43
Figure 3.3: (a) I-V characteristics of tunnel junction LED samples A and B, with 2.5 nm GaN layer width and different thicknesses, 50 nm, and 150 nm, respectively, of the top n ⁺ -AlGaIn contact layer. (b) I-V characteristics of samples B, C, and D grown with the same thickness of top n ⁺ -AlGaIn but different GaN layer widths of 2.5 nm, 5 nm, and 10 nm, respectively. Variations of (c) EQE and (d) WPE with injected current density, for samples B, C, and D.	45
Figure 3.4: I-V characteristics of an optimized tunnel junction LED from sample E with a GaN layer thickness of 5 nm and top n ⁺ -AlGaIn contact layer thickness ~480 nm.	48

Figure 3.5: (a) Electroluminescence spectra measured at different injection currents for a representative tunnel junction LED. The inset shows an electroluminescence spectrum measured at 25 A/cm ² current density with the intensity in log scale. (b) Variations of peak position (red circles) and spectral linewidth (black squares) vs. injected current density.	49
Figure 3.6: (a) Variations of (b) EQE and (c) WPE with injected current density for an LED from sample E.	50
Figure 4.1: Schematic of (a) tunnel junction deep UV LED heterostructure and (b) nanowire photonic crystal integrated deep UV LED. (c) Top view of the nanowire photonic crystal.	56
Figure 4.2: Contour plot of average LEE as a function of nanowire diameter (<i>d</i>) and lattice constant (<i>a</i>) at nanowire height (<i>L</i>)=240nm. (b) Variations of the average LEE vs. nanowire height (<i>L</i>) for a constant nanowire diameter (<i>d</i>) of 160nm and lattice constant (<i>a</i>) of 320nm.	59
Figure 4.3: 45°-tilted view SEM image of hexagonal nanowire photonic crystal arranged in a triangular lattice with nanowire diameter (<i>d</i>) of 160nm and lattice constant (<i>a</i>) of 320nm.	60
Figure 4.4: (a) Current-voltage characteristics for both with and without incorporation of nanowire photonic crystal. (b) Electroluminescence spectra were measured with different current injections. Inset shows no other defect-related emission. (c) Top emitting optical power density measurement using 10kHz repetition rate and 1% duty cycle.	61
Figure 4.5: (a) External quantum efficiency (EQE) and (b) wall-plug efficiency (WPE) as a function of injected current density.	62
Figure 5.1: (a) Schematic of AlN-on-Sapphire ring resonator coupled to an external waveguide with a pulley coupling scheme. (b) Cross-section of the electric mode profile of an AlN-on-Sapphire ring resonator with an internal radius of 60 μm, width of 3 μm, and height of 1 μm. (c) Mode profile of the optical waveguide at the pulley coupling region, with a waveguide width of 1100 nm. The waveguide width in the pulley region is adjusted to be phase-matched to the mode of the resonator. (d) Calculated coupling Q-factor vs. the pulley angle for different waveguide resonator gaps.	67
Figure 5.2: (a) AFM images of AlN grown on a sapphire show an RMS roughness of ~0.2 nm. (b) XRD (0002) and (1012) plane rocking curves for AlN on sapphire samples.	68
Figure 5.3: (a) Schematic illustration of the fabrication process for the AlN-on-sapphire microring resonator. (b) SEM image of the devices after SiO ₂ etching at step 5 in (a). (c) SEM image of the devices after AlN etching at step 6 in (a). (d) SEM image of the fabricated AlN-on-sapphire microring resonator and associated waveguide after SiO ₂ removal at step 7 in (a). (e) Enlarged SEM image for the red box area in (d), showing the resonator's vertical and smooth sidewall after etching.	69
Figure 5.4: (a) and (b) SEM images of trench refill capability for silane-based and TEOS-based SiO ₂ deposition, respectively. The dimension of the trench is 1 μm deep and 1 μm wide.	70

Figure 5.5: (a) Spectrum of the resonators near 1550 nm, where a strong coupling is observed. The gap between the waveguide and the resonator is 800 nm, the pulley angle is 20 degrees, and the waveguide width at the pulley region is 1100 nm. (b) A zoomed view of one of the resonances at the solid red circle in (a), wherein the resonance shows the coupling between the degenerate CW and CCW modes of the resonator due to sidewall roughness scattering. A fitting of this spectrum to theoretical spectrum using coupled-mode theory shows intrinsic Q for both CW and CCW modes..... 71

Figure 5.6: Previously reported Q-factor of AlN-on-sapphire microring resonators [60, 186, 190, 205, 213]. 72

Figure 6.1: (a) Measured refractive index and (b) photoluminescence spectrum of AlN-on-sapphire. (c) Schematic illustration of microring resonators with thermal heater. (d) Mode profiles of the ring resonator and bus waveguide at pulley coupling region. The width of the bus waveguide and ring resonator are adjusted to satisfy the phase-matching condition. (e) Cross-section of microring resonator. 76

Figure 6.2: SEM image of (a) a fabricated AlN-on-sapphire microring resonator and (b) magnified image of waveguide sidewall. (c) Optical microscope image of demonstrated microring resonators. Five microring resonators with different widths are coupled to one bus waveguide. 77

Figure 6.3: (a) Normalized transmission characteristic using tunable laser around 780nm with two different bias voltages, 0V and 5V. (b) Measured resonance wavelength shift as a function of applied voltage square showing a linear relationship. 79

Figure 6.4: (a) Normalized transmission characteristic as a function of calibrated wavelength offset at (a) green wavelength (532nm fixed laser) and (b) UV wavelength (fixed 369.5nm laser). The red dash line shows the simulated transmission characteristic based on coupled-mode theory. The inset of each figure shows the optical microscope image at the resonance condition, where the arrow shows laser input..... 80

Figure 6.5: (a) Measured step response of the NiCr microheater and magnified view of (b) rise time and (c) fall time response..... 81

Figure 7.1: Pockels coefficient (r_{13} and r_{33}) for different materials; Polymers [240-243], LiNbO₃ [74-81, 244], GaN [73], GaN/AlGa_N MQWs [71, 72], AlN [65-67] and our study (AlGa_N/AlN MQWs). 84

Figure 7.2: (a) Schematic illustration of regrown AlGa_N/AlN MQWs on AlN-on-sapphire. (b) High-resolution XRD patterns of 2θ/omega scan for samples of with (w.) MQWs and without (w/o) MQWs along the (0002) direction. The satellite diffraction peaks can be observed from the MQW sample, which indicate a good periodicity of MQWs. (c) Photoluminescence spectrum of 3 regrown samples. (d) Simulated band structure of regrown AlGa_N/AlN MQWs on AlN. The inset shows the built-in field in the QW and barriers due to spontaneous and piezoelectric polarization. 86

Figure 7.3: (a) Schematic illustration of demonstrated MRMs and (b) magnified ring resonator. (c) and (d) show the cross-sections of MRMs at telecom (Sample A&B) and $\sim 780\text{nm}$ (Sample C) wavelengths, respectively. Thin Al_2O_3 is included for Sample C to increase the coupling efficiency. (e) and (f) show the simulated E_z of each layer, along the dashed line shown in the (c) and (d), respectively..... 91

Figure 7.4: SEM images of (a) fabricated microring resonator on Sample A (left) and C (right). Insets show the magnified images of each waveguide sidewall. (b) Optical microscope images of fabricated MRMs on Sample A and C..... 92

Figure 7.5: (a) Normalized transmission spectrum for a microring resonator made on Sample A (see Table 7-1 for the specifications) and (b) magnified transmission spectrum near 1554nm . $\lambda_{3\text{dB}}$ shows the input wavelength used for frequency response measurement shown in Fig. 7.6. (c) Resonance wavelength shifts as a function of applied voltage of MRMs on Sample A (blue) and bare AlN with SiO_2 cladding (dashed black). The inset shows simulated mode profile of ring resonator on Sample A. (d) Calculated effective refractive index variation of MRMs on Sample A (blue), bare AlN with SiO_2 cladding (dashed black), and bare AlN with Al_2O_3 cladding (dashed red) as a function of applied electric field (E_z). Bare AlN MRM with Al_2O_3 cladding (dashed red) shows a negative relationship between applied electric field and effective index variation. 95

Figure 7.6: Frequency response of EO modulation at telecom wavelength (Sample A) with a 3dB bandwidth of 27 GHz. The laser wavelength is parked at the full-width half-maximum of the resonator..... 97

Figure 7.7: (a) Normalized transmission spectrum for a microring resonator made on Sample C (see Table 7-1 for the specifications) and (b) magnified transmission spectrum near 768.7nm . (c) Resonance wavelength shifts as a function of the applied voltage of MRMs on Sample C (red) and bare AlN (black dash). Inset shows the simulated mode profile of ring resonator on Sample C. (d) Calculated effective refractive index variation of MRMs on Sample C (red) and bare AlN (dashed black) as a function of applied electric field (E_z). 98

Figure 8.1: Reported Q_{int} of AlN [60, 186, 190, 205], SiN [253-256] and LiNbO_3 [58, 257-262] MRR..... 104

Figure 8.2: Schematic of principle for Kerr comb generation [189]. 106

Figure 8.3: (a) Normalized transmission characteristic of demonstrated microring resonator and (b) magnified transmission near 1557.47 107

Figure 8.4: SEM image of previously demonstrated selective area growth nanowires with different designs [277]. 109

List of Appendices

Appendix A Fabrication Procedure for AlGaN Epilayer LEDs 111

Appendix B Fabrication Procedure for AlN Microring Resonator and Modulator 114

Abstract

Al(Ga)N semiconductors have attracted tremendous research interest due to their wide direct bandgap that enables passive/active optoelectronic, photonic, and quantum functionalities in UV, visible, and infrared wavelengths. In addition, high-power handling properties and intrinsic 2nd and 3rd order nonlinear optical characteristics make AlGaN a unique platform for photonic integrated circuit (PIC) at telecom and UV/visible wavelengths. Despite the attractive characteristics, the performance of AlGaN-based optoelectronic devices has been severely limited by the presence of large densities of defects/dislocations in the active region, extremely inefficient p-type doping, and poor light extraction due to predominantly TM polarized emission for Al-rich AlGaN. For the emerging AlN-based PIC platform, the growth and fabrication processes have remained underdeveloped prior to this work. Furthermore, the 2nd order nonlinear susceptibility of Al(Ga)N required for wavelength conversion and basis of linear electro-optic effect, Pockels effect, is relatively weak, limiting the performance of photonic and quantum functionalities. In this thesis, we focus on the design and development of optoelectronic and photonic devices based on high Al composition Al(Ga)N on a sapphire substrate, including deep UV light-emitting diodes (LEDs) and microring resonators (MRRs).

Regarding deep UV LEDs, we investigate the epitaxy, design, fabrication, and characterization of high-efficiency deep UV LEDs emitting at ~265nm, which can be utilized for sterilization of pathogens such as current COVID-19 and preventing future pandemics. First, we apply polarization-engineered tunnel junctions to improve hole injection efficiency. The demonstrated bottom-emitting UV LEDs with an optimized GaN tunnel junction show the

maximum EQE of 11%, the highest value reported at this wavelength. We also investigate and improve the light-emitting efficiency (LEE) by utilizing photonic crystal (PhC) as a diffraction grating layer. For this study, we investigate the top-emitting UV LEDs where LEE is the dominant limiting factor. The demonstrated LED shows EQE of 5.4% and WPE of 3.5%, which are approximately 2.5 times higher than identical LED structures without PhC.

Next, we focus on the AlN-based microring resonator, one of the widely investigated components of PIC platform offering unique features due to cavity-based resonance characteristics. Initially, the fabrication process is optimized to provide ultra-high Q AlN MRRs using single-crystal AlN on the sapphire platform. The demonstrated AlN MRR showed intrinsic Q (Q_{int}) of 2.8×10^6 at telecom wavelength, the highest Q_{int} reported for fully etched AlN-on-sapphire resonators. Subsequently, we extend our focus to shorter wavelengths, especially green wavelength ($\sim 532\text{nm}$), to demonstrate and characterize MRRs where tunable lasers are less available. Here, we utilize a new technique, thermo-optic tuning with an integrated microheater, to characterize the demonstrated microring resonator, which shows a Q_{int} of 147,000, first measured Q_{int} at this wavelength. Finally, we achieve significantly enhanced Pockels coefficient of AlN by utilizing AlGaN/AlN multiple quantum wells (MQWs). The demonstrated AlN microring resonator modulators (MRMs) with MQWs show ~ 2.16 times and ~ 1.56 times higher effective Pockels effect than MRMs without MQWs at telecom and $\sim 780\text{nm}$ wavelengths, respectively. These enhancements can be attributed to an order of magnitude higher Pockels coefficient of the AlGaN/AlN MQWs than that of AlN.

This work provides a viable and unique path to realize high-efficiency deep UV LEDs extended to other wavelengths. In addition, based on demonstrated high-Q microring resonators

at UV to telecom wavelength along with enhanced Pockels effect, our studies show a new opportunity to achieve a high-performance monolithic PIC platform.

Chapter 1 Introduction

1.1 III-Nitride Semiconductor

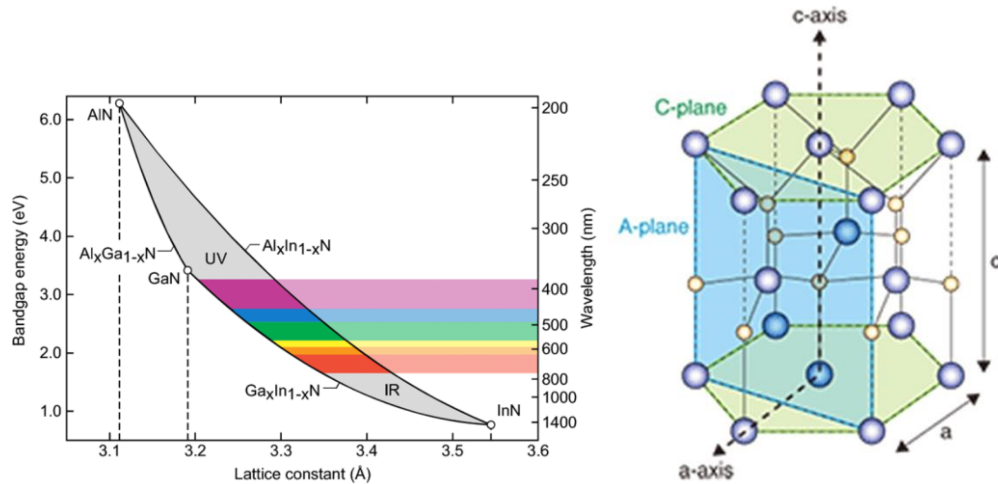


Figure 1.1: (a) Bandgap and lattice constants of III-N semiconductors [1]. (b) Schematic of wurtzite crystal structure [2].

III-Nitride (N) material system consists of InN, GaN, AlN, and their alloys, which are direct bandgap materials with bandgap covering from 0.7eV (InN) to 6.1eV (AlN), shown in Fig. 1.1 (a). These attractive characteristics allow III-N semiconductor to be a promising candidate for optoelectronics and photonics in a broad range of operation wavelengths, from UV to mid-infrared (IR). Recent studies have focused on high Al composition AlGaN which allows optoelectronic and photonic devices at UV wavelength where the application includes sensing, polymer curing, data storage, and quantum information processing. In addition, UV-B and UV-C light can damage the DNA, which can be used for sterilization for pathogens, such as current COVID-19 and future pandemics.

Another unique property of III-N semiconductors is spontaneous and piezoelectric polarization. In this thesis, we focus on III-N semiconductors with wurtzite crystal phase, which has a noncentrosymmetric crystal structure, shown in Fig. 1.1(b), providing a strong spontaneous polarization field. The direction of the spontaneous polarization field depends on the polarity of the crystal, which lies along the c-axis of the wurtzite crystal. The spontaneous polarization points towards the substrate for metal-polar crystal, whereas, for N-polar crystal, the spontaneous polarization points towards the surface. The polarization field is also affected by piezoelectric polarization, which can be manipulated based on significant lattice mismatch of the different binary compounds, and it can be intentionally utilized for specific applications. The direction of piezoelectric polarization is aligned with the spontaneous polarization for tensile strain, whereas opposite for compressive strain, shown in Fig. 1.2. The material properties of III-N semiconductors are listed in Table 1-1.

Table 1-1: Material Properties of wurtzite III-N semiconductors [3-6].

Property	AlN	GaN	InN
Bandgap E_g (eV)	6.1	3.44	0.7
a (nm)	0.3112	0.3189	0.3545
c (nm)	0.4978	0.5185	0.5718
Piezoelectric Coefficient e_{33} (C/m²)	1.46	0.73	0.97
Piezoelectric Coefficient e_{31} (C/m²)	-0.6	-0.49	-0.57
Spontaneous Polarization (C/m²)	-0.081	-0.029	-0.032
C_{11} (GPa)	396	367	223
C_{12} (GPa)	137	135	115
C_{13} (GPa)	108	103	92
C_{33} (GPa)	373	405	224

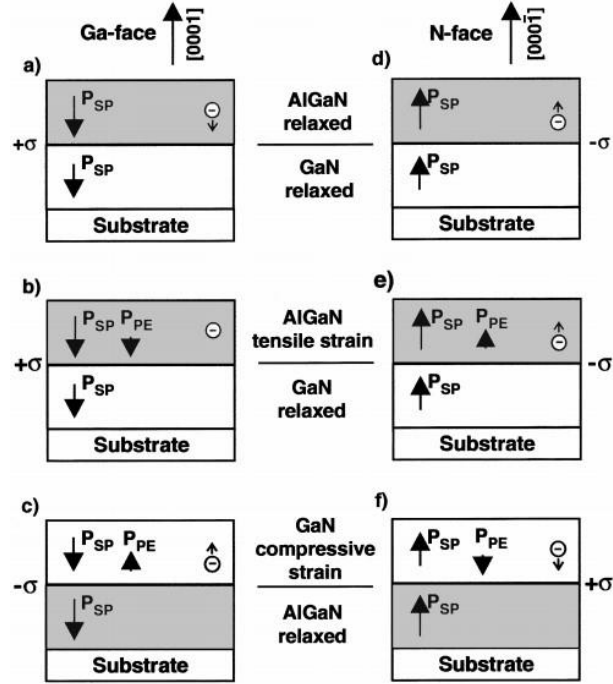


Figure 1.2: Polarization direction and sheet charge density for AlGaIn/GaN heterostructure with different crystal polarities. For Ga (Al)-face: (a) AlGaIn on GaN heterostructure with relaxed AlGaIn. (b) AlGaIn on GaN heterostructure with tensile strained AlGaIn. (c) GaN on AlGaIn heterostructure with compressive strained GaN. For N-face: (d) AlGaIn on GaN heterostructure with relaxed AlGaIn. (e) AlGaIn on GaN with tensile strained AlGaIn. (f) GaN on AlGaIn heterostructure with compressive strained GaN [7] .

Due to strong polarization, huge charge carrier densities at heterointerfaces are found following $\sigma = -\nabla \cdot \vec{P}$ (Gauss' Law) and result in the high built-in electric field of MV/cm order that can significantly impact the devices. Such large polarization fields also provide unique opportunities for device engineering. The magnitude of the built-in field (F) in the heterostructure can be given by,

$$F_w = \frac{P_b^{SP} + P_b^{PZ} - P_w^{SP} - P_w^{PZ}}{\epsilon_w + \epsilon_b(L_w/L_b)}, \quad (\text{Equation 1.1})$$

$$F_b = -\frac{L_w}{L_b} F_w, \quad (\text{Equation 1.2})$$

where ε is the static dielectric constant, L is the layer thickness, and P^{SP} is the spontaneous polarization. The subscript w and b represent quantum well (QW) and barrier, respectively. The piezoelectric polarization (P^{PZ}) for the biaxial strained layer can be calculated by,

$$P^{PZ} = 2(e_{31} - \frac{c_{13}}{c_{33}} e_{33}) \varepsilon_{||}, \quad (\text{Equation 1.3})$$

$$\varepsilon_{||} = (a - a_0)/a_0, \quad (\text{Equation 1.4})$$

where e is the piezoelectric coefficients and C is elastic constants, a_0 is the unstrained lattice constant, and a is the lattice constant of strained case. As listed in Table 1-1, the spontaneous polarization difference between AlN and GaN is huge, whereas the lattice constant difference is relatively small. This shows that for AlGaIn-based heterostructure, spontaneous polarization will act as a dominant factor. These unique characteristics need to be well understood, which can affect the performance of optoelectronic and photonic devices. In addition, it can be used as a technique to improve performance and overcome the challenges of different devices and applications, which will be described in the following chapters.

1.1.1 Impact of Polarization Field in Optical Devices

Figure 1.3 shows the energy band diagram of QW under applied bias condition and quantum-confined Stark effect (QCSE), where electrons and holes are separated toward opposite sides. A similar phenomenon occurs in III-N QWs due to a high polarization field attributed to spontaneous polarization and strain-induced piezoelectric polarization. This internal polarization field can affect the carrier dynamics and radiative efficiency under carrier injection conditions [6, 8-10]. Typically, shown in Fig. 1.3, it shows a narrow effective bandgap where the emission of electroluminescence (EL) or photoluminescence (PL) show redshift from those of a “stress-free”

bulk layer. However, under a high carrier injection regime, the polarization field is compensated by screening effect reducing the effect of polarization field and start to show blue-shift in emission wavelength [6].

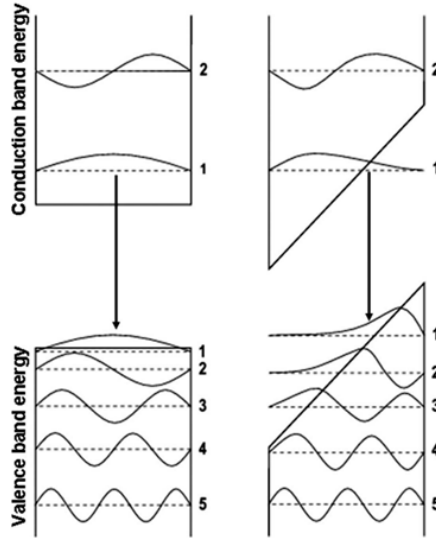


Figure 1.3: Electronic band structure of QW under applied bias condition [6].

1.1.2 Polarization-Induced Tunnel Junctions

Interband tunneling of electrons is based on the tunneling barrier height and tunneling barrier thickness. Therefore, III-N semiconductors offer poor tunneling probability due to wide bandgap and limited impurity doping efficiency. However, the presence of a giant built-in polarization field in III-N heterostructures can be exploited to realize interband tunneling in p-n junction [11-14] even with limited impurity doping conditions. Typically, the polarization-induced tunnel junction is composed of double heterostructures where the intermediate layer shows significant band-bending, shown in Fig. 1.4. and polarization dipoles compensate the ionized impurity charges and shrink the effective depletion width, allowing the interband tunneling. In this

thesis, this technique will be used to improve the hole injection efficiency of deep UV LEDs in Chapters 3 and 4.

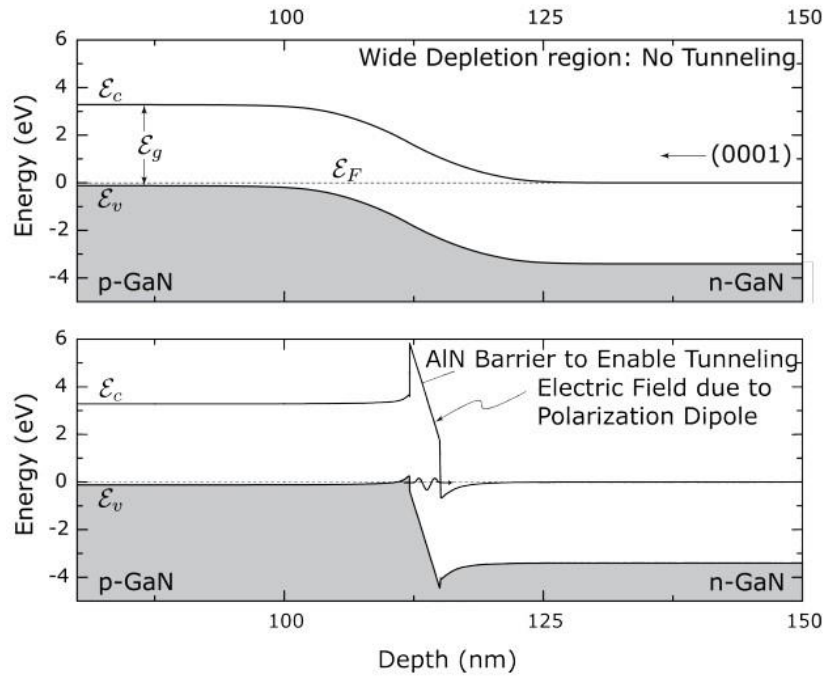


Figure 1.4: Energy band diagram of a typical p-n junction (top) and a polarization-induced tunneling p-n junction (bottom) [13].

1.2 Light Emitting Diodes (LEDs)

LEDs are solid-state light sources that convert electrical energy into optical energy using charge carrier recombination. Typically, LEDs consist of a p-n junction designed to maximize the radiative recombination in the active region where holes and electrons are injected from the p-doped and n-doped region, respectively, shown in Fig. 1.5. The emitted spectrum of LEDs relies on spontaneous emission, which is incoherent and offers a relatively broad full-width half maximum (FWHM). The emission characteristic depends on the bandgap of semiconductors where radiative recombination occurs, generally in the active region, which can be tailored by changing the composition of the active region or using QCSE.

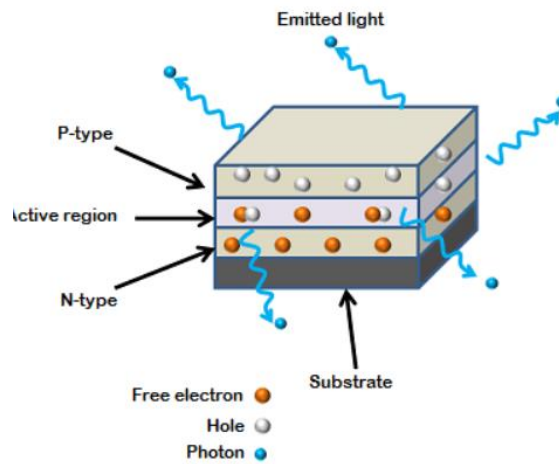


Figure 1.5: Schematic of typical LED [15].

The key parameters used to describe LEDs' efficiency are described below.

The internal quantum efficiency (IQE) is generally used to show the material quality, which is defined as,

$$IQE = \frac{\text{Photons generated in active region}}{\text{Electrons injected to active region}}, \quad (\text{Equation 1.5})$$

Since radiative recombination depends on the bandgap, material composition, and quality (defect/dislocation densities) of the active region, optimizing the growth condition for the active region is necessary to maximize the IQE.

Another parameter is injection efficiency (IE) which shows the ratio of carriers injected in the active region, where others will be recombined outside of the active region or become leakage current. The IE can be defined as,

$$IE = \frac{\text{Electrons injected into active region}}{\text{Electrons injected into device}}, \quad (\text{Equation 1.6})$$

After radiative recombination, not all the generated photons are emitted from the devices due to internal reflection and absorption. The light extraction efficiency (LEE) shows the ratio of photons that escape from the device and are detected, which can be defined as,

$$LEE = \frac{\text{Photons emitted out of the device}}{\text{Photons generated in the device}}, \quad (\text{Equation 1.7})$$

Based on these parameters, LED performance is generally represented by external quantum efficiency (EQE), which is the ratio of photons emitted to the total carriers injected, defined as

$$EQE = IQE \times IE \times LEE, \quad (\text{Equation 1.8})$$

as well as the wall-plug efficiency (WPE) which is the energy conversion efficiency of electrical to optical power, defined as

$$WPE = \frac{\text{Power of optical output}}{\text{Power of electrical input}}, \quad (\text{Equation 1.9})$$

1.3 AlGaN based UV LEDs and Challenges

From the late 1980s, intense research into III-N semiconductors started based on tremendous effort on heteroepitaxial growth, mostly on sapphires substrate. Significant progress in all growth-related areas such as substrate, epitaxy, doping, and ternary alloy had been made from these early efforts, opening a new path for III-N device technologies. After a decade of research on GaN, its other ternary alloys, InGaN and AlGaN, were also developed, which enabled the growth of high-quality single-crystal materials by using a low-temperature nucleation layer [16]. After successfully growing single-crystal GaN, p-type GaN was realized using low-energy electron beam treatment of the magnesium-doped material, followed by thermal annealing [17, 18]. These advancements in growth trigger the tremendous development in GaN-based LEDs and laser diodes.

With the significant development of GaN-based visible wavelength LEDs, many research groups started to focus on shorter wavelengths, UV wavelengths, where the application includes air/water purification, sterilization, UV cure, UV light source, and biomedical equipment [19, 20]. Regarding UV light sources, AlGaN semiconductor is promising material due to several advantages such as small footprint, high electrical efficiency, electron-photon conversion rate, and eco-friendly fabrication process compared to conventional UV light sources. In this regard, tremendous research has been done on AlGaN quantum well/dot UV LEDs [21, 22]. However, the external quantum efficiency (EQE) of AlGaN quantum well LEDs operating in the UV-C band is below 10%, significantly lower than GaN-based blue LEDs, which often show $EQE > 50\%$.

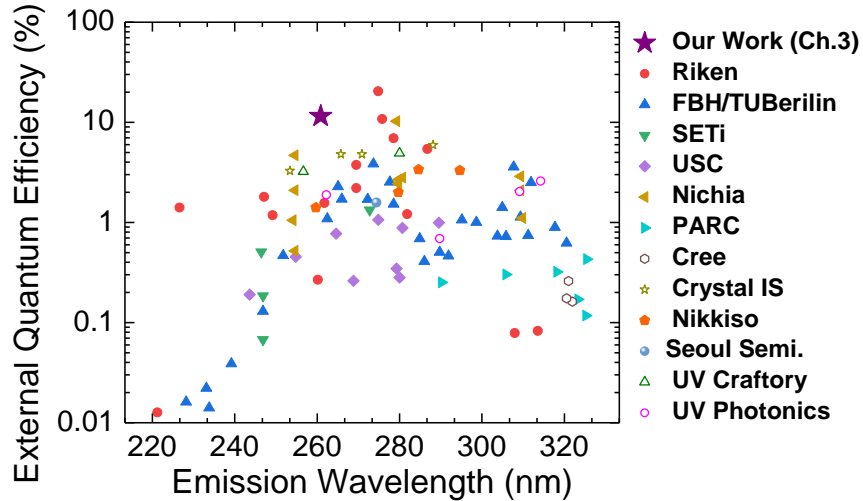


Figure 1.6: Plot of EQE of UV LEDs vs. emission wavelengths [23].

Figure 1.6 shows the EQE of reported UV LEDs where wavelengths around 275nm showed ~20% and decreased sharply with decreasing wavelength. The followings are the factors that degrade the EQE of AlGa_N UV LEDs: low internal quantum efficiency, inefficient p-type doping, low light extraction for TM polarization emission, and asymmetric charge carrier transport, which will be described in the following chapters.

1.3.1 Low Internal Quantum Efficiency

Dislocations and defects usually act as the nonradiative recombination centers, which lower the internal quantum efficiency and act as leakage paths, directly affecting the device performance. The main contribution of high dislocation density (DD) is due to the large lattice mismatch between Al(Ga)_N layers and the commonly used substrates such as sapphire and Si. In addition, GaN cannot be used for the buffer layer since it will cause tensile strain resulting in cracks on the surface [24], making it hard to realize high-quality Al(Ga)_N epi-layer. In addition, during the AlGa_N growth, the Al atom has a low migration rate compared to the Ga atom, leading

to the formation of Al-rich islands and further increasing DD and reducing IQE. Figure 1.7 shows the relationship between the maximum IQE and dislocation density (DD) in AlGaIn MQWs [25].

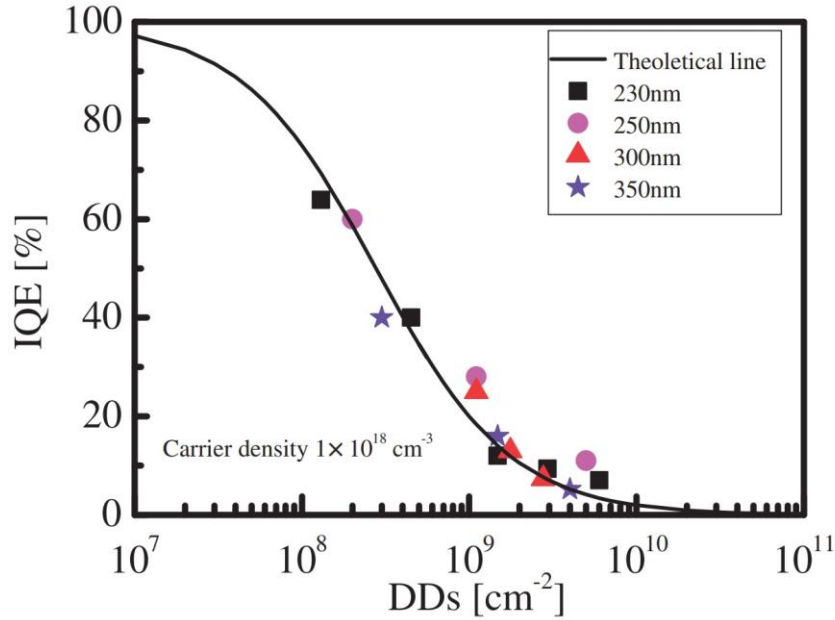


Figure 1.7: The effect of dislocation density on maximum IQE at different wavelengths [25].

To overcome the limitation, several techniques have been investigated to improve the material quality of AlN, including interlayers [26] and utilizing nano-patterned substrates (NPSS) [27]. Recently, my colleague Dr. David Laleyan grew a thin and high-quality AlN layer with a smooth surface directly on sapphire substrate with a multi-cycle anneal-regrowth technique [28].

1.3.2 Inefficient P-type Doping

To achieve high-performance UV LEDs, efficient charge carrier injection is required for both n- and p-contact layers. For III-N semiconductors, n-type doping can be easily done by Si having electron concentration higher than $1 \times 10^{18} \text{cm}^{-3}$ even with high Al composition AlGaIn [29].

However, achieving high hole concentration for AlGaN semiconductors is extremely hard, especially with high Al composition AlGaN. For p-type doping, Be, Mg, and Zn can be the candidates whose activation energy are 60meV, 160meV, and 370meV, respectively, in GaN [24]. Despite low activation energy, Be is poisonous and easily becomes an interstitial atom due to its small size, compensating acceptors [30]. Therefore, Mg is the most widely used acceptor for AlGaN semiconductors, however, there are still difficulties to achieve efficient p-type doping.

First, AlGaN has strong self-compensating defects such as nitride vacancies (V_N) and oxygen incorporation, which act as donors, and this compensation gets stronger with the increase of hole concentration. As shown in Fig. 1.8 (a) and (b), these donor-like native defects have very low formation energy when the fermi level gets closer to the valence band maximum [31]. This self-compensation can be reduced by lowering defect density with optimized growth cond.

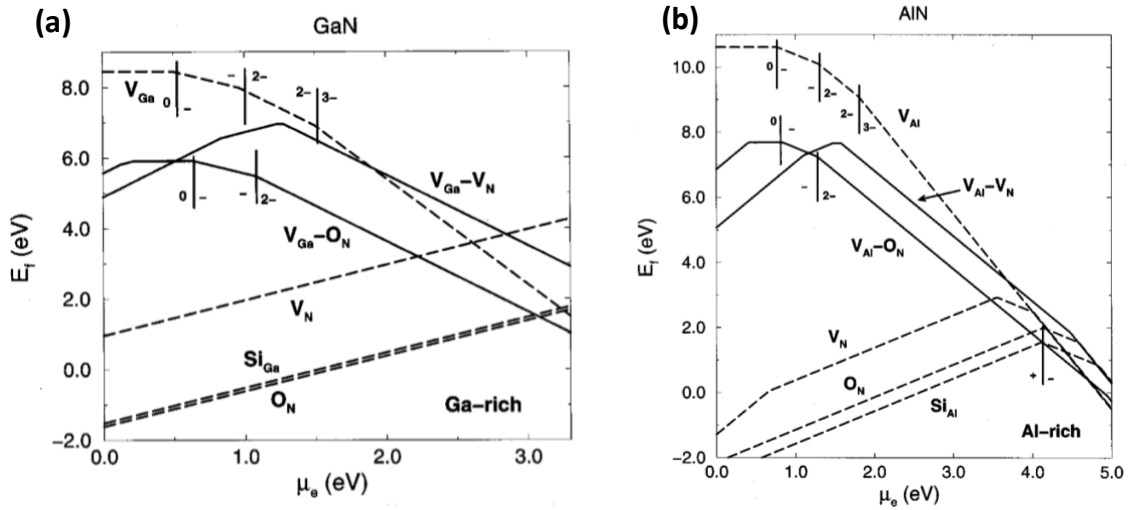


Figure 1.8: Formation energies and ionization level for the studied defect in (a) GaN for the Ga-rich case and (b) AlN for the Al-rich case [31].

Secondly, Mg has low solubility in AlGaN due to large formation enthalpy. The Mg solubility (C) can be defined as,

$$C = N_{sites} e^{-\Delta H_f / k_B T}, \quad (\text{Equation 1.10})$$

where C is Mg solubility, N_{sites} is the number of sites in AlGaN for Mg incorporation, k_B is Boltzmann constant, ΔH_f is enthalpy, and T is temperature [24]. To act as an acceptor, Mg must substitute Ga or Al. However, due to the large formation enthalpy, shown in Fig. 1.9 (a), the solubility of Mg is low, and the situation becomes worse with higher Al composition. One technique to increase solubility is to use the surface effect, which has negative enthalpy shown in Fig. 1.9 (b) [32]. This can be realized by using nanostructures that provide a larger surface-to-volume ratio than bulk structure. Also, based on Eq. (1.10), a higher growth temperature helps to increase the Mg solubility.

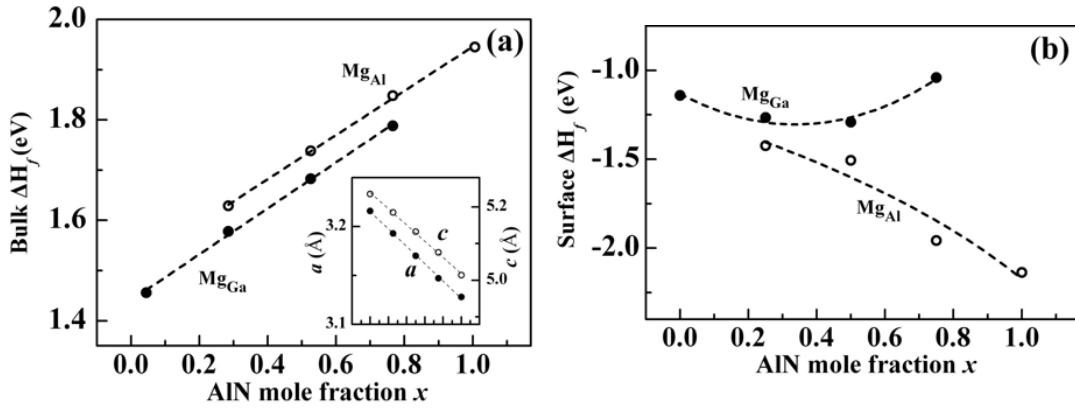


Figure 1.9: Formation enthalpies of Mg_{Ga} and Mg_{Al} of AlGaN films (a) in bulk and (b) on the surface of AlGaN film with different Al compositions [24, 32].

Finally, Mg has very high activation energy in AlGaN, especially with high Al composition, ranging from 160 meV to 600 meV, shown in Fig. 1.10. Due to high activation energy, it is very hard to achieve high hole concentration at room temperature and limits the optoelectronic device performance.

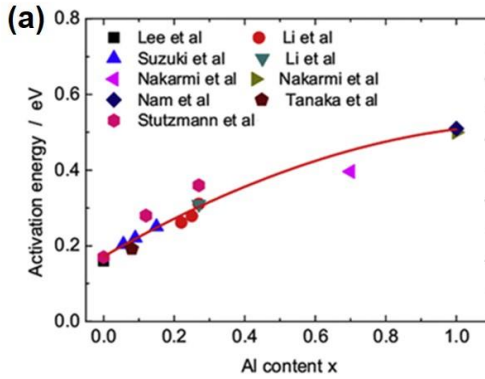


Figure 1.10: Activation energy of Mg acceptor dopant for different Al composition AlGaIn [33].

As an alternative, due to inefficient p-type doping with high Al composition AlGaIn, thin p-type GaN is commonly used as the p-type contact layer, providing efficient hole injection. However, due to its narrow bandgap, it absorbs the photons generated from the AlGaIn active region, lowering the efficiency of demonstrated UV LEDs and increasing the demand for a transparent p-type contact layer. Significant investigation has been done to realize low-resistivity p-AlGaIn layer such as high nitrogen overpressure during growth [34], delta-doping [35], utilizing superlattices [36], metal-modulation epitaxy [37], and polarization-induced doping [38, 39]. One of my colleagues, Ayush Pandey, recently demonstrated record low resistivity with high Al composition AlGaIn layer using metal-semiconductor junction assisted epitaxy with MBE system. Metal-semiconductor junction-assisted epitaxy can be done by tuning the surface Fermi level during the growth, where efficient p-type conduction can be achieved [40]. In this thesis, all the following growth on UV AlGaIn LEDs are done utilizing metal-semiconductor junction assisted epitaxy for p-type doping, which allows us to have more freedom to optimize the LED structures.

1.3.3 Electron Overflow due to Asymmetric Charge Carrier Transport

Despite improved p-type doping with high Al composition AlGa_N, it is still incomparable to n-type doping with high mobility achieved by Si as a dopant [29]. This asymmetric charge carrier transport results in electron overflow in the active region and leads to poor injection efficiency [41].

To overcome electron overflow, electron blocking layers (EBLs) with high bandgap layer or superlattice structure [42-44] are introduced to confine the electron in the active region. Typically, p-type EBL is included after the active region, however, it can degrade the hole injection due to band offset in the valence band between EBL and active. Previously, my colleague Ayush and I investigated different types of EBLs in our AlGa_N LEDs to improve the injection efficiency and balance the asymmetric charge carrier transport [45]. We observed that n-doped EBL before the active region shows the highest EQE, where electron injection is reduced while hole injection is maintained.

Another approach is to use tunnel junction as a p-type contact layer, providing efficient hole injection, low contact resistivity, and improved current spreading simultaneously. As mentioned in Chapter 1.1.2, it is challenging to achieve interband tunneling due to the wide bandgap and limited impurity doping efficiency of the AlGa_N layer. However, with improved p-type doping based on metal-semiconductor junction assisted epitaxy technique and the use of polarization-engineering, which reduces the barrier height, we were able to demonstrate high-efficiency tunnel junction UV LED at 265nm, which will be discussed in Chapter 3.

1.3.4 Low Light Extraction of TM-Polarized Light

The polarization of generated light can be either transverse-electric (TE) or transverse-magnetic (TM) based on the band structure of the active region where e-field (E) direction for TE polarized emission is $E \perp c$, whereas TM polarized emission has $E \parallel c$. For III-N semiconductors, the valance band maximum is split into the heavy hole (HH), light hole (LH), and crystal-field split-off hole (CH) subbands by the crystal field near the Γ point in the Brillouin zone [46]. It is generally accepted that transition between the conduction band and HH/LH generates TE polarized emission, whereas transition between the conduction band and CH generates TM polarized emission. Based on the theoretical calculation, due to the difference in crystal-field splitting energy of GaN and AlN, the subband for valance band maximum is different with GaN and AlN, shown in Fig. 1.11 [46].

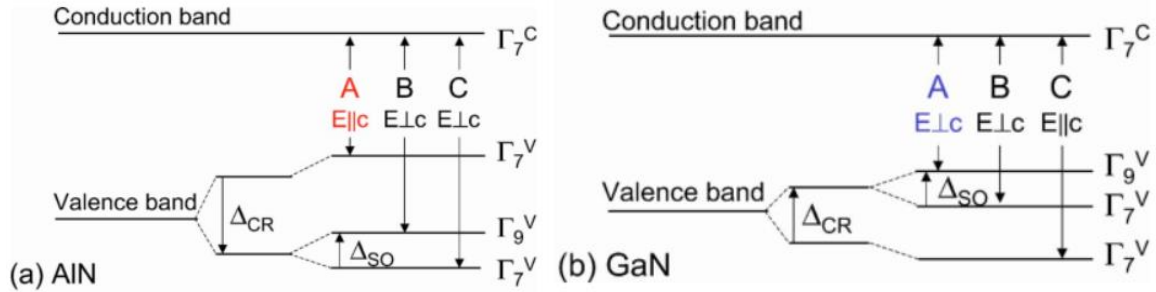


Figure 1.11: Optical transition between valence bands to conduction band at the Γ point of (a) AlN and (b) GaN [46].

With low Al composition, since the HH/LH subbands are on the top of the valance band, TE polarized emission dominates TM polarized emission. However, with high Al composition, CH subband rises whereas HH/LH subbands fall, resulting in TM polarized emission. The ratio of TE/TM polarized emission is also determined by Al composition and the width of quantum well/barrier, strain, etc., which all affect the band structure. Since TM polarized emission has an

E-field parallel to the c-axis, for c-orientated AlGaIn, the photon is trapped in the structure, making it hard to extract. Therefore, light extraction efficiency decreases with higher Al composition LEDs.

To improve LEE, several techniques are utilized, such as patterned sapphire substrate (PSS) [47] and surface roughness [48] to reduce total internal reflection, shown in Fig. 1.12 (a) and (b). Other approaches include removing substrate [49, 50] and using reflective contacts [51], shown in Fig. 1.12 (c). Photonic crystal (PhC) is another promising technique to improve LEE, manipulating the optical guiding mode. In Chapter 4, we utilized PhC with a top-down approach to improve the LEE of UV LED at 265nm and demonstrated top-emitting LED with 2.5 times higher LEE than planar UV LEDs without PhC.

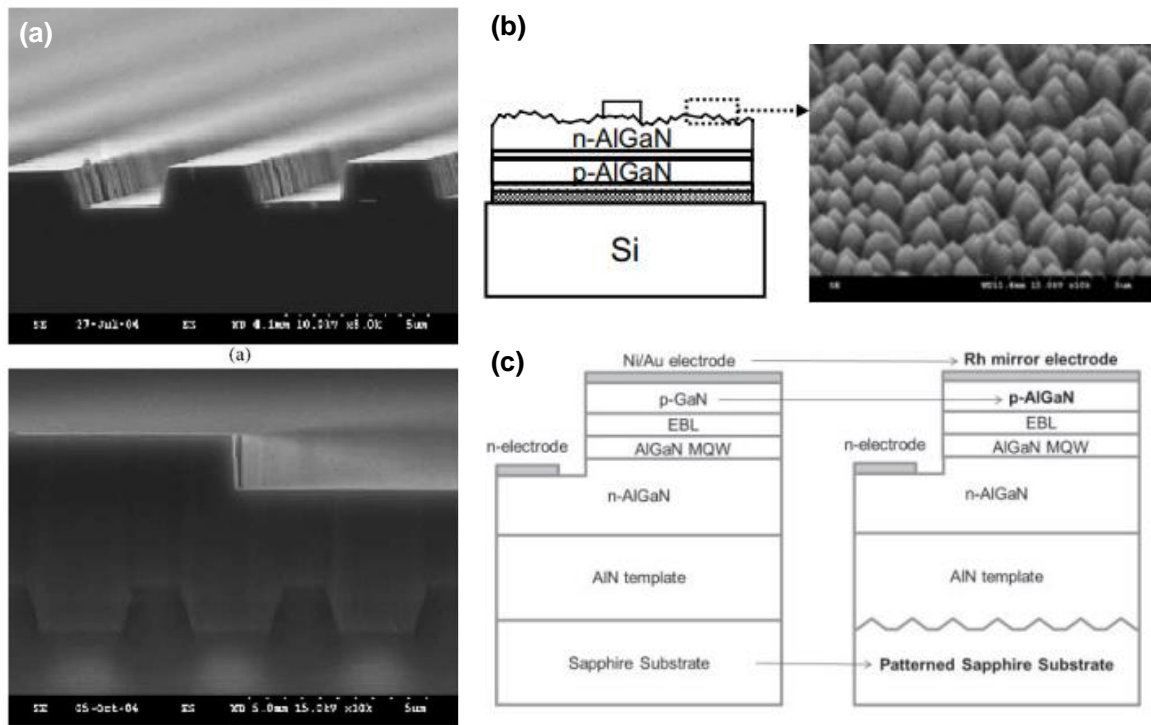


Figure 1.12: (a) Cross-section of stripe PSS after inductive coupled plasma dry etching and LED full structure [47]. (b) LED with surface roughness. (c) Schematic of UV LED with reflective contact and PSS [51].

1.4 III-N Semiconductor based Photonic Integrated Circuit and Its Challenges

A photonic integrated circuit (PIC) is a device that is composed of multiple photonic components with the operating signal of optical wavelength and provides functions for signal processing on a chip-scale. Up to now, based on the success of Si photonics, tremendous research development has been made on silicon-on-insulator (SOI) platforms. With mature Si fabrication technology, compatibility with electronic devices, and ultra-compact photonic device based on high refractive index contrast makes Si photonics more attractive. However, due to the narrow indirect bandgap (1.1eV), the operating wavelength is limited to above 1100nm, and it is hard to realize active devices such as light emitters. Furthermore, Si has a centrosymmetric crystal structure, which does not show the second-order nonlinearity required for wavelength conversion and linear electro-optic (EO) effect, Pockels effect. In this regard, other wide bandgap platforms with intrinsic Pockels effect are investigated for UV/vis PIC platform, which offers various optical applications, including underwater communication [52], optogenetics [53], UV spectroscopy [54, 55], and quantum information processing [56], shown in Fig. 1.13.

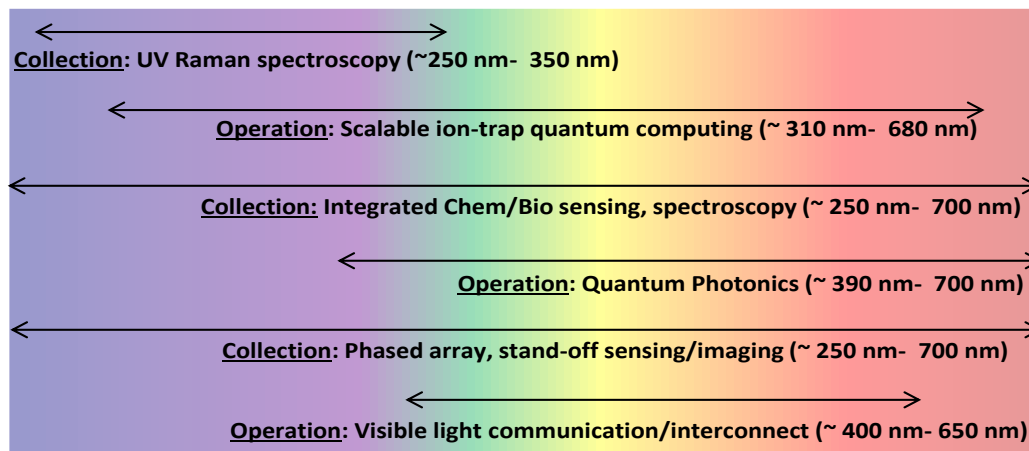


Figure 1.13: Applications for UV/Vis PIC platform [57].

One of the most developed wide bandgap materials for visible PIC platforms is LiNbO_3 which provides a wide transparency window (400nm~5 μm) with large second-order nonlinear susceptibility ($\chi^{(2)}=30\text{pm/V}$) [58]. However, due to the photorefractive effect, it is not suitable for handling high optical power, which is necessary for nonlinear optic applications, and it becomes more severe at UV wavelength [59]. Another candidate for a visible PIC platform is SiN, which has the advantages of utilizing mature Si manufacture technology and compatibility with the complementary-metal-oxide-semiconductor (CMOS) platform. Nonetheless, SiN shows high optical loss below 470nm down to UV wavelength due to silicon incorporation during SiN growth [60, 61], and it is not suitable for fast control of optical signals. In this regard, wide bandgap materials that provide low optical losses and handle high optical power at UV/vis wavelength are required. The characteristics of different wide bandgap materials for UV/vis PIC platforms are shown in Fig. 1.14.

	Diamond	GaN	AlN	SiO₂	Si₃N₄
refractive index @ $\lambda = 500 \text{ nm}$	2.4	2.42	2.13	1.45	2.04
bandgap (nm)**	230	365	200	140	250
crystalline	yes	yes	yes	no	no
electro-optic coeff. (pm/V)	NA	~1	~1	NA	NA
thermo-optic coeff. (K^{-1})	10^{-6}	1.6×10^{-4}	3.6×10^{-5}	10^{-5}	2.5×10^{-5}
thermal conductivity ($\text{W.m}^{-1}.\text{K}^{-1}$)	2200	130	285	1.4	30
active integration	no	yes	yes	no	no
*: The data in this table are available in many references including Refs [1,9–11] cited here.					
**: Above the bandgap wavelength, the material starts to become transparent.					

Figure 1.14: Comparison of AlN and other wide bandgap materials for PIC platform [57].

Recently, AlN has emerged as a promising candidate for the UV/visible PIC platform due to its wide direct bandgap (~6.1eV) and attractive electrical and optical characteristics. The wide bandgap of AlN allows free of two-photon absorption above 400nm, making it suitable for a

wide range of applications at UV/vis wavelength. In addition, its noncentrosymmetric crystal structure provides both second (χ^2) and third (χ^3) order optical nonlinearities required for frequency mixing and the basis of EO effects. AlN also has high thermal conductivity (319W/mK) [62] and a small thermo-optic coefficient ($2.7 \times 10^{-5} \text{K}^{-1}$) [63], which is suitable to handle high optical power. Furthermore, unlike other wide bandgap materials, Al(Ga)N can demonstrate passive/active optoelectronic functionalities on the same platform [23], making it a promising platform for monolithic photonic integrated circuits.

However, despite the attractive characteristics of AlN, its Pockels effect is weak ($r_{11}, r_{13} \sim 1 \text{ pm/V}$) [64-67] compared to other traditional nonlinear optic materials such as LiNbO₃, shown in Fig. 1.15. Up to now, several efforts have been made to increase the EO effect in III-N semiconductors, such as utilizing quantum confined stark effect (QCSE) [68], applying external DC electric field along the optical axis to induce electric-field-induced second harmonic (EFISH) [69, 70]. Some studies utilize a high internal polarization field based on GaN/AlGaN superlattices which show 10 times higher Pockels coefficient than bare GaN, shown in Fig. 1.15, providing additional freedom for manipulating the EO effect [71, 72]. However, most studies are limited to GaN film, and it has remained unknown if the Pockels coefficient of AlN can be enhanced.

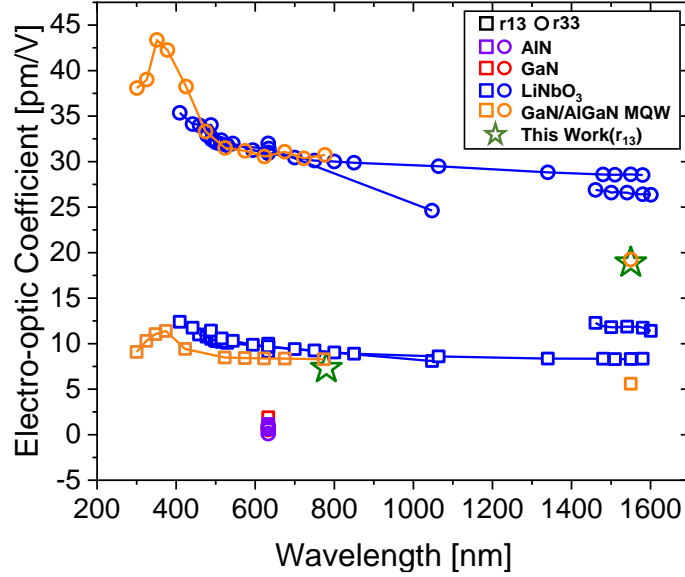


Figure 1.15: EO coefficient (r_{13} and r_{33}) for different materials; AlN [65-67], GaN [73], LiNbO₃ [74-81], GaN/AlGaN MQWs [71, 72] and AlGaIn/AlN MQWs (This work, discussed in Ch.7).

In Chapter 6-8, we will discuss about demonstrated high-Q AlN-based microring resonator (MRR) operating at UV, visible to telecom wavelengths. MRR is a widely used device in the PIC platform which shows unique features based on its cavity-based resonance characteristic. In addition, in Chapter 7, we investigate the enhanced Pockels effect in an AlN integrated photonic platform by utilizing AlGaIn/AlN MQWs regrown on top of the AlN layer on a sapphire substrate. In the following chapters, we will discuss the basic mechanisms of the microring resonator, and some representative parameters used in the thesis.

1.5 Mechanism of Microring Resonator (MRR)

This thesis focuses on an all-pass microring resonator composed of a ring resonator and a bus waveguide shown in Fig. 1.16(a).

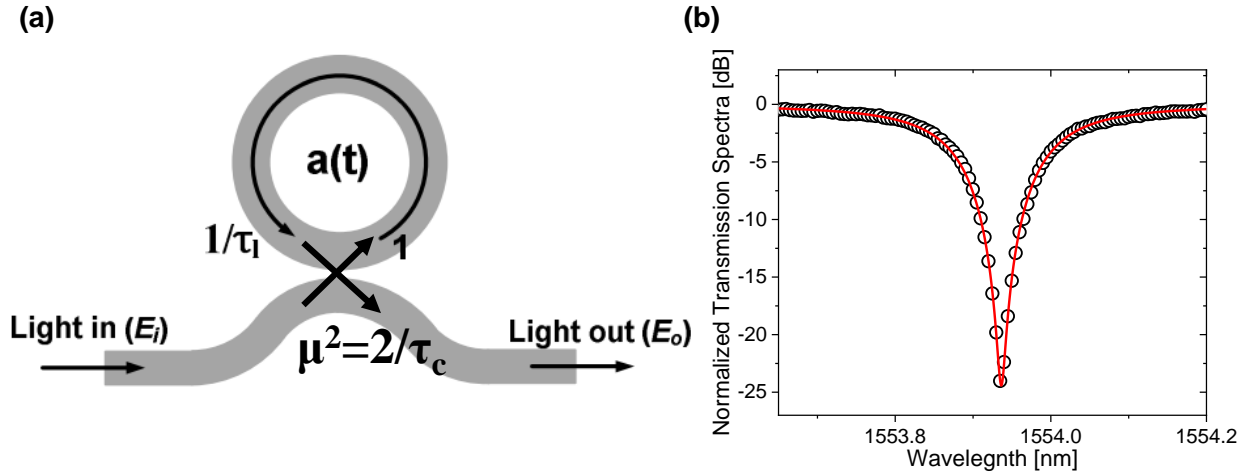


Figure 1.16: (a) Schematic of all-pass microring resonator with the time constant of round-trip loss (τ_l) and coupling loss (τ_c). (b) Example of transmission characteristics of microring resonator.

The resonance wavelength that has the in-phase condition and constructive interference in the ring resonator is defined as,

$$m\lambda_{res} = n_{eff}L, \quad (\text{Equation 1.11})$$

where λ_{res} is resonance wavelength, n_{eff} is the effective refractive index of the ring resonator, and L is the effective length or perimeter of the resonator. The integer m represents the mode number, the number of standing waves in the ring waveguide for one round-trip. Figure 1.16(b) shows an example of the transmission spectrum of a microring resonator. Due to phase shift, while coupling between bus waveguide and ring resonator, the output transmission power at resonance wavelength shows a minimum value. The dynamic of microring resonator can be represented by coupled-mode theory (CMT),

$$\frac{d}{dt} a(t) = \left(j\omega_0 - \frac{1}{\tau_L} \right) a(t) - j\mu E_i(t), \quad (\text{Equation 1.12})$$

$$E_o(t) = E_i(t) - j\mu a(t), \quad (\text{Equation 1.13})$$

where $a(t)$ is energy amplitude in the ring resonator, τ_L is decay time constant for $a(t)$, μ represents the coupling efficiency from input optical field to $a(t)$, and ω_0 is resonance angular frequency. E_o and E_i represent the input and output optical electric fields. The total decay time constant (τ_L) is defined as,

$$\frac{1}{\tau_L} = \frac{1}{\tau_i} + \frac{1}{\tau_c}, \quad (\text{Equation 1.14})$$

where τ_i is the photon lifetime in the ring resonator due to optical loss and τ_c is the time constant of the rate of energy coupling between ring resonator and bus waveguide, shown in Fig. 1.16 (a). Assuming that reflection back into the bus waveguide is negligible, the ratio of the incident field and transmitted in the bus waveguide can be represented as,

$$\frac{E_o(\omega)}{E_i(\omega)} = \frac{\frac{j2(\omega-\omega_0)}{\omega_0} + \frac{1}{Q_i} - \frac{1}{Q_c}}{\frac{j2(\omega-\omega_0)}{\omega_0} + \frac{1}{Q_i} + \frac{1}{Q_c}}, \quad (\text{Equation 1.15})$$

where ω represents input frequency, Q_i represents intrinsic quality factor ($=\omega_0\tau_i/2$) which depends on material loss and scattering losses due to surface roughness. It is showing overall optical loss which can characterize the fabrication technologies and material system. Based on the intrinsic quality factor, propagation loss can be calculated with the following expression, $\alpha=10*\log_{10}(e)*2\pi n_g/(Q_i*\lambda)$ [dB/cm]. Q_c represents coupling quality factor which is defined as coupling ratio between ring resonator and bus waveguide,

$$Q_c = \omega_0 \frac{\text{Resonator Energy}}{\text{Optical Power Coupled to Bus Waveguide}} = \omega_0\tau_c/2, \quad (\text{Equation 1.16})$$

The relationship between Q_i , Q_c and total quality factor, loaded Q ($Q_L=\omega_0\tau_L/2$), is

$$\frac{1}{Q_L} = \frac{1}{Q_i} + \frac{1}{Q_c}, \quad (\text{Equation 1.17})$$

where Q_L can be easily extracted from the full width at half maximum (FWHM) of transmission spectrum from the following equation,

$$\Delta\omega_{FWHM} = \frac{\omega_0}{Q_L}, \quad (\text{Equation 1.18})$$

The ring resonators can be classified into three different operation regimes, based on the ratio of Q_i and Q_c , which shows unique characteristics: critical coupling, over-coupling, and under-coupling [82].

1. The case of $Q_i = Q_c$ is called critical coupling regime, where at the resonance wavelength, the transmission magnitude is zero and has a discontinuity in the phase response.
2. The case of $Q_i < Q_c$ is called the under-coupling regime, where the transmission at resonance wavelength is non-zero and FWHM of the transmission is narrower than the critical coupling condition and $Q_L > Q_i/2$.
3. The case of $Q_i > Q_c$ is called the over-coupling regime, where the transmission at resonance is non-zero, FWHM is wider than the critical coupling condition and $Q_L < Q_i/2$. This condition is used for low-loss all-pass phase filters.

Another useful equation that can be used to extract Q_i is transmission at resonance wavelength, which can be derived from Eq. (1.15),

$$|T(\omega_0)|^2 = \left| \frac{1-Q_i/Q_c}{1+Q_i/Q_c} \right|^2 = \left| \frac{2Q_L}{Q_i} - 1 \right|^2, \quad (\text{Equation 1.19})$$

Figure 1.17 shows a plot of Eq. (1.19), showing $|T|^2$ as a function of Q_L/Q_i [82]. The same $|T|^2$ value can be obtained with different values of Q_L/Q_i corresponding to the under-critical and over-critical coupling regimes. Therefore, coupling conditions must be determined before extracting Q_i which can be done by phase response or measuring different coupling condition devices such as different gaps or pulley angles.

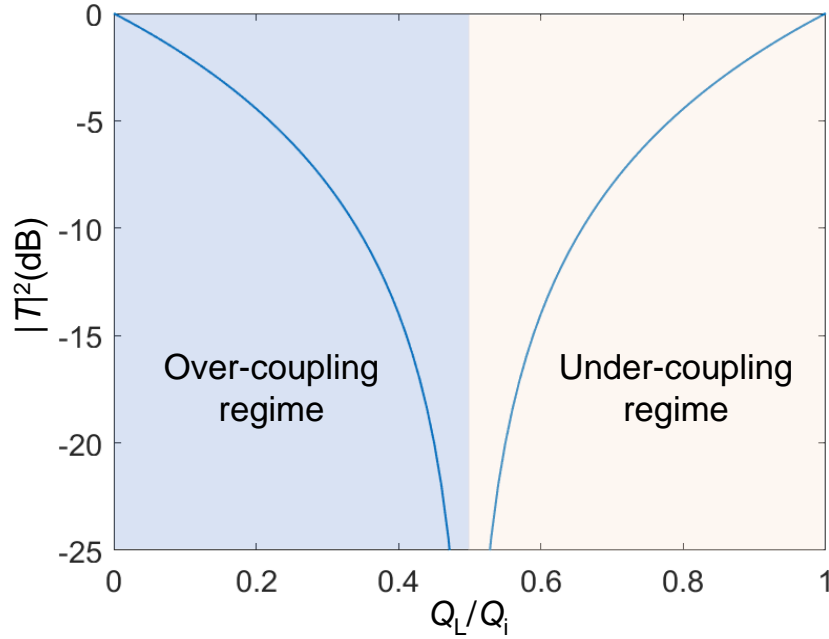


Figure 1.17: Variation of $|T|^2$ at resonance wavelength as a function of Q_L/Q_i .

Finally, free spectral range (FSR) represents the interval between resonance defined as,

$$FSR = \lambda_m - \lambda_{m+1} = \frac{\lambda^2}{n_g L}, \quad (\text{Equation 1.20})$$

where n_g represents the group index,

$$n_g = n_{eff} - \lambda \frac{dn_{eff}}{d\lambda}. \quad (\text{Equation 1.21})$$

All the parameters will be used to characterize the demonstrated AlN-based microring resonator in the following chapters.

1.6 Electro-Optic Modulator Based on MRR

The electro-optic modulator is an optical device with an optical signal modulated by the electro-optic effect, which changes the optical properties of materials under external electric-field conditions. The electro-optic effect can be subdivided into refractive index change or absorption change. In this thesis, we focus on the change of refractive index of material under

external electric field conditions. There are several ways to change the refractive index used for electro-optic modulator; Pockels effect (linear electro-optic effect), Kerr effect (quadratic electro-optic effect), plasma-dispersion effect, etc. Here, we focus on the Pockels effect of AlN to demonstrate a high-speed electro-optic modulator based on a microring resonator. As a noncentrosymmetric wurtzite crystal structure, AlN is a uniaxial material with a c-axis as an optical axis. It is categorized in 6 mm symmetry which has nonvanishing Pockels coefficient of r_{13} , r_{33} , and r_{15} . We focus on r_{13} and r_{33} , related to the out-of-plane electric field (E_z) since they show an order of magnitude higher value than r_{15} [64]. The refractive index variation based on out-of-plane electric field (E_z) with TE ($n_{x,y}$) and TM (n_z) polarized propagation mode is given by,

$$n_{x,y} = n_o - \frac{1}{2}r_{13}n_o^3E_z, \quad (\text{Equation 1.22})$$

$$n_z = n_e - \frac{1}{2}r_{33}n_e^3E_z, \quad (\text{Equation 1.23})$$

n_o and n_e are the ordinary and extraordinary refractive indices, respectively. The out-of-plane external field can be achieved by following the structure.

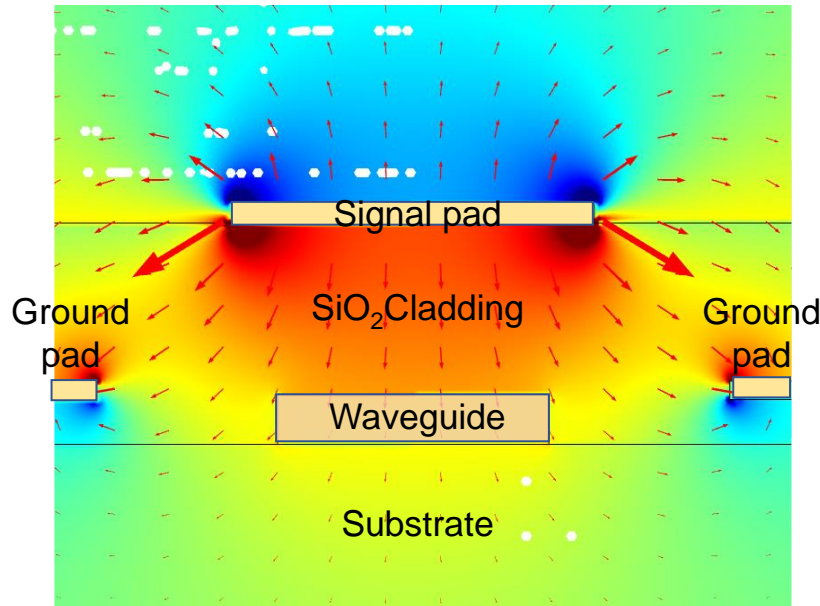


Figure 1.18: Simulated electric-field distribution induced by the ground-signal-ground electrode.

Following the Eq. (1.22) and (1.23), when the external electric field is applied on the microring resonator, the effective refractive index of the ring resonator changes and the transmission characteristic of ring resonator changes, as shown in Fig. 1.19, which can be used to modulate optical output signal. In Chapter 7, the ground-signal-ground (GSG) structure, shown in Fig. 1.18, will be used to apply an out-of-plane electric field in the resonator core.

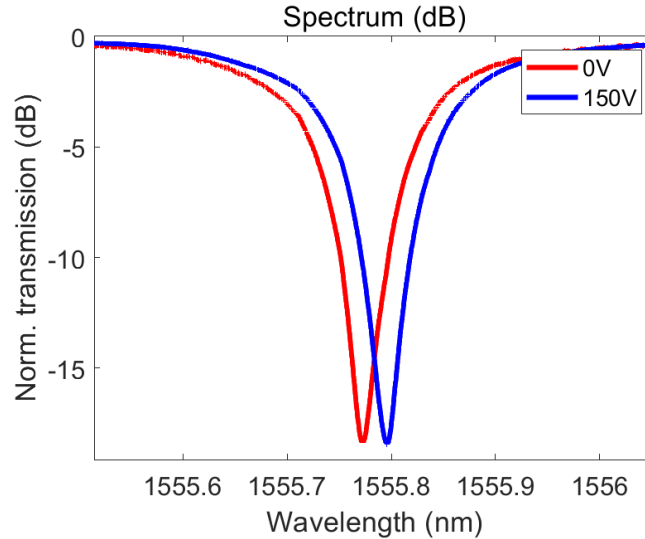


Figure 1.19: Example of the transmission spectrum of MRM under different bias conditions.

1.7 Dissertation Overview

The main objective of this dissertation is to understand the limitations and improve the performance of Al(Ga)N-based deep UV LEDs and photonic devices.

Chapter 2 describes an overview of the molecular beam epitaxial (MBE) system used to grow semiconductor structures and all the optical and structural characterization techniques used for characterizations. In addition, measurement setup and its operation used to characterize demonstrated UV LEDs and photonic devices are included.

Chapter 3 presents the work published in [83], a high-efficiency backside emitting UV LED operating at 265nm. Polarization-engineered tunnel junction structure is optimized to improve the hole injection efficiency. With 5nm GaN tunnel junction sandwiched between highly doped n-type and p-type AlGaIn layers, our demonstrated deep UV LED shows significantly improved I-V characteristics with EQE and WPE of 11% and 7.6%, respectively.

Chapter 4 reports the demonstration of top-emitting UV LED with enhanced LEE using PhC as a diffraction layer [84]. The optimized tunnel junction structure reported in Chapter 3 is used for efficient hole injection with emission at 267nm. Theoretically and experimentally, LEE is enhanced by nearly a factor of two with nanowire PhC structures where EQE \sim 5.4% and WPE \sim 3.5% are measured.

Chapter 5 presents the demonstration of ultra-high Q_{int} microring resonators utilizing single-crystal AlN on a sapphire substrate [85]. With an optimized fabrication process, a fully etched AlN MRR achieves a record high Q_{int} of 2.8×10^6 at the wavelength of 1550 nm (propagation loss: 0.13dB/cm).

Chapter 6 describes a new technique to characterize the demonstrated AlN microring resonator at green (532nm) and UV (369.5nm) wavelengths which are two important wavelengths for sensing and quantum information processing [86]. Due to the lack of high-performance tunable laser at these wavelengths, the Q-factor of these resonators are characterized based on the thermo-optic effect with integrated microheaters. We measure a record high Q_{int} of 147,000 (propagation loss: 7.3dB/cm) at 532 nm wavelength, and Q_{int} of 25,500 (propagation loss: 60.4dB/cm) at 369.5nm wavelength. In addition, thermal crosstalk between the adjacent resonators due to the high thermal conductivity of sapphire substrate is investigated.

Chapter 7 presents an enhanced Pockels effect by utilizing AlGaIn/AlN MQWs regrown on the AlN layer. This enhancement is attributed to the large built-in polarization field in the MQWs, which results in a higher second-order susceptibility in the MQW layer overlapping with the optical mode of the waveguiding device. The resonance shift due to Pockels effect is characterized by applied voltages and compared with the AlN MRM of similar dimensions but without MQWs. We observe enhanced resonance shift factors of 2.16 (at 1550nm) and 1.56 (at 780 nm) for resonators with MQWs compared to those without MQWs. Through a modal overlap analysis between the MQW layers and the optical mode of the resonator, we extract the second-order susceptibility in the MQWs regions, which show ~20 times (at 1550 nm) and ~10 times (at 780 nm) higher compared to that of AlN, respectively. Our study shows a promising path to realize III-N integrated photonic modulators with a stronger Pockels effect by employing MQWs with optimal overlap with the optical mode of the modulator.

Finally, Chapter 8 presents the summary of the thesis and some future works focused on the nonlinear characteristics of III-N semiconductors, including mode-lock frequency comb generation at cryogenic condition, nonlinear IR up-conversion, and investigation of enhanced nonlinearity of III-N semiconductors.

Chapter 2 Methods

2.1 Overview

This section introduces experimental techniques used in each study, including molecular beam epitaxy system, material characterization, and device measurement techniques. Both principles and measurement setups are detailed in this section.

2.2 Molecular Beam Epitaxy (MBE)

Molecular beam epitaxy is a unique and well-developed epitaxy growth method for III-V compounds which is a physical vapor deposition method based on the surface kinetics of adatoms and thermodynamics of crystal formation [87-89]. The MBE systems used in this work are Veeco GEN930 and Veeco GENxplor systems equipped with radiofrequency (RF) plasma-assisted nitrogen source where growths take place under high vacuum conditions (base pressure $\sim 10^{-12}$ Torr) using both cryo pump and ion pump. The systems contain several different target elements contained in source effusion cells which are heated and slowly evaporated toward the substrate. Due to the ultra-high vacuum environment, evaporated atoms only react when the elemental beam converges on the substrate [86], resulting in the high purity of the single crystal grown films.

One of the dominant factors that decide the growth condition is the substrate temperature. Our systems are equipped with a pyrometer and thermocouple heater to monitor and control the temperature and calibrate growth temperature with different samples. Our substrate heater can be heated up to ~ 1800 °C, which is ideal for epitaxial growth of large bandgap III-N materials.

The surface morphology and crystallinity of the grown film can be monitored by reflection high-energy electron diffraction (RHEED), which shows real-time *in-situ* feedback of the grown layer. Installed electron gun shoots high-energy electron aiming to the sample, and its diffracted patterns are shown in phosphor screen which contains the information of few monolayers of sample surface due to the shallow angle injected electron [90]. Therefore, the pattern shown in the RHEED presents the surface morphology and crystallinity of the grown films in real-time.

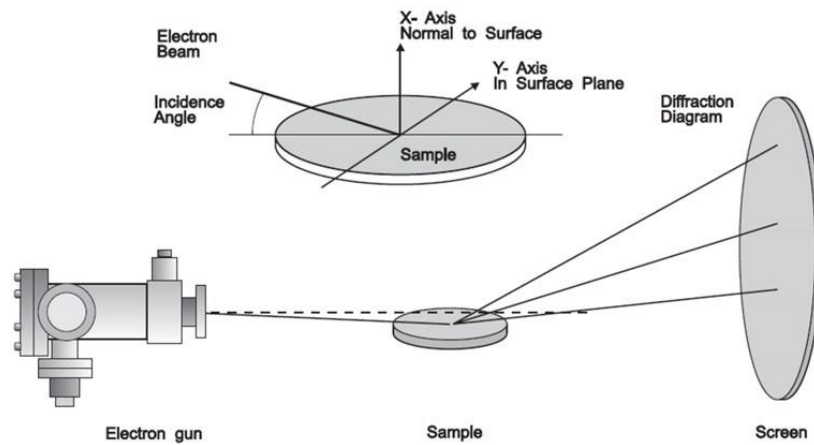


Figure 2.1: The schematic of reflection high-energy electron diffraction (RHEED) operation [91].

2.3 Optical Characterization Techniques

2.3.1 Photoluminescence Spectroscopy

Photoluminescence (PL) spectroscopy is a non-contact, non-destructive measurement commonly used for sample characterization, which shows the optical characteristic of the semiconductors [3]. When photon energy is higher than the bandgap of material injected onto a sample, the charge carrier generates due to the photoexcitation and release energy (photon), as it

relaxed by radiative recombination, which results in light emission. Figure 2.2 shows the PL process in typical direct and indirect bandgap materials.

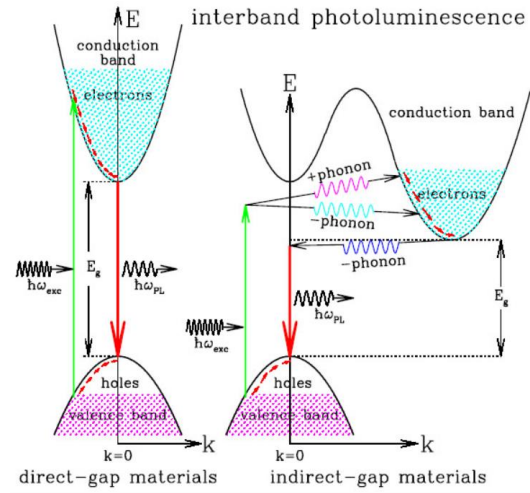


Figure 2.2: Schematic of the PL process with direct and indirect bandgap materials [92].

The samples studied in this thesis are based on Al(Ga)N alloys which are wide bandgap materials, and a Coherent Excistar XS500 ArF excimer laser with an emission peak at 193 nm is used for exciting the samples. The generated photons are collected and detected by a UV-sensitive charge-coupled detector (CCD).

2.3.2 Spectroscopic Ellipsometry

Spectroscopic ellipsometry is a versatile optical measurement technique mainly used for measuring sample thickness, growth/etch rates, and refractive index. In general, ellipsometry measures polarization change caused by the interaction of light with the sample, which arises from the reflectivity difference between electric field components oriented parallel (p-) and perpendicular (s-) to the plane of incidence, shown in Fig. 2.3. These polarization change

differences between p- and s- polarized fields are represented as amplitude ratio (ψ) and phase difference (Δ), and Spectroscopic Ellipsometry measures the change in polarization with different incident angles over a broad wavelength. The Cauchy dispersion model can be fitted to the measured polarization change and extract the thickness, the refractive index, and the absorption characteristic of the sample within a transparent wavelength.

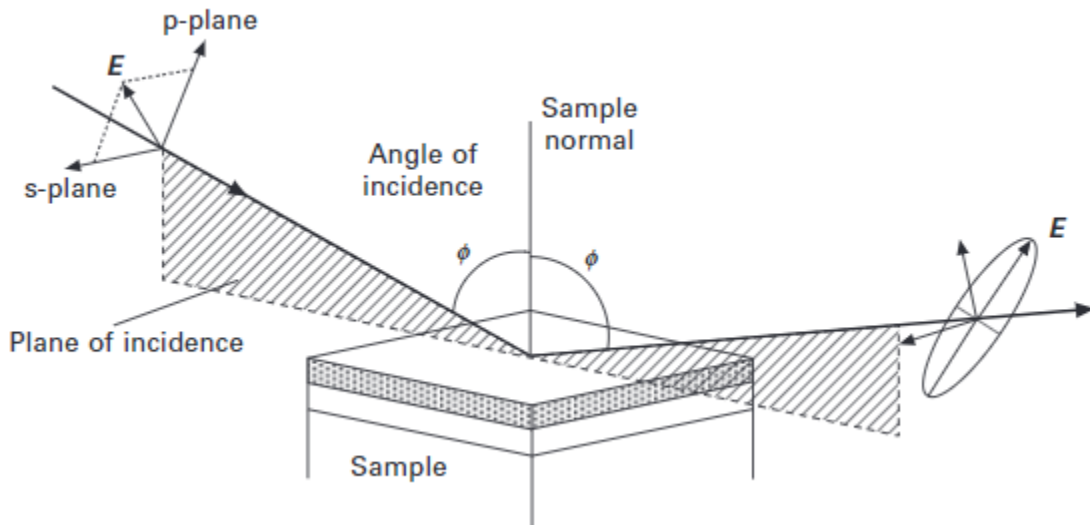


Figure 2.3: Spectroscopic ellipsometry technique [93].

2.4 Structural Characterization Techniques

2.4.1 X-Ray Diffraction

X-ray diffraction (XRD) is a well-known characterization technique for determining the atomic and molecular structure of a crystal, which shows the material quality, lattice constants, strain, and composition of the grown layer. Shown in Fig. 2.4 (a), fixed wavelength X-ray beam injected to the sample where X-ray is diffracted based on crystal lattices following Bragg's Law, and destructive and constructive interference occurs based on the incident and detection angles.

Since the diffraction depends on the angle of incidence, substrate orientation, and crystal lattice, various structural information can be extracted from the measurements.

In this thesis, the Rigaku SmartLab XRD system, shown in Fig. 2.4(b), is used to measure coupled 2θ - ω scans, primarily used to estimate the composition of the grown samples and material quality.

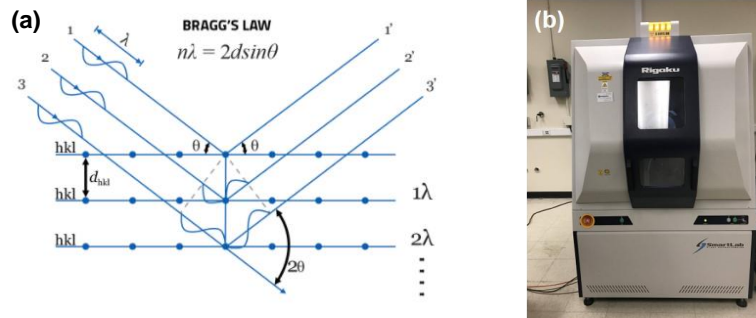


Figure 2.4: (a) Mechanism of XRD experiment [94]. (b) A Rigaku SmartLab XRD system.

2.4.2 Scanning Electron Microscopy

Scanning electron microscopy (SEM) uses a high-energy electron-focused beam to generate secondary electrons, backscattered electrons, and X-rays at the surface of the sample. These signals derived from the electron-sample interactions show morphology, crystalline structure, and materials orientation. In this thesis, Hitachi SU8000 cold field emission Scanning Electron Microscope (FE-SEM) is used, which provides high magnification with a resolution of a few nanometers scale range.

2.5 Light Emitting Diode Characterization Techniques

2.5.1 Current-Voltage Measurement

Current-voltage (I-V) measurement is a widely used device characterization technique that provides direct estimates of diode performance. Since LEDs are based on p-n junctions, the ideal I-V characteristic of LEDs should follow the typical diode characteristics, which show turn-on voltage close to the material bandgap with negligible leakage current at reverse bias. Therefore, I-V measurement can provide information on the fabrication and the material growth of demonstrated LEDs. In this thesis, Keithley 2400 SMU was used for continuous wave (CW) source, and A-1010B pulse generator was used for pulsed source to measure I-V characteristic of demonstrated LEDs. Typically, due to the significant heating effect of our devices, the pulsed source showed higher EQE than the CW source.

2.5.2 Electroluminescence Spectroscopy

Electroluminescence (EL) spectroscopy is an optical and electrical phenomenon where material emits light in response to the injection current or strong electric field. A UV transmissive fiber optic cable collects the emitted light and analyzes the spectrum through CCD when UV light is emitted from the demonstrated LEDs under applied positive bias. In this thesis, we mostly used to check the emission spectrum of demonstrated LEDs. Different from PL, which is mainly determined by the optical properties of the materials, the EL spectrum is decided by several factors such as the optical properties and physical structures of the active layers, the electrical properties of two contact layers, and the properties of the electrical contacts.

2.5.3 LED Power Measurement

In this thesis, we used Newport 818-ST-2 UV photodetector with a Newport 1919-R power meter for optical power measurement. For backside emitting LEDs, demonstrated samples were placed directly on the photodetector. In contrast, for top-emitting LEDs, the photodetector cannot be placed right on top of the devices due to the height of the contact probe. Therefore, the distance between the sample and photodetector is considered, calibrating the measured optical power. Based on the measured optical power, voltage and current, LED efficiency such as EQE and WPE are calculated.

2.6 Microring Resonator and Modulator Characterization Techniques

2.6.1 Transmission Characterization of Microring Resonator

Figure 2.5 shows the experimental setup for characterizing the demonstrated microring resonator (MRR). High-performance tunable lasers are used to sweep the input wavelength within the target range with a resolution of ~ 0.1 pm to measure the characteristics of the demonstrated MRR. To perform the edge-coupling technique, lensed fiber (NIR wavelength) or collimator/objective lens (visible wavelength) are utilized for coupling the light into the chip. The fiber polarization controller (FPC) is placed and adjusted while monitoring the output optical power to control the polarization of input sources. The output light from the chip is coupled to the lensed fiber and goes through a power splitter (9:1) connected to both the power meter and photodetector (PD). The transmittance from the PD and input wavelength from the tunable laser are recorded. To characterize the resonance shift of the demonstrated MRM, a high-speed ground-signal-ground (GSG) probe is used to apply an out-of-plane electric field in the ring resonator core.

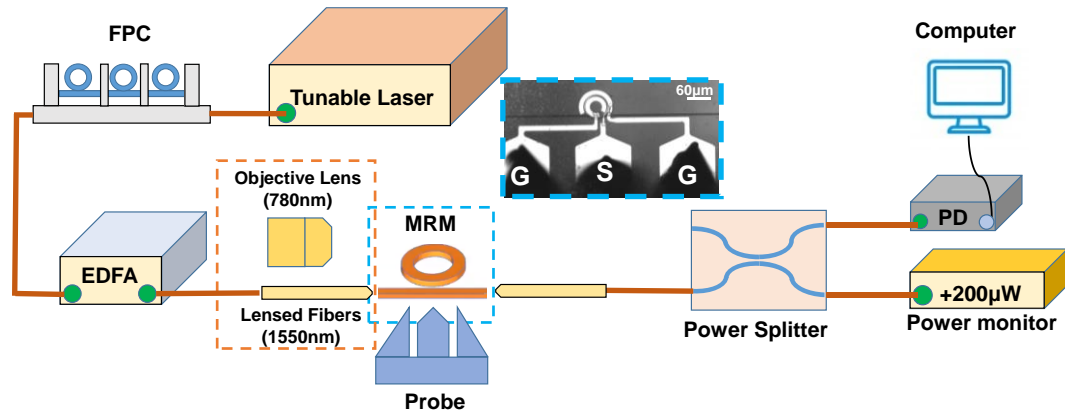


Figure 2.5: Measurement setup for MRR transmission characteristics.

2.6.2 Electro-Optic Modulation Measurement in Frequency Domain

Figure. 2.6 shows the experimental setup for measuring electro-optic modulation in the frequency domain, used to extract 3dB bandwidth of the demonstrated MRM. To achieve a high-resolution frequency response of MRM, erbium-doped fiber amplifier (EDFA) and optical filter are included before the photodetector. Subsequently, a vector network analyzer (VNA), widely used in the RF domain measurement technique, is utilized to measure the EO modulation amplitude in the frequency domain (S_{21}). In this thesis, due to the limited optical amplifier at 780nm and visible wavelengths, the measurement is only performed at telecom wavelengths.

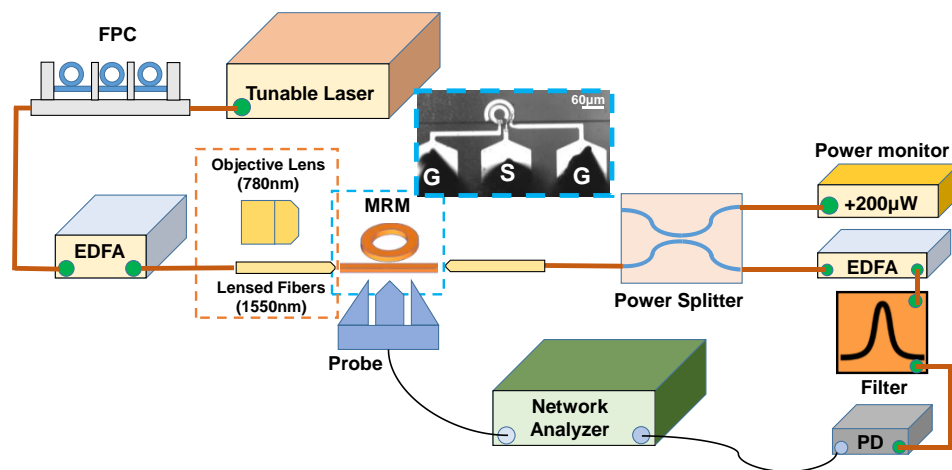


Figure 2.6: Measurement setup for MRR frequency response measurement.

Chapter 3 High-Efficiency Tunnel Junction AlGaN UV LEDs

3.1 Author Contribution and Copyright Disclaimer

The contents of this chapter were published in the Photonics Research journal in February 2020 [83], for which I retain the right to include it in this thesis/dissertation, provided it is not published commercially. The co-authors were Ayush Pandey, Jiseok Gim, Robert Hovden, and Zetian Mi from the University of Michigan. I contributed partly to the design, characterization, fabrication, and measurement of the work. A. Pandey, the first author, contributed to design, material growth, and measurement. J. Gim and R. Hovden collected the HAADF-STEM images presented. The work was supervised by Z. M., who contributed to the design of the experiments. This work was supported by the Army Research Office under the grant W911NF19P0025 and the University of Michigan, College of Engineering.

3.2 Introduction

According to the World Health Organization, health-care associated infections (HCAIs) [95] and water-borne illnesses [96] are responsible for thousands of fatalities and billions of dollars in costs each year. Sterilization of medical equipment and water supplies is now frequently utilized to minimize the possibility of infections by neutralizing pathogens, and for this purpose, conventional mercury UV lamps have been widely used. Semiconductor optoelectronic devices offer an alternative that is non-toxic, more compact, and more flexible in applications. The AlGaN alloy system is uniquely suited for this purpose as the alloys are direct bandgap semiconductors

spanning from ~200 nm to ~365 nm in wavelengths. To date, AlGaN LEDs operating in the UV-C band (200-280 nm), which is of prime importance for sterilization, exhibit low efficiency, which has been attributed to the poor light extraction associated with TM-polarized light emission [97-100], low luminescence efficiency due to the presence of large densities of defects [25, 101], and inefficient p-type doping [102-104]. These issues become more severe for LEDs operating at shorter wavelengths which require a higher Al content in the device active region. In this regard, intensive studies have been performed to improve the light extraction efficiency by engineering the energy band structure [105, 106] and utilizing nanostructures [107-110]. Various techniques, including epitaxy on nano-patterned substrates and high-temperature annealing, have also been developed to reduce the formation of defects [111-114]. Recently, EQE over 20% was reported for AlGaN LEDs operating at 275 nm, which, however, had a low WPE of 5.7% [51]. To our knowledge, the best reported EQE for AlGaN LEDs operating at ~265 nm, an important wavelength for water purification and sterilization [115], is ~6.3% for packaged devices grown using MOCVD [116, 117]. However, direct on-wafer measurements, typically result in lower efficiencies due to reduced light extraction/collection and severe self-heating of the devices, with the best peak EQE of only ~2% at ~265 nm [118, 119]. The maximum wall-plug efficiency of these devices is often much lower, which is fundamentally limited by the large resistance and poor hole injection efficiency due to the high resistivity of p-type AlGaN. Moreover, the poor p-type conduction, together with the highly asymmetric hole and electron injection efficiencies, can lead to parasitic carrier recombination outside the active region [120, 121], which further exacerbates the heating of the devices and can have a detrimental impact on the device performance [122-125]. While using p-GaN as the contact layer may partly alleviate the issue of hole injection to the active

region, it has an adverse impact on the light extraction efficiency due to the significant UV light absorption by GaN [19].

A promising technique to improve hole injection is utilizing a tunnel junction structure, wherein holes are injected into the valence band of the p-type layer by the interband tunneling of electrons to the conduction band of an n-type layer. Using the tunnel junction structure, the high resistance p-AlGa_N layer can be replaced by a relatively low resistance n-AlGa_N contact layer, which further allows a reflective Al ohmic contact to enhance the light extraction for backside emitting devices [126-128]. The III-N-based homojunction tunnel diodes have been previously demonstrated using highly doped GaN [129-131]. However, the doping required for efficient interband tunneling of carriers becomes extremely difficult to attain AlGa_N alloys due to their higher bandgaps and less efficient p-type doping. Such critical challenges can be addressed, to a certain extent, through polarization engineering by incorporating a thin layer of different compositions between the n and p-type layers [12, 132-134]. Due to the strong spontaneous and piezoelectric polarization, the sheet charges at the hetero-interfaces help better align the conduction band of the n-type layer with the valence band of the p-type layer while reducing the width of the depletion region. This results in a dramatic increase in the probability of electron tunneling. Such a technique has been employed in visible LEDs [11] and lasers [135] and has also been demonstrated using an InGa_N-based tunnel junction for UV LEDs grown using MBE [127, 128, 136] and GaN-based tunnel junction for UV LEDs grown using MOCVD [137].

In this chapter, we demonstrate using a GaN polarization engineered tunnel junction with a p-AlGa_N/GaN/n-AlGa_N structure to realize high-efficiency AlGa_N LEDs operating at 265 nm. A series of samples with different GaN widths and thicknesses of the top n-AlGa_N contact layer were grown and fabricated, and their effect on device performance was thoroughly studied. Through

detailed optimization, we demonstrate LEDs with emission wavelengths ~ 265 nm with a maximum EQE of 11%. The peak WPE was measured to be 7.6%. It is also observed that these devices exhibit severe efficiency droop at relatively low current densities. The underlying causes have been discussed. This work provides new insights on the performance improvement of AlGaIn deep UV LEDs.

3.3 Epitaxy of UV LED Structures

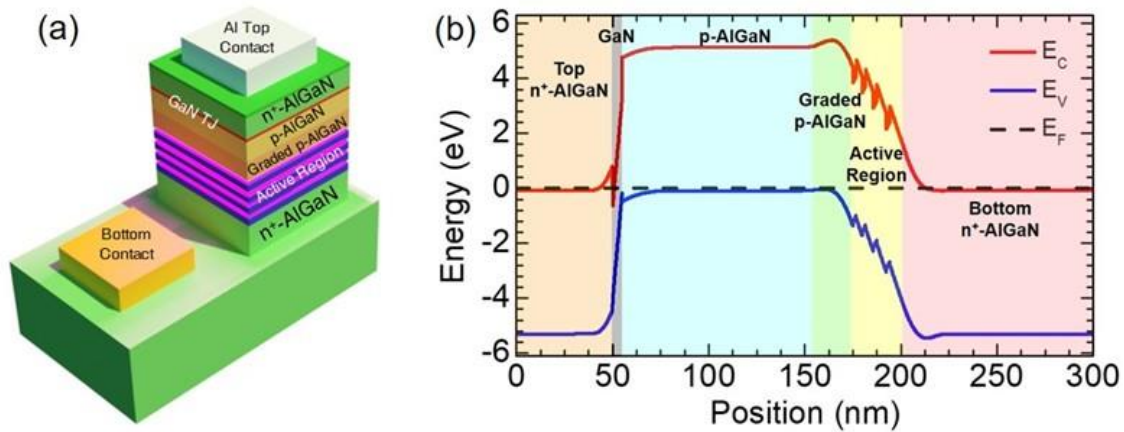


Figure 3.1: (a) Schematic illustration of the tunnel junction LED structures. (b) Simulated equilibrium band diagram for a representative LED using a 5nm GaN layer. The different layers used in the structure are labeled and shown with different colors.

The tunnel junction LED structures were grown in a Veeco Gen 930 PA-MBE system on 1 μm thick AlN-on-sapphire substrates from DOWA Holdings Co. Ltd. A nitrogen flow rate of 0.6 SCCM, with an RF power of 350W, was used throughout the growth. The growth rate is ~ 160 nm/hr for the AlGaIn epilayers. The growth was conducted using metal-semiconductor junction-assisted epitaxy to enhance Mg-dopant incorporation and reduce defect formation [40]. A schematic of the LED structures is shown in Fig. 3.1(a). The growth was initiated with a ~ 50 nm thick AlN layer, followed by the subsequent AlGaIn growth. The initial ~ 500 nm thick

$\text{Al}_{0.65}\text{Ga}_{0.35}\text{N}$ layer was Si-doped to form the bottom n-contact. The Al composition of the AlGaIn was graded up from 65% to 85% in a thickness of ~20 nm immediately before the active region. The active region consisted of four AlGaIn quantum wells with compositions ~60% designed for peak emission at ~265 nm. The AlGaIn barriers, with higher Al compositions, were grown with decreasing thicknesses, from ~5 nm to ~3 nm closer to the Mg-doped AlGaIn. A graded Mg-doped AlGaIn layer, with a thickness of ~20 nm and Al compositions varying from 80% to 65%, followed the last quantum well. The grading down of the Al composition of the AlGaIn provides polarization-induced doping, which enhances the hole concentration [39]. A ~100 nm thick p- $\text{Al}_{0.65}\text{Ga}_{0.35}\text{N}$ was then grown, followed by the GaN layer. Compared to the previously reported InGaIn-based tunnel junction UV LEDs grown by MBE [127, 128, 136, 138], there was no growth interruption for the tunnel junction as the substrate temperature was kept the same as that for the GaN and AlGaIn layers. Following the growth of the tunnel junction, the top n^+ - $\text{Al}_{0.65}\text{Ga}_{0.35}\text{N}$ contact layer was grown. Different design parameters, including the thicknesses of the GaN layer and the top n^+ -AlGaIn contact layer, are listed in Table 3-1. A one-dimensional Poisson-Schrödinger solver was used to simulate the band diagram of a representative structure having 5 nm GaN width, as shown in Fig. 3.1(b).

Table 3-1: List of tunnel junction LED structures.

Sample	GaN Thickness	Top n^+-AlGaIn Thickness
A	2.5 nm	50 nm
B	2.5 nm	150 nm
C	5 nm	150 nm
D	10 nm	150 nm
E	5 nm	480 nm

3.4 Characterization of the UV LED structure

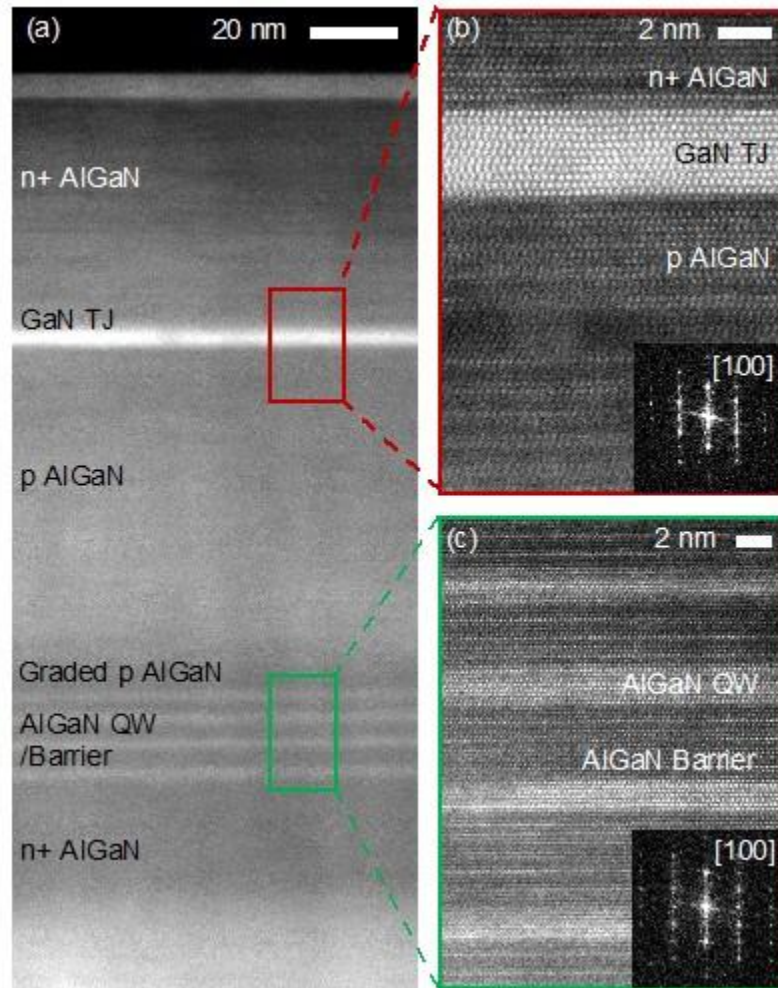


Figure 3.2: (a) HAADF-STEM overview of cross-sectional AlGaIn multilayers shows the complete device structure. (b) The high-resolution HAADF-STEM of the p-AlGaIn/GaN/n-AlGaIn tunnel junction shows crystalline epitaxial growth with sharp interfaces for enhanced hole injection by tunneling. (c) Atomic-resolution HAADF-STEM of $\text{Al}_{0.6}\text{Ga}_{0.4}\text{N}$ quantum wells coupled to $\text{Al}_{0.85}\text{Ga}_{0.15}\text{N}$ barriers with sharp epitaxial interfaces for carrier confinement.

HAADF-STEM on a representative sample confirms the AlGaIn multilayer structure with p-AlGaIn/GaN/n-AlGaIn tunnel junction and AlGaIn quantum well layers, shown in Fig. 3.2(a). The GaN layer (~5 nm) is epitaxially grown between the top n^+ -AlGaIn contact and p-AlGaIn layer with sharp interfaces, as shown in Fig. 3.2(b). The ratio of HAADF STEM intensity estimates $\sim 64\% \pm 6\%$ less Ga in the p-AlGaIn layers compared to the Ga concentration in the GaN layer. The high

relative Ga content in the tunnel junction is expected to increase the efficiency of charge carrier injection by tunneling. High-resolution cross-sectional STEM, shown in Fig. 3.2(c), also confirms the epitaxial growth of four AlGa_N quantum wells (~ 2 nm) with ~27% ± 3.5% higher content of Ga relative to adjacent AlGa_N barriers (ranging from ~ 5 nm to ~ 3 nm) that confine charge carriers. Fast Fourier transforms (FFT) of the atomic resolution HAADF STEM images confirm the (100) lattice plane of AlGa_N multilayers with an orientation that indicates preferred growth along the [001] c-axis direction.

3.5 Tunnel Junction Design Optimization and Characterization

All the 265 nm LED structures were fabricated using the same process to maximize emission from the backside of the wafer. A BCl₃/Cl₂ plasma was first used to dry etch the samples down to the bottom n-contact layer, with device mesas having an areal size of 40 μm × 40 μm. This was followed by the deposition of an HfO₂/SiO₂ dielectric distributed Bragg reflector (DBR) to increase light reflection towards the wafer's backside and serve as a surface passivation layer. The thicknesses of HfO₂ and SiO₂ layers are ~30 nm and ~45 nm, respectively, which were calculated based on the measured refractive indices of the dielectric layers and an Al_{0.65}Ga_{0.35}N epilayer to maximize reflectivity around 265 nm. Openings were then etched into the passivation layer for the deposition of metal contacts. A top reflective contact of Al (250 nm)/Au (50 nm) was then deposited [126, 128], followed by a Ti (40 nm)/Al (120 nm)/Ni (40 nm)/Au (50 nm) metal stack for the bottom n-contact. The metal contacts were annealed at 700 °C for 30 seconds in nitrogen ambient.

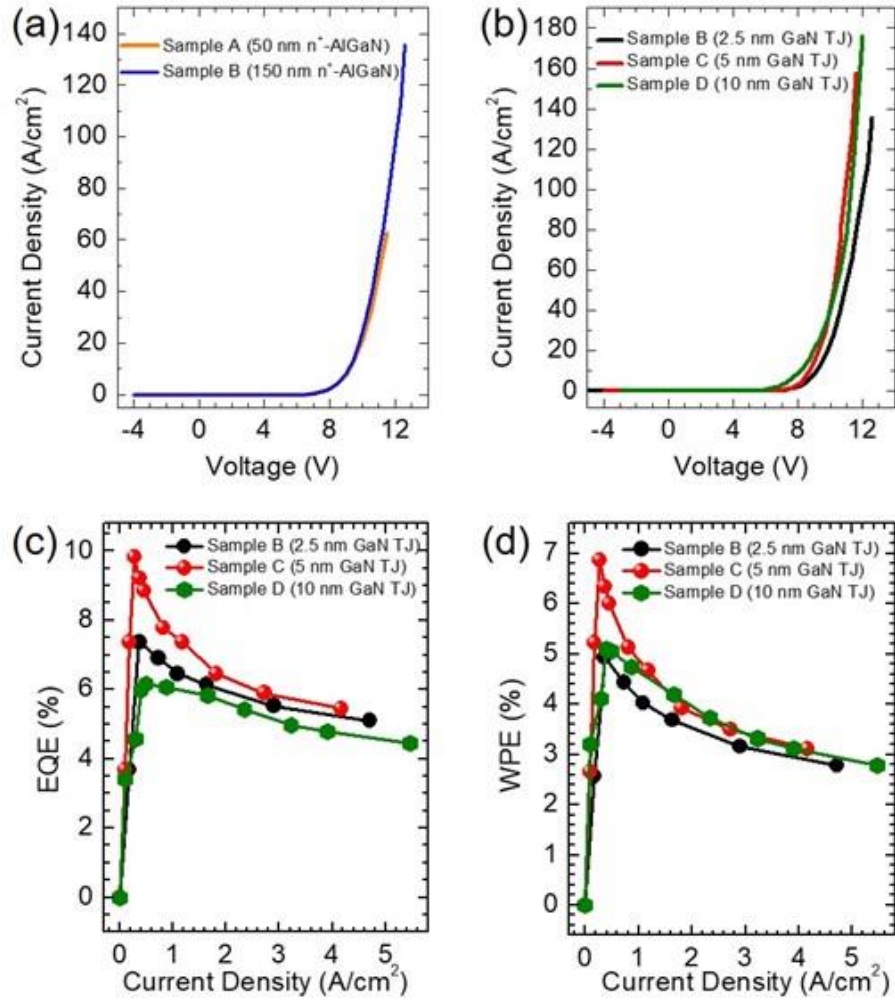


Figure 3.3: (a) I-V characteristics of tunnel junction LED samples A and B, with 2.5 nm GaN layer width and different thicknesses, 50 nm, and 150 nm, respectively, of the top n⁺-AlGaIn contact layer. (b) I-V characteristics of samples B, C, and D grown with the same thickness of top n⁺-AlGaIn but different GaN layer widths of 2.5 nm, 5 nm, and 10 nm, respectively. Variations of (c) EQE and (d) WPE with injected current density, for samples B, C, and D.

Measurements were performed using an AV-1010B pulse generator, with a 1% duty cycle and a 10 kHz repetition rate to minimize the heating effect. A calibrated Newport 818-ST2-UV silicon photodetector with a Newport Model 1919-R power meter was used to measure the device output power. Figure. 3.3(a) shows the current-voltage characteristics for samples A and B, which have a 2.5 nm thick GaN layer between the highly doped AlGaIn layers but with different thicknesses of the top n⁺-AlGaIn contact layer. It is seen that the devices exhibit similar I-V characteristics

under relatively low current densities. However, higher current densities can only be measured in Sample B, which has a thicker (~150 nm) top n^+ -AlGa N contact layer. Slightly higher efficiency was also measured for Sample B than Sample A. We have subsequently studied the effect of different thicknesses of the Ga N layer within the tunnel junction on the device efficiency while keeping the top n^+ -AlGa N contact layer thickness at 150 nm. The Ga N layer thicknesses were varied from 2.5 nm (Sample B), 5 nm (Sample C) to 10 nm (Sample D). I-V characteristics of these devices were measured and shown in Fig. 3.3(b). It is seen that Samples C and D have slightly better turn-on voltage compared to Sample B. The slight difference between the turn-on voltages of the different structures indicates that tunneling through the tunnel junction might be dominated by trap-assisted tunneling [139, 140]. Studies on AlGa N /Ga N -based double barrier resonant tunnel diodes have suggested that trapped charges at the hetero-interface are responsible for the observed electrical characteristics [141]. It has also been shown previously that a high concentration of impurity atoms at the tunnel junction interface can improve the turn-on voltage of the tunnel junction by providing states enabling trap-assisted tunneling [142-144]. The reduced turn-on voltage through trap-assisted tunneling improves the wall-plug efficiency of the tunnel junction LEDs by facilitating carrier transport even at low biases. The measured EQE and WPE are shown in Fig. 3.3(c) and Fig. 3.3(d), respectively. A maximum EQE of 9.8% was measured for Sample C. In contrast, maximum EQE of 7.4% and 6.2% were measured for Samples B and D, respectively, suggesting that a Ga N layer thickness ~5 nm is optimum for the presented tunnel junction structures. This could be due to the degraded material quality with incorporating a thicker Ga N layer, whereas a thinner Ga N layer may not provide sufficiently strong polarization. Moreover, a thicker Ga N layer also increases the absorption of UV light emission from the device active region. A thick Ga N layer would also present an obstacle to carrier transport due to the increased distance

that electrons would need to tunnel through. A peak WPE of 6.9% was measured for Sample C, shown in Fig. 3.3(d).

It is interesting to note that all the devices showed a strong droop even at the relatively low current injection of $\sim 0.5\text{-}1\text{ A/cm}^2$, suggesting that the cause of the droop is independent of the tunnel junction designs. Efficiency droop has been commonly measured for InGaN-based blue and green LEDs at current densities $\sim 5\text{-}10\text{ A/cm}^2$ [145, 146]. The underlying causes for the efficiency droop, including carrier delocalization, Shockley-Read-Hall (SRH) recombination, Auger recombination, and device heating, have been intensively studied [146-148]. At low current densities of $\sim 1\text{ A/cm}^2$, device heating and Auger recombination are not expected to be significant. As studied previously, the operation of GaN-based LEDs may deviate from low-level injection conditions even under relatively low current densities due to the asymmetric charge carrier transport [120, 149, 150]. Due to the large activation energy for Mg dopant in Al-rich AlGaN, p-type conduction is primarily mediated by hole hopping in the Mg impurity band at room temperature, which has low mobility [40, 151]. For Al-rich AlGaN, the electron mobility is typically on the order of $20\text{-}50\text{ cm}^2\cdot\text{V}^{-1}\cdot\text{s}^{-1}$ [152], whereas the hole mobility is $\sim 1\text{-}5\text{ cm}^2\cdot\text{V}^{-1}\cdot\text{s}^{-1}$ [153], or lower, while the corresponding maximum electron and hole concentrations are $\sim 10^{19}\text{ cm}^{-3}$ and $\sim 10^{17}\text{-}10^{18}\text{ cm}^{-3}$, respectively. The resulting conductivity of the n and p-AlGaN layers is nearly three orders of magnitude different. Consequently, even at a small current density of 1 A/cm^2 , the device operates in a regime that severely deviates from the low carrier injection condition. The resulting electric field in the p-AlGaN layer, even at a seemingly small current density, affects the transport of holes more severely than that of electrons due to the large difference in their mobility values. This leads to a significant increase in charge carrier recombination outside of the device active region, i.e., electron overflow to the p-AlGaN layer, at

a small injection current. A similar effect has also been measured in AlGaN nanowire UV-C LEDs [149]. Further, it should also be noted that as the epitaxial growth of the entire LED structure was performed under slightly Ga-rich conditions, it is expected that the distribution of Ga may not be uniform in the epilayers [119, 154-156]. It has been shown that these Ga-rich regions act as highly efficient radiative recombination sites due to their ability to locally confine excitons. However, as the injected current into the device increases, carrier delocalization will occur, allowing carriers to recombine at non-radiative recombination centers and decrease device efficiency.

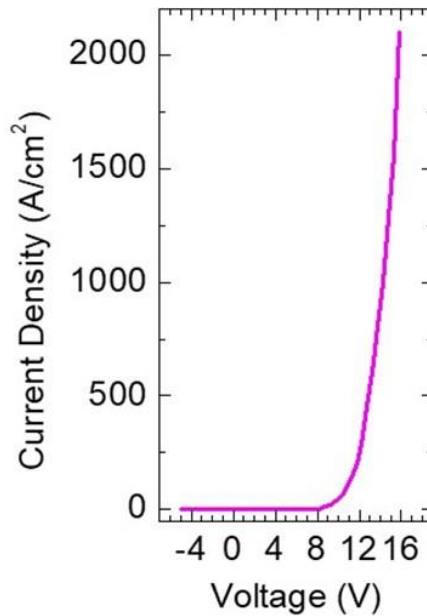


Figure 3.4: I-V characteristics of an optimized tunnel junction LED from sample E with a GaN layer thickness of 5 nm and top n⁺-AlGaN contact layer thickness ~480 nm.

Based on the studies above, a 265 nm deep UV-LED structure with a 5 nm thick GaN layer in the p-AlGaN/GaN/n-AlGaN tunnel junction and ~480 nm thick top n-AlGaN contact layer (Sample E) was grown and fabricated. The measured current-voltage characteristics are shown in Fig. 3.4. A large current density of ~2,000 A/cm² was measured at 16 V, which is significantly better than that measured in Samples A-D and tunnel junction UV-C LEDs reported previously

having emission at a similar wavelength [128, 137]. The high current density measured for this sample suggests the optimization of the p-AlGaIn/GaN/n-AlGaIn tunnel junction by adjusting the width of the GaN layer together with a relatively thick n-AlGaIn top contact layer, can significantly enhance the current injection and stability of deep UV LEDs.

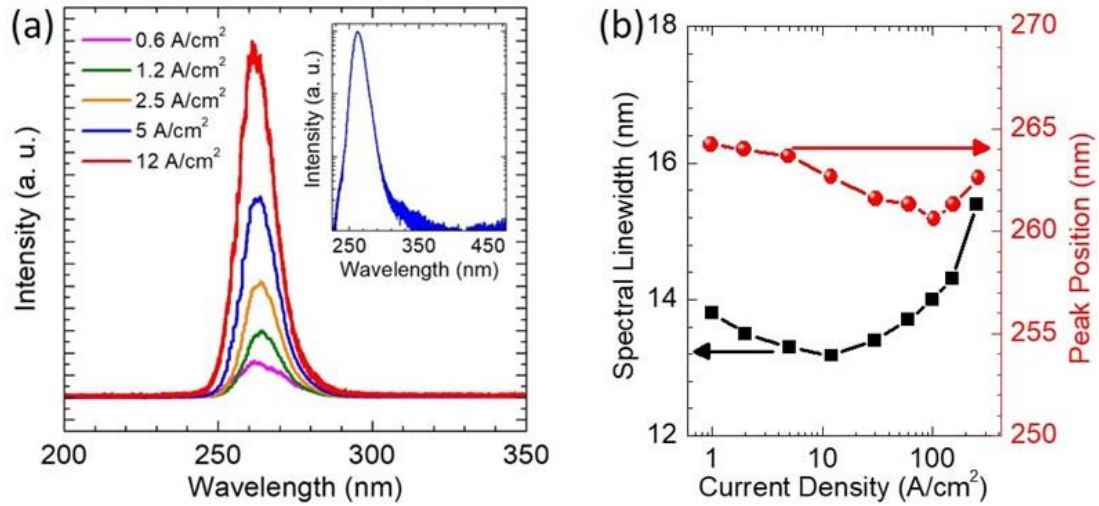


Figure 3.5: (a) Electroluminescence spectra measured at different injection currents for a representative tunnel junction LED. The inset shows an electroluminescence spectrum measured at 25 A/cm² current density with the intensity in log scale. (b) Variations of peak position (red circles) and spectral linewidth (black squares) vs. injected current density.

Shown in Fig. 3.5(a) are the electroluminescence spectra of an LED from Sample E measured at different current densities. The spectra were measured using CW bias supplied by a Keithley 2400 SMU, collected using an optical fiber coupled to a high-resolution spectrometer, and detected by a charge-coupled device. Variations of the peak position and spectral linewidth with current density are shown in Fig. 3.5(b). It is seen that the device first exhibits a small blueshift from ~264 nm to ~260 nm with increasing current density, followed by a redshift at relatively high injection conditions. The blueshift can be explained by the QCSE. The polarization field in AlGaIn quantum wells is estimated to be ~370 kV/cm based on the shift experimentally

observed, assuming that an injected current density of $\sim 100 \text{ A/cm}^2$ completely flattens the bands in the quantum well, while not significantly affecting the emission wavelengths due to heating. This is substantially less than the predicted theoretical value of 1.5-2.5 MV/cm [13, 157], indicating the compensation of the sheet charge by impurities or defects and some degree of relaxation in the AlGaIn layers. The red-shift at higher operating currents is likely due to the heating effect. Such a red-shift has also been reported previously for both AlGaIn [122] and InGaIn [158] LEDs. The spectral linewidths stay nearly constant at $\sim 13.5 \text{ nm}$ at low current densities and broaden to $\sim 15.5 \text{ nm}$ at relatively high injection conditions. It is also noticed that no significant defect-related emission was measured in the UV-C LEDs, shown in the inset of Fig. 3.5(a).

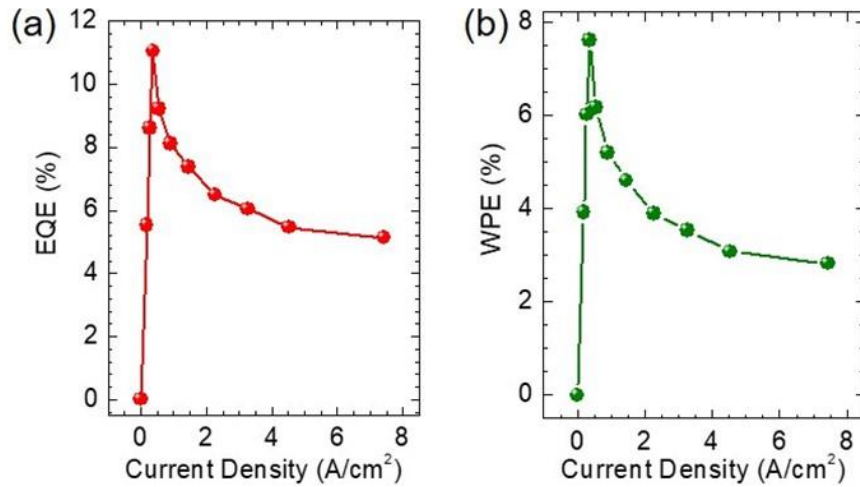


Figure 3.6: (a) Variations of (b) EQE and (c) WPE with injected current density for an LED from sample E.

The measured EQE and WPE of the LED from Sample E are shown in Figs. 3.6(a) and (b), respectively. A maximum EQE of 11% and WPE of 7.6% were measured. The EQE measured here is higher than comparable UV LEDs having emission at this wavelength [116-119, 128, 137], although still below the highest reported for LEDs at 275 nm [51]. However, the tunnel junction

devices studied here have a higher WPE due to the more efficient carrier injection from such a structure, resulting in significantly lower turn-on voltages. It is also noticed that efficiency droop is present at low current injection despite the optimization in the tunnel junction structure design. The external quantum efficiency of such a diode was fitted using the standard ABC model [159, 160]. From the fitted curve (not shown), A, B, and C parameter values of $1.6 \times 10^7 \text{ s}^{-1}$, $1.1 \times 10^{-9} \text{ cm}^3 \text{ s}^{-1}$, and $7.4 \times 10^{-27} \text{ cm}^6 \text{ s}^{-1}$ were derived. The estimated C value of $7.4 \times 10^{-27} \text{ cm}^6 \text{ s}^{-1}$ is around three orders of magnitude higher than the previously reported Auger coefficient of $\sim 10^{-30} \text{ cm}^6 \text{ s}^{-1}$ for AlGaN quantum well heterostructures [161], which, together with the presence of efficiency droop at very low current densities ($\sim 1 \text{ A/cm}^2$), strongly suggests that other carrier loss mechanisms, such as electron overflow, other than Auger recombination is the main cause for the efficiency droop of deep UV LEDs [120, 149].

3.6 Summary

In summary, we have studied the design, epitaxy, fabrication, and performance characteristics of p-AlGaN/GaN/n-AlGaN tunnel injected deep UV LEDs operating at $\sim 265 \text{ nm}$. Significantly improved current-voltage characteristics and efficiency were measured by incorporating GaN layer thickness $\sim 5 \text{ nm}$. The optimized AlGaN deep UV LED exhibited a maximum EQE and WPE of 11% and 7.6%, respectively. However, the device performance suffers from efficiency droop even at relatively low current densities $\sim 1 \text{ A/cm}^2$. The underlying cause is not likely due to Auger recombination, but instead could be related to electron overflow due to the small hole mobility associated with hole hopping conduction in the Mg impurity band of Al-rich AlGaN. To achieve high efficiency and high-power UV-C LEDs, it is important to

improve the hole mobility and p-type conduction of AlGaN by improving the epitaxy conditions, heterostructure design, and/or developing new p-type wide bandgap semiconductors.

Chapter 4 Photonic Crystal Tunnel Junction Deep UV LEDs with Enhanced Light Extraction Efficiency

4.1 Author Contribution and Copyright Disclaimer

The contents of this chapter were published in the Optics Express in December 2019 [84], for which I retain the right to include it in this thesis/dissertation, provided it is not published commercially. The co-authors were Ayush Pandey, Xianhe Liu, Yi Sun, and Zetian Mi from the University of Michigan. I designed, conducted, and authored most of the work. A. Pandey contributed to the sample growth and characterization. X. Liu contributed to optimizing e-beam lithography conditions, and Y. Sun contributed to fabrication. The work was supervised by Z. M., who contributed to the design of the experiments. This work was supported by the Army Research Office under the grant W911NF19P0025 and the University of Michigan, College of Engineering Blue Sky Research Program.

4.2 Introduction

The presence of large densities of defects and dislocation [25, 101, 162], poor p-type conduction [102, 104, 163, 164], and inefficient light extraction [97, 98] have been identified as some of the major challenges for achieving high-efficiency deep UV LEDs. Significant progress has been made in AlGaIn quantum well LEDs, with the best reported external quantum efficiency ~20% for devices operating at 275 nm [51]. It has remained extremely challenging, however, to achieve high wall-plug efficiency, particularly for devices operating at wavelengths ~265 nm or

shorter, which are well suited for water purification and disinfection applications [19, 20]. The light extraction efficiency of AlGaIn deep UV LEDs can be fundamentally improved by incorporating photonic nanostructures. To date, the design of photonic crystal LEDs is often based on photonic bandgap engineering to prohibit light emission into guided modes and enable coupling into the ambient, thereby enhancing light extraction. However, the device fabrication process involves either etching through the active region or the bottom-up epitaxy of nanowire structures [108, 109, 165-167]. The lack of deep UV transparent passivation materials [168, 169] makes it challenging to demonstrate high-efficiency UV devices. Such fabrication challenges can be addressed, to a certain extent, by employing photonic crystal structures as a diffraction grating layer to enhance light extraction efficiency for TM polarized emission [166]. Previously, the use of photonic crystal diffraction to increase LEE has been demonstrated for LEDs in the UV-A and visible spectra [166, 167, 170-173]. To date, however, there have been very few reports on the use of photonic crystal diffraction properties to improve light extraction in the deep UV to our knowledge [116, 174].

Another factor that fundamentally limits the wall-plug efficiency of deep UV LEDs is the poor p-type conduction of Al-rich AlGaIn due to the large activation energy (up to 600 meV) for the p-type (Mg) dopant and the formation of extensive compensating defects under relatively high doping conditions. Recent studies suggest that the formation energy for compensating defects can be significantly enhanced by tuning the Fermi level at the growth front away from the valence band edge during the epitaxy of Mg-doped AlGaIn. In contrast, the formation energy for Al (or Ga) substitutional Mg dopant incorporation can be reduced [40]. Therefore, large concentrations of Mg dopant can be incorporated without extensive defect formation and impurity incorporation. The resulting formation of an Mg impurity band enables hole hopping conduction and effectively

reduces the activation energy for a portion of Mg acceptors due to the dispersion of acceptor energy levels [175], thereby leading to significantly enhanced p-type conduction. Using this technique, relatively high hole concentration and small Mg-dopant activation energy have been measured for AlGa_N with high Al content. The achievement of relatively efficient p-type conduction of AlGa_N also provides the distinct opportunity to realize tunnel junction deep UV LEDs, which can further reduce the device contact resistance, enhance charge carrier (hole) injection, and reduce light absorption associated with conventional p-Ga(Al)_N contact layer [128, 132, 176, 177]. However, there has been no demonstration of tunnel junction deep UV devices with the incorporation of photonic crystal structures.

In this chapter, we report on the first demonstration of tunnel junction deep UV photonic crystal LEDs operating at ~267 nm. We have performed a detailed simulation of the light extraction efficiency (LEE) of AlGa_N quantum well LEDs with the integration of photonic crystal. We show that the LEE can be enhanced by nearly a factor of two, reaching over 60% by integrating photonic crystal structures on a conventional AlGa_N quantum well LED structure. Experimentally, we have investigated the MBE growth, characterization, and fabrication of such deep UV LEDs. The device exhibits a peak wall-plug efficiency (WPE) ~3.5% and external quantum efficiency (EQE) ~5.4%, which are approximately 2.5 times higher than identical top-emitting LED structures but without using photonic crystal structures. This work demonstrates a viable path for achieving high efficiency deep UV LEDs by integrating nanoscale structures with conventional planar AlGa_N.

4.3 Device Structure and Photonic Crystal Simulation

Illustrated in Fig. 4.1(a) is the schematic of the AlGa_{0.65}N deep UV LED heterostructure, which was grown using a Veeco Gen 930 MBE system equipped with a radio frequency plasma-assisted nitrogen source on 1 μm AlN-on-sapphire substrates from DOWA Holdings Co. Ltd. The device heterostructure consists of ~480nm Si-doped Al_{0.65}Ga_{0.35}N and a graded Si-doped AlGa_{0.65}N layer with Al compositions varied from 65% to 85% within ~25nm thickness. The active region consists of four Al_{0.6}Ga_{0.4}N quantum wells (QWs), showing a photoluminescence emission peak at ~267nm. A 25nm Mg-doped AlGa_{0.65}N layer with Al compositions varied from 85% to 65% was then grown, followed by a ~100nm thick p-Al_{0.65}Ga_{0.35}N, 5nm GaN, and 360nm n⁺-Al_{0.65}Ga_{0.35}N. The incorporation of a thin GaN in the tunnel junction design can enhance the tunneling probability due to the large polarization induced band bending [137, 177]. The samples were grown using the unique technique of metal-semiconductor junction assisted epitaxy, which can significantly enhance Mg-dopant incorporation and enable relatively efficient p-type conduction of Al-rich AlGa_{0.65}N [40].

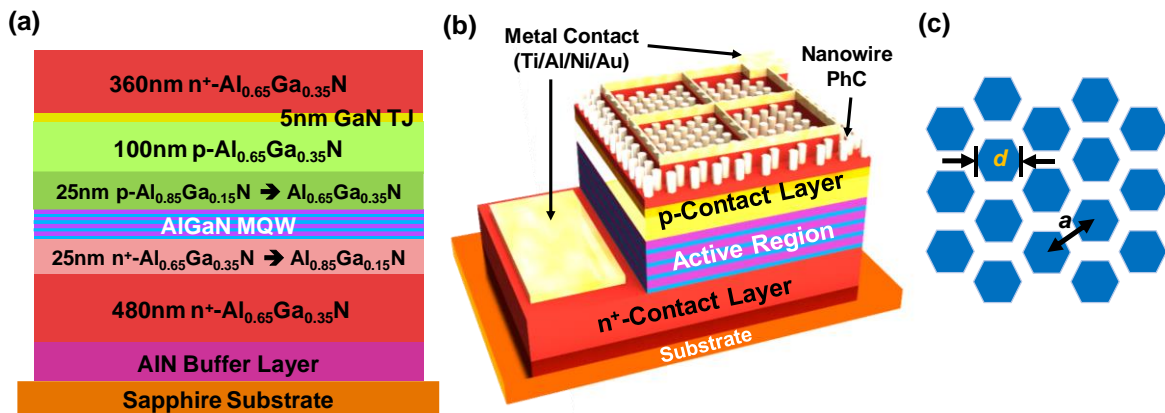


Figure 4.1: Schematic of (a) tunnel junction deep UV LED heterostructure and (b) nanowire photonic crystal integrated deep UV LED. (c) Top view of the nanowire photonic crystal.

Figure 4.1(b) shows the schematic of the device, wherein nanowire photonic crystal structures were realized by etching the topmost n+-AlGaIn layer of the planar deep UV LED structure. The nanowires have a hexagonal shape and are arranged in a triangular lattice, illustrated in Fig. 4.1(c). Important design parameters for achieving high LEE include nanowire diameter (d), lattice constant (a), nanowire height (L), and distance between active region and nanowire. To calculate the LEE, finite difference time domain (FDTD) simulation was performed using the Lumerical FDTD Solutions software package. To optimize top-emitting light extraction, a perfect electrical conductor substrate with nearly 100% reflectivity was included in the simulation, which can be experimentally realized by incorporating AlGaIn/AlN distributed Bragg reflectors (DBRs) [178]. Perfect matched layers (PMLs) were used as boundary conditions, which inhibit outgoing electromagnetic waves reflecting back into the simulation domain [179, 180]. A minimum mesh step size of 0.25nm was used via the adaptive meshing technique. A single polarized dipole source with a 1:1 ratio of TE and TM polarized emission was placed in the active region to simulate the light emission [181]. The dipole spectrum is Gaussian shape with 60nm full-width-at-half-maximum (FWHM) linewidth and a peak wavelength of 265nm. To increase simulation accuracy, the refractive indices for each layer are calibrated and further measured separately by Wollam M-2000 Ellipsometer, shown in Table 4-1, whereas average refractive index was used for the active region and graded AlGaIn layer. Absorption of emitted light in the p- and n-AlGaIn layers was not considered, given their larger bandgap than the quantum well active region.

Table 4-1: List of refractive indices for tunnel junction deep UV LED structure

Structure	Refractive index
$\text{Al}_{0.65}\text{Ga}_{0.35}\text{N}$ (meas.)	2.51
$\text{Al}_{0.85}\text{Ga}_{0.15}\text{N}$ (meas.)	2.35
GaN TJ (meas.)	2.67
Active region & graded AlGaIn layer (aver.)	2.43

Figure 4.2(a) shows the calculated LEE, averaged in the wavelength range of 264nm to 271nm, as a function of nanowire diameter (d) and lattice constant (a) for nanowire height $L = 240\text{nm}$. The highest light extraction efficiency ~60-64% was found at $d = 180\text{nm}$ and $a = 240\text{nm}$, and at $d = 160\text{nm}$ and $a = 320\text{nm}$, with the latter being used in the experimental studies in this work. The LEE was further calculated as a function of nanowire height, shown in Fig. 4.2(b). The LEE varied from ~50% to 61% for nanowire heights in the range of 140 to 340 nm. A nanowire height $L = 240\text{nm}$ was used in subsequent experimental studies. For comparison, the calculated LEE for an identical planar LED but without the incorporation of photonic crystal structures is ~30%, which is approximately two times lower than the presented photonic crystal UV LED.

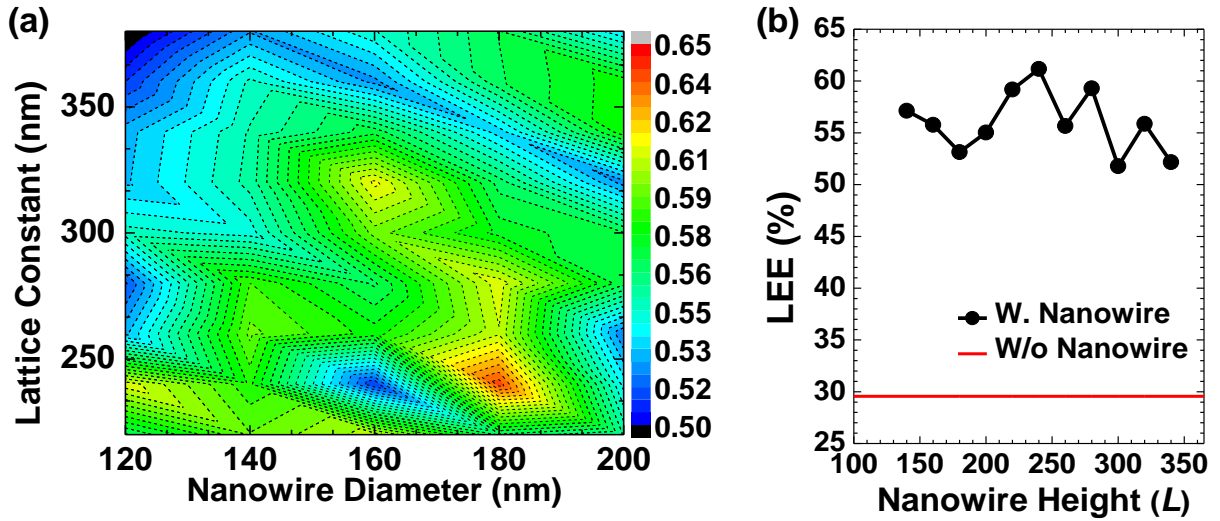


Figure 4.2: Contour plot of average LEE as a function of nanowire diameter (d) and lattice constant (a) at nanowire height (L)=240nm. (b) Variations of the average LEE vs. nanowire height (L) for a constant nanowire diameter (d) of 160nm and lattice constant (a) of 320nm.

4.4 Device Fabrication and Measurement

The fabrication of AlGaIn nanowire photonic crystal LED is described. AlGaIn nanowire photonic crystal structures were defined using e-beam lithography, BCl_3/Cl_2 plasma dry etching, and Tetramethylammonium hydroxide (TMAH) wet etching. Shown in Fig. 4.3 is the scanning electron microscopy (SEM) image of the fabricated nanowire photonic crystal structure, which has a diameter (d) \sim 160nm, lattice constant (a) \sim 320nm, and height (L) \sim 240nm. Ti (40 nm)/Al (120 nm)/Ni (40 nm)/Au (50 nm) was deposited as the top as well as the bottom n-metal contact, schematically shown in Fig. 4.1(b). The samples were subsequently annealed at 700°C for 30 seconds in nitrogen ambient.

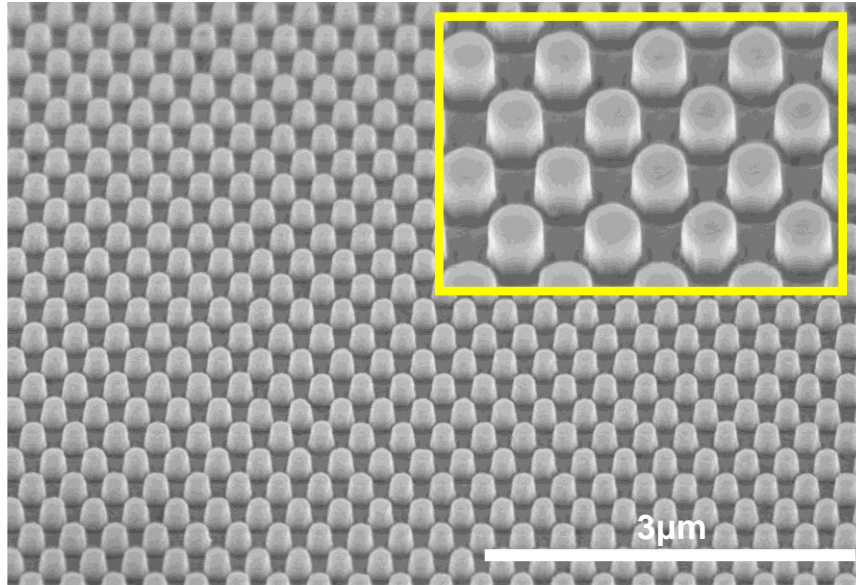


Figure 4.3: 45°-tilted view SEM image of hexagonal nanowire photonic crystal arranged in a triangular lattice with nanowire diameter (d) of 160nm and lattice constant (a) of 320nm.

The fabricated deep UV LEDs were measured directly on the wafer without any packaging. Figure 4.4(a) shows the current-voltage characteristics measured at room temperature. The device has an areal size of $50\mu\text{m} \times 50\mu\text{m}$. The device turn-on voltage is $\sim 9\text{V}$, and the current density reaches $\sim 20 \text{ A/cm}^2$ at $\sim 10\text{V}$. The current-voltage characteristics can be further improved by optimizing the tunnel junction structure. It is also noticed that the current-voltage characteristics are nearly identical for the deep UV LEDs with and without the incorporation of AlGaIn nanowire photonic crystals, shown in Fig. 4.4(a). Figure 4.4(b) shows the electroluminescence spectra measured at room temperature, which were collected by a UV optical fiber, analyzed using a high-resolution spectrometer and detected by a charge-coupled device. The peak emission wavelength is at $\sim 267\text{nm}$, which stays nearly constant with increasing current injections. A Newport 818-ST2-UV silicon photodetector with a Newport Model 1919-R power meter measured the output optical power. As shown in Fig. 4.4(c), an output power density $\sim 3 \text{ W/cm}^2$ was measured at a current

density of $\sim 23 \text{ A/cm}^2$, which is over two times higher than AlGaIn deep UV LEDs without the incorporation of nanowire photonic crystal structures.

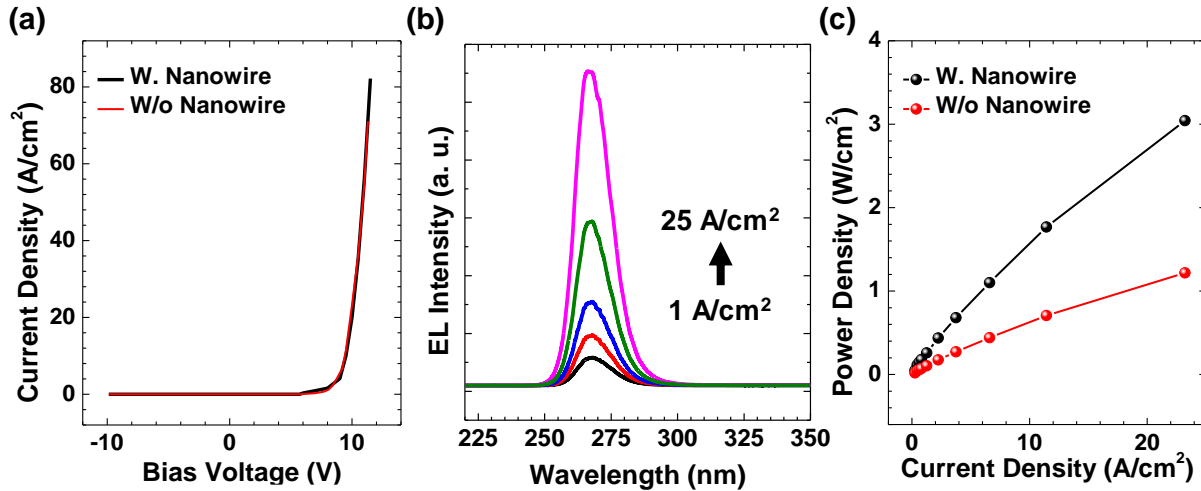


Figure 4.4: (a) Current-voltage characteristics for both with and without incorporation of nanowire photonic crystal. (b) Electroluminescence spectra were measured with different current injections. Inset shows no other defect-related emission. (c) Top emitting optical power density measurement using 10kHz repetition rate and 1% duty cycle.

The calculated EQE and WPE as a function of current density are shown in Figs. 4.5 (a) and (b), respectively. Peak EQE $\sim 5.4\%$ and WPE $\sim 3.5\%$ were measured at low current densities $0.5\sim 1 \text{ A/cm}^2$ for AlGaIn photonic crystal UV LED, which is approximately ~ 2.5 times higher compared to identical devices without the incorporation of photonic crystals. Given that the devices exhibit nearly identical current-voltage characteristics, the increase in WPE and EQE can be directly attributed to the enhanced LEE with the incorporation of nanowire photonic crystals, which is in good agreement with the simulation results shown in Fig. 4.2(b). A severe efficiency droop was measured with increasing current injection. The underlying causes for the efficiency droop may include electron overflow [120, 121, 124], Auger recombination [124, 182], carrier delocalization [183], and/or heating effect [125]. Since the efficiency droop occurs at a very low current density ($\sim 1 \text{ A/cm}^2$), the heating effect and Auger recombination are not likely the major

causes. On the other hand, electron overflow is expected to become significant in AlGaIn deep UV LEDs even at very low current densities due to the highly asymmetric charge carrier transport properties between electrons and holes in Al-rich AlGaIn. Similar efficiency droop was measured previously in AlGaIn deep UV LEDs. Due to the hole hopping conduction in the Mg impurity band, poor hole mobility was attributed to be the major cause [149]. It is expected that with further improvement of p-type conduction of AlGaIn and optimization of the tunnel junction, the efficiency droop of AlGaIn deep UV LEDs can be effectively reduced.

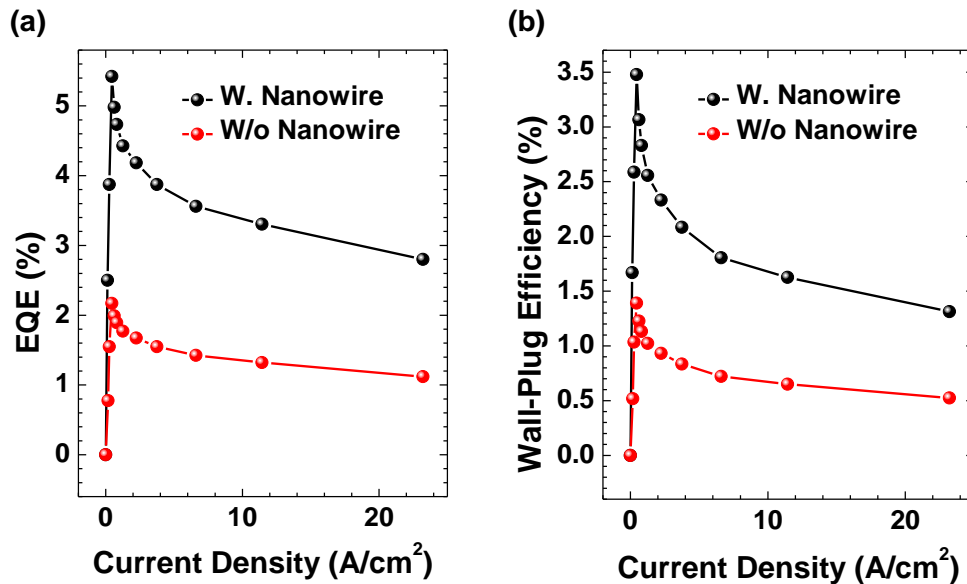


Figure 4.5: (a) External quantum efficiency (EQE) and (b) wall-plug efficiency (WPE) as a function of injected current density.

4.5 Summary

In summary, we have demonstrated AlGaIn tunnel junction deep UV photonic crystal LEDs operating at $\sim 267\text{nm}$. Significantly enhanced EQE and WPE were measured for AlGaIn deep UV LEDs with the incorporation of nanowire photonic crystal structures. Although this work was primarily focused on devices operating at 267nm, such a unique design can be readily

extended to AlGaN LEDs with higher Al compositions, i.e., shorter emission wavelengths, wherein TM polarized emission is more dominant. It is also observed that AlGaN deep UV LEDs suffer from severe efficiency droop, which is likely induced by electron overflow, due to the low hole mobility of Al-rich AlGaN. Enhanced efficiency and output power are expected by further optimizing the design, epitaxy, and fabrication of AlGaN tunnel junction photonic crystal LED structures in the future.

Chapter 5 Ultrahigh Q Microring Resonator Using a Single Crystal AlN on Sapphire Platform

5.1 Author Contribution and Copyright Disclaimer

The contents of this chapter were published in the Optics Letters in December 2019 [85], for which I retain the right to include it in this thesis/dissertation, provided it is not published commercially. The co-authors were Yi Sun, David Arto Laleyan, Ping Wang, Ayush Pandey, Xianhe Liu, Yuanpeng Wu, and Zetian Mi from the University of Michigan and Mohammad Soltani from Raytheon. I designed, fabricated, and partly conducted the work. Y. Sun, the first author, contributed to the fabrication. D. A. Laleyan, P. Wang, A. Pandey contributed to the material characterization. X. Liu and Y. Wu contributed to fabrication. The work was supervised by M. Soltani and Z. Mi, who contributed to the design of the experiments. This work was supported by the University of Michigan, College of Engineering and National Science Foundation (NNCI-1542081).

5.2 Introduction

Aluminum nitride (AlN) has emerged as a novel and versatile platform for integrated photonics enabling electro-optics and nonlinear optical devices for a broad range of applications [57, 60, 64, 67, 184-203], and optical transparency over a broad spectral range including UV, visible and infrared, due to its large bandgap (~ 6.2 eV) [204, 205]. Moreover, AlN belongs to a family of ternary and quaternary III-N alloys, i.e., Al(Ga, In)N, with a direct energy bandgap that

can be varied from 6.2 eV to 0.65 eV, which would allow material and refractive index engineering as well as monolithic integration of light sources, modulators, and detectors on the same platform [206, 207].

To date, however, the realization of low-loss waveguiding and high-quality resonators utilizing the AlN-on-sapphire platform has often been limited by the material quality for AlN grown directly on sapphire [198, 203]. Due to the large lattice mismatch, AlN grown on sapphire generally has $\sim 10^9$ cm⁻² or higher dislocation densities. The realization of high Q_{int} resonators has been further limited by the surface and sidewall roughness induced either during epitaxy and/or during the fabrication process. Recent studies have shown that the quality of AlN grown on sapphire can be dramatically improved by utilizing a nanopatterned sapphire wafer and annealing at ultrahigh temperature (up to 1700°C) [208, 209]. A high Q_{int} of ~ 2.5 million was measured in the telecom band using single-crystalline AlN epitaxially grown on a sapphire substrate with a partially etched structure [186]. Though partial etching can improve the intrinsic Q_{int} at larger radii and enhance the coupling to an external waveguide, a fully etched AlN waveguide is more desirable to provide higher optical mode confinement and enable more compact devices with smaller bend radii.

In this chapter, we perform a detailed investigation of the design, fabrication, and characterization of AlN-on-sapphire waveguides and microring resonators. All the structures are fully etched to achieve compact integration. By optimizing the design and fabrication process, the as-fabricated devices exhibit an ultra-high Q_{int} of 2.8×10^6 at a wavelength of ~ 1550 nm, indicating a propagation loss of less than 0.13 dB/cm.

5.3 Characterization, Design and Fabrication of Microring Resonator

The AlN-on-sapphire samples consist of 430 μm sapphire substrate with a $1 \mu\text{m} \pm 0.1 \mu\text{m}$ c-plane undoped AlN epi-layer. For our study, we designed a microring resonator with a radius of 60 μm and a width of 3 μm . We employed a pulley coupling scheme for the waveguide–resonator coupling, as shown in Fig. 5.1(a). This allows for a longer and stronger interaction length between the resonator and the external pulley waveguide and helps to increase the gap between the waveguide and the resonator, making the lithography and fabrication less problematic. However, an efficient waveguide–resonator coupling for a long interaction length requires phase matching between the mode of the resonator and the pulley waveguide. For that, we adjust the width of the pulley waveguide to be phase-matched to the mode of the resonator. Figures 5.1(b) and 1(c) show the simulated mode profile of the resonator and the pulley waveguide with the adjusted width for the phase-matching purpose. Figure 5.1(d) shows the simulated coupling Q-factor between the waveguide and the resonator using the coupled-mode theory [210] for different pulley angles and coupling gaps. As seen from this figure, we can increase the pulley angle to get the required coupling even for larger gaps. The coupling Q-factor value needs to be close to the Q_{int} of the resonator for strong waveguide–resonator coupling interaction [211]. Using these simulations, we design microring resonators with different pulley angles and waveguide–resonator gaps for the device fabrication.

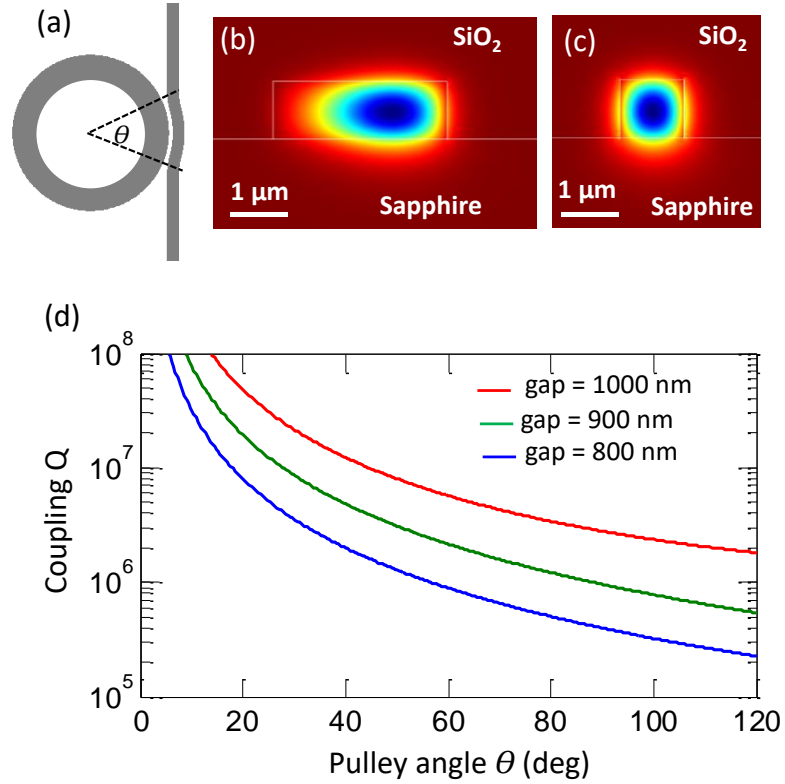


Figure 5.1: (a) Schematic of AlN-on-Sapphire ring resonator coupled to an external waveguide with a pulley coupling scheme. (b) Cross-section of the electric mode profile of an AlN-on-Sapphire ring resonator with an internal radius of 60 μm , width of 3 μm , and height of 1 μm . (c) Mode profile of the optical waveguide at the pulley coupling region, with a waveguide width of 1100 nm. The waveguide width in the pulley region is adjusted to be phase-matched to the mode of the resonator. (d) Calculated coupling Q-factor vs. the pulley angle for different waveguide resonator gaps.

To fabricate microring resonators, we used commercially available AlN-on-sapphire wafers from DOWA Electronics Materials Co. Ltd. Since the surface, and crystalline quality of the material is crucial for achieving high Q-factors, we first characterize the AlN-on-sapphire wafers. Figure 5.2(a) shows the atomic force microscopy (AFM) image of the AlN-on-sapphire that was used primarily in this study, which has a root mean square (RMS) roughness of ~ 0.2 nm over a $5 \times 5 \mu\text{m}^2$ area. The x-ray diffraction (XRD) rocking curve measurement reveals an FWHM linewidth of ~ 60 and ~ 1500 arcsec for the (0002) and (10 $\bar{1}$ 2) planes, respectively, shown in Figs. 5.2(b), indicating relatively good crystalline quality.

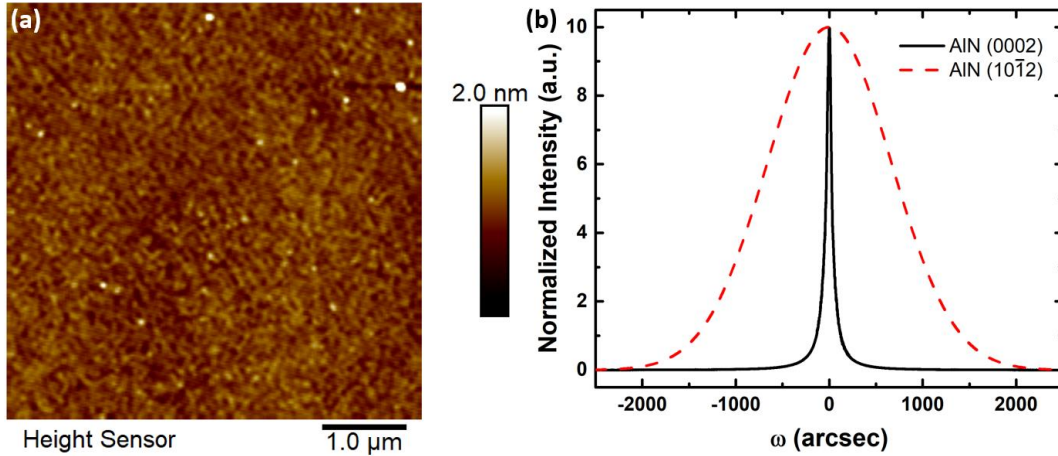


Figure 5.2: (a) AFM images of AlN grown on a sapphire show an RMS roughness of ~ 0.2 nm. (b) XRD (0002) and (10 $\bar{1}2$) plane rocking curves for AlN on sapphire samples.

Since AlN is a hard material to etch, especially for a large etch depth of one micron, we employ two hard mask layers in our fabrication process to define the patterns on the AlN layer. The first hard mask is SiO₂ for etching the AlN and the second hard mask is Al₂O₃ for etching the SiO₂ hard mask. A schematic illustration of the fabrication process is shown in Fig. 5.3(a). The process starts with the deposition of a 500 nm SiO₂ hard mask layer on top of an AlN layer by plasma-enhanced chemical vapor deposition (PECVD). 5 nm of Ti is evaporated on top of the SiO₂ hard mask to avoid the charging effect during the electron lithography process. Then, using an electron beam lithography system (JEOL JBX-6300FS) with PMMA 495 A2 and PMMA 950 A2 resist and a lift-off process, device patterns are defined on a 25 nm Al₂O₃, which is the second hard mask. SiO₂ is etched with fluoride-based chemistry in a reactive ion etching (RIE) system (LAM 9400) using this mask layer, as shown in Fig. 5.3(b). The etching selectivity of SiO₂ and Al₂O₃ is measured to be larger than 20:1, which can therefore define a 500-nm-thick SiO₂ hard mask by etching. The dry etching of AlN is performed in a separate RIE system (Oxford Plasmalab System 100) with Cl₂/Ar-based chemistry using SiO₂ as hard masks, as shown in Fig. 5.3(c). The etching rate of AlN is ~ 120 nm/min and the etch selectivity of AlN and SiO₂ is measured to be ~ 3 :1. Figures 5.3(d)

and 3(e) show the scanning electron microscope (SEM) images of the fabricated ring resonator. The fabrication process continues with the deposition of 3 μm SiO_2 by PECVD as the cladding layer on top of an AlN microring and waveguides.

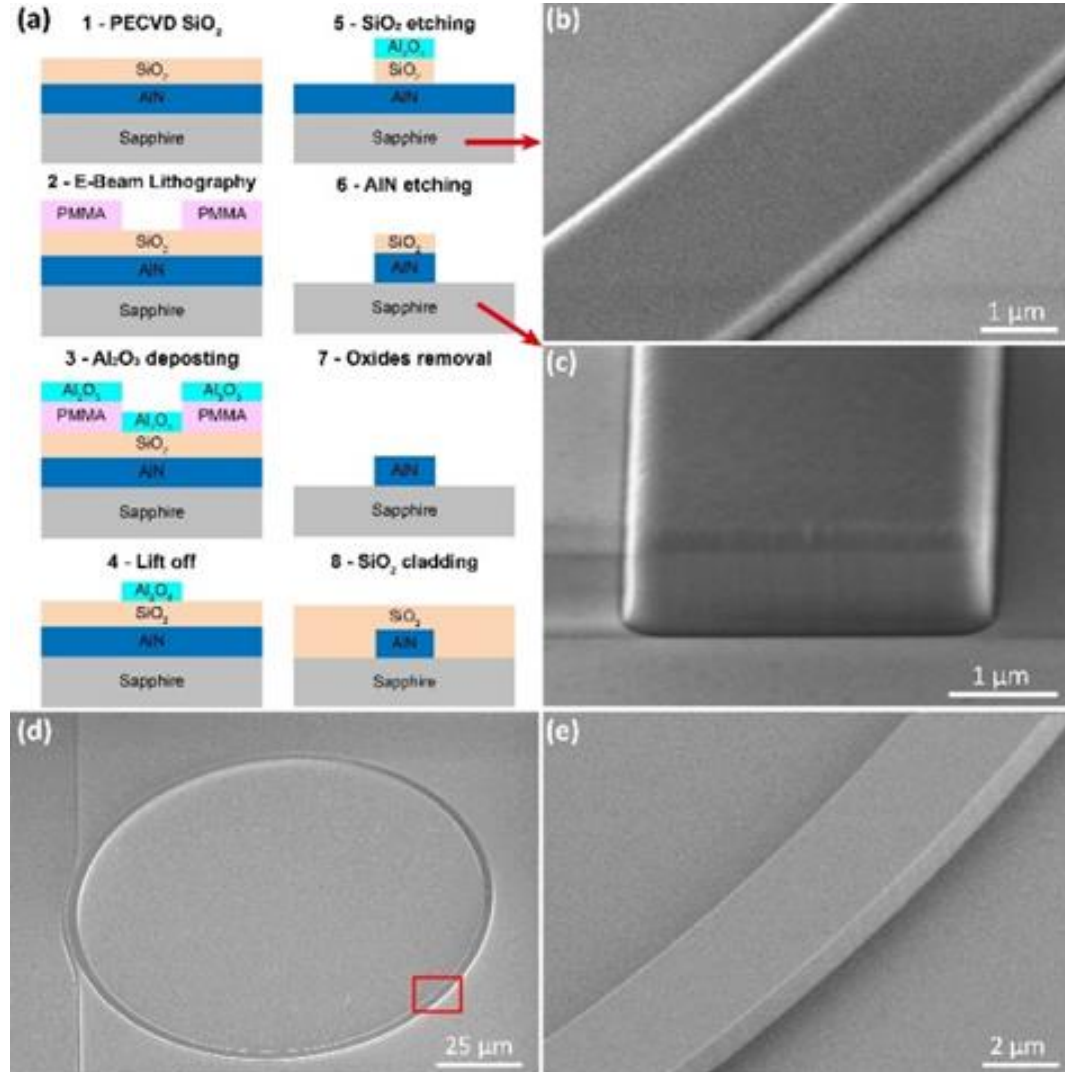


Figure 5.3: (a) Schematic illustration of the fabrication process for the AlN-on-sapphire microring resonator. (b) SEM image of the devices after SiO_2 etching at step 5 in (a). (c) SEM image of the devices after AlN etching at step 6 in (a). (d) SEM image of the fabricated AlN-on-sapphire microring resonator and associated waveguide after SiO_2 removal at step 7 in (a). (e) Enlarged SEM image for the red box area in (d), showing the resonator's vertical and smooth sidewall after etching.

Since the gap between the microring resonators and associated waveguides is less than 1 μm with a depth of 1 μm , traditional silane-based SiO_2 deposition by PECVD often results in air voids, also known as the keyhole effect, in the waveguide–resonator gap. We investigated the influence

of the SiO₂ trench refill profile by using different SiO₂ deposition methods and recipes. Silane and nitrous oxide gases have been widely used for SiO₂ deposition in PECVD, but they often result in a severe keyhole effect when refilling small trenches, as shown in Fig. 5.4(a). This keyhole effect between the microring resonator and waveguide may introduce light scattering, weaken the coupling, and further degrade the Q-factor of the microring resonators. On the other hand, tetraethyl orthosilicate (TEOS) is a highly conformal oxide and can provide a much better trench refill profile [212]. By depositing SiO₂ using TEOS-based PECVD, we achieved a much-improved trench-refilling profile from the cross-sectional SEM image shown in Fig. 5.4(b). It is also seen that a vertical sidewall of the AlN waveguide (sidewall angle around 85°) is achieved after etching. Subsequently, the sample is diced, and the facets of the chip are polished for edge coupling of laser light.

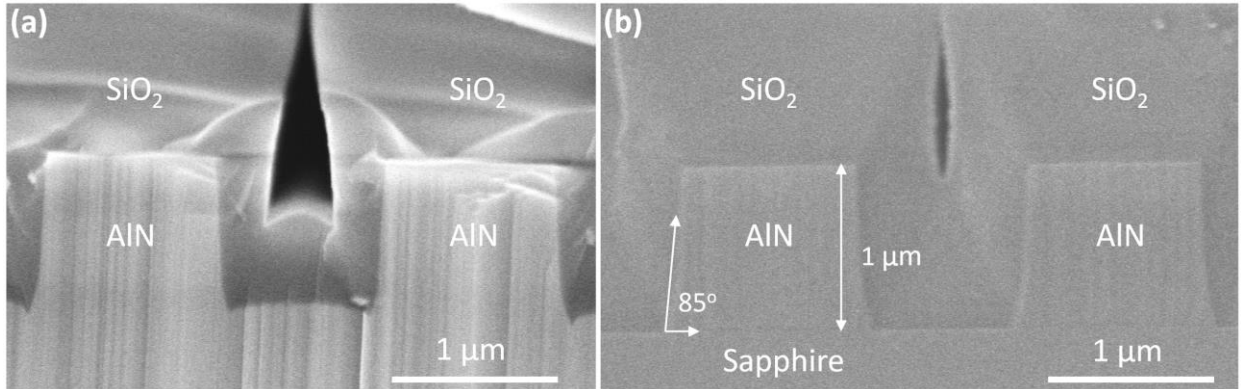


Figure 5.4: (a) and (b) SEM images of trench refill capability for silane-based and TEOS-based SiO₂ deposition, respectively. The dimension of the trench is 1 μm deep and 1 μm wide.

5.4 Measurement of Demonstrated Microring Resonator

The performance of microring resonators is characterized through transmission measurements. Tapered lens fibers with a beam spot of 2.5 μm are used to couple light in and out of the chip. The waveguides at the facet of the chip are an inverse taper design with an entrance waveguide width

of 800 nm. Our measurement shows an insertion loss of 5 dB per facet. For the waveguide–resonator coupling, we have different gap widths ranging from 800 to 1100 nm and pulley angles. Figure 5.5(a) shows the measured spectrum for the ring resonator with a 60 μm radius, a gap of 800 nm, and a pulley coupling angle of 20 degrees. The zoomed view in Fig. 5.5(b) shows that there is a resonance splitting due to the resonator’s clockwise (CW) and counterclockwise (CCW) mode coupling induced by sidewall roughness. Fitting these results to the coupled-mode theory and including CW and CCW coupling [82], we can predict the intrinsic quality factor as high as 2.8×10^6 , which is the highest reported value for fully etched AlN-on-sapphire resonators at the telecom wavelength to the best of our knowledge, as shown in Fig. 5.6.

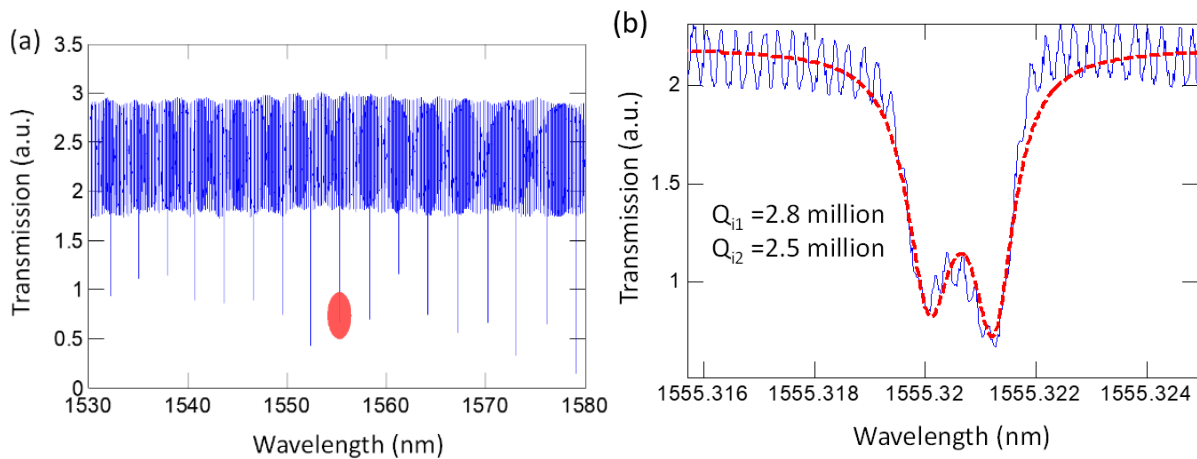


Figure 5.5: (a) Spectrum of the resonators near 1550 nm, where a strong coupling is observed. The gap between the waveguide and the resonator is 800 nm, the pulley angle is 20 degrees, and the waveguide width at the pulley region is 1100 nm. (b) A zoomed view of one of the resonances at the solid red circle in (a), wherein the resonance shows the coupling between the degenerate CW and CCW modes of the resonator due to sidewall roughness scattering. A fitting of this spectrum to theoretical spectrum using coupled-mode theory shows intrinsic Q for both CW and CCW modes.

The propagation loss is determined to be 0.13 dB/cm for a Q-factor of 2.8×10^6 . The propagation loss can be further reduced by minimizing the sidewall roughness during the fabrication process and by improving the quality of AlN-on-sapphire during epitaxy.

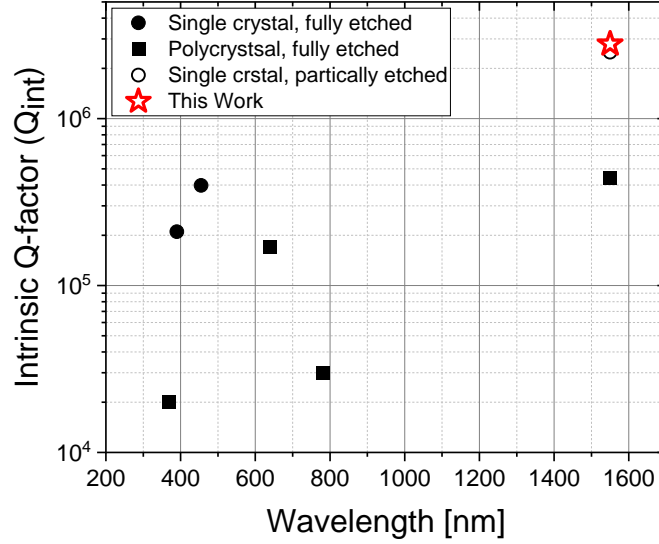


Figure 5.6: Previously reported Q-factor of AlN-on-sapphire microring resonators [60, 186, 190, 205, 213].

5.5 Summary

In summary, we have demonstrated high Q_{int} (2.8×10^6) microring resonators at 1550 nm utilizing single-crystal AlN film grown directly on a sapphire substrate, corresponding to a propagation loss of 0.13 dB/cm. With further optimization of the material crystalline quality and fabrication process, resonators with even higher Q-factor value can be achieved in a broader wavelength range, providing a unique platform for integrated photonics and quantum photonics from UV to the near-infrared. Future work will focus on achieving devices with electro-optic and nonlinear optic functionalities in the infrared and visible and UV wavelengths.

Chapter 6 Demonstration of Green and UV Wavelengths High Q Aluminum Nitride on Sapphire Microring Resonators Integrated with Microheaters

6.1 Author Contribution and Copyright Disclaimer

The contents of this chapter were published in the Applied Physics Letters in May 2021 [86], for which I retain the right to include it in this thesis/dissertation, provided it is not published commercially. The co-authors were Yi Sun and Zetian Mi from the University of Michigan and Mohammad Soltani from Raytheon. I designed, fabricated, measured, and authored most of the work. Y. Sun contributed to the fabrication process. The work was supervised by M. Soltani and Z. Mi, who contributed to the design of the experiments. This work was partly supported by the College of Engineering at the University of Michigan.

6.2 Introduction

PICs at UV and visible wavelengths are important for a wide range of applications, including sensing, underwater communication [52], optogenetics [53], UV spectroscopy [54, 55], and quantum information processing [56]. A variety of PIC platforms have been investigated for operation at these wavelengths including LiNbO₃ [58, 214-216], SiN_x [217, 218], Al₂O₃ [219, 220], TiO₂ [221-223], and diamond [224, 225]. Despite many progresses made on these platforms, they suffer from various issues, namely: lack of electro-optic tuning [57], photorefractive damage even at small powers for such wavelengths [59], and/or large absorption loss when going to shorter wavelengths [226].

A promising alternative material is AlN [190, 201, 226], which belongs to the III-N material group and has a wide direct bandgap ($\sim 6.1\text{eV}$) with both second (χ^2) and third (χ^3) order optical nonlinearities. It also allows to demonstrate Al(Ga)N based passive/active optoelectronic functionalities [24]. Recently, significant progress has been made in making low loss AlN PIC by demonstrating high Q resonators at IR ($\sim 1550\text{nm}$) [85, 186], NIR ($\sim 780\text{nm}$) [64], and UV ($\sim 396\text{nm}$) [205]. In this letter, we tap on two other important wavelengths of 532 nm and 369.5nm within the Visible-UV spectra and demonstrate high Q single crystal AlN on sapphire microring resonators for these wavelengths. Since tunable lasers are less available at these wavelengths, we employ another technique by integrating microheaters with the resonators and tuning the resonance across a fixed wavelength using thermo-optic tuning.

6.3 Characterization, Design and Fabrication

For the device design and fabrication, we use AlN-on-sapphire template, which consists of $430\mu\text{m}$ sapphire substrate with $1\mu\text{m} \pm 0.1\mu\text{m}$ c-plane undoped AlN epi-layer. Figure 6.1(a) shows the measured refractive index of AlN film spanning from UV to IR wavelength with a spectroscopic ellipsometer. Both ordinary and extraordinary refractive index of the transparent region are extracted by fitting with Cauchy dispersion for three different angles of incidents: above, near, and below Brewster angle [227, 228]. Figure 6.1(b) shows PL with $\lambda=193\text{nm}$ pump laser where the signal was collected using a high-resolution spectrometer and detected by a charge-coupled device. No defect-related emission was found in the PL measurement up to visible wavelength, which confirms high-quality single crystallinity with low defect and dislocation densities [28, 229].

Microring resonators with a $60\mu\text{m}$ radius and height of 550nm were designed in this study. Five different rings with slightly different widths were considered, all coupled to the same waveguide, shown in Fig. 6.1(c). This helps the experimentation with a single wavelength laser when tuning the resonance of these rings to coincide with the laser resonance. In addition, we used a pulley coupling scheme between the waveguide and the resonators to provide strong waveguide-resonator coupling without the need to reduce the waveguide-resonator gap to extra small sizes. An additional design consideration to improve the waveguide-resonator coupling is to cover the waveguide and the resonator surfaces with a thin layer of Al_2O_3 which has a refractive index larger than that of SiO_2 . This layer also fills the coupling gap region between the waveguide and the resonator and allows more leakage of the optical modes to cladding, thereby providing a stronger mode overlap between the waveguide and the resonator modes. The width of the coupling waveguide and the waveguide-resonator gap are optimized to provide phase matching and strong mode overlap between the mode of the waveguide and that of the resonator. Figure 6.1(d) shows the simulated mode profiles of the waveguide and the resonators buried on SiO_2 cladding, and Fig. 6.1(e) shows the cross-section of the ring resonator with the thermal heater.

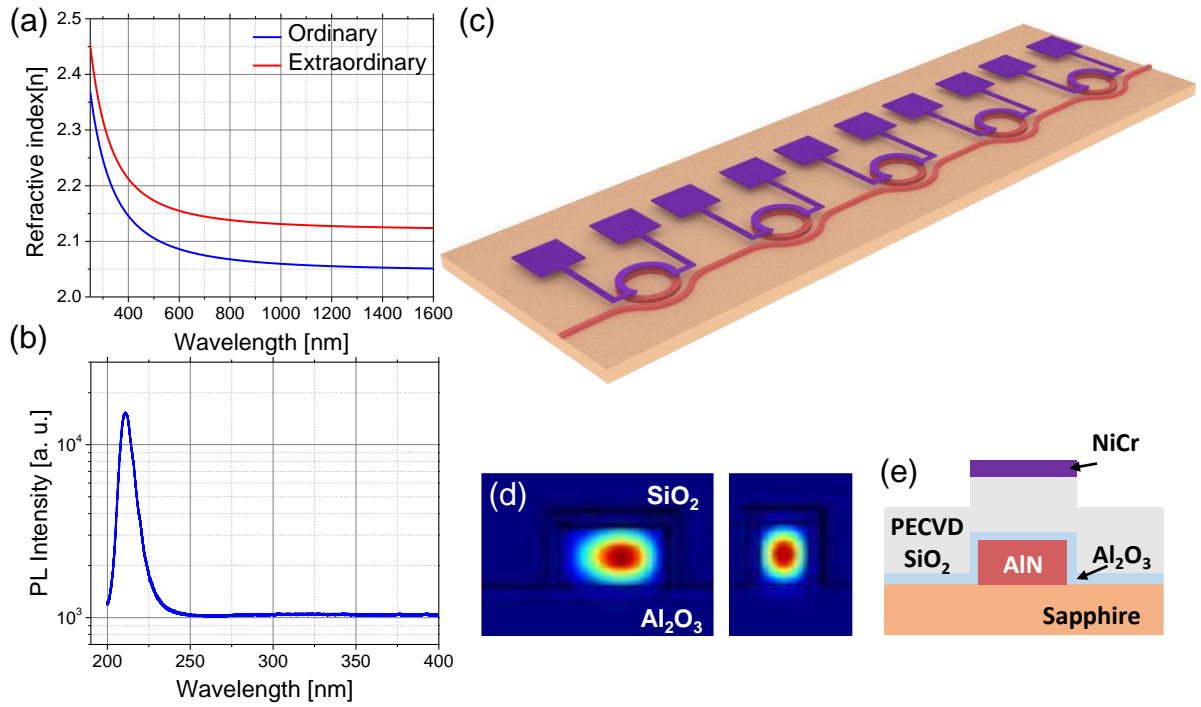


Figure 6.1: (a) Measured refractive index and (b) photoluminescence spectrum of AlN-on-sapphire. (c) Schematic illustration of microring resonators with thermal heater. (d) Mode profiles of the ring resonator and bus waveguide at pulley coupling region. The width of the bus waveguide and ring resonator are adjusted to satisfy the phase-matching condition. (e) Cross-section of microring resonator.

For the fabrication of the resonators, initially, the AlN layer is etched down to a thickness of 550nm using Cl_2/Ar based inductive coupled plasma reactive ion etching (ICP-RIE). Then, microring resonator patterns are defined using e-beam lithography with two layers of the hard masks. First, a 500nm thick PECVD SiO_2 mask is deposited on the AlN layer. For patterning, an electron beam lithography system (JEOL 6300FS) with bilayer PMMA e-beam resists and discharge H_2O anti-charging layer were used. After patterning, 30nm of Al_2O_3 deposition and a lift-off process were followed. SiO_2 mask was etched by fluoride-based chemistry ICP-RIE using Al_2O_3 mask layer, followed by AlN etching with Cl_2/Ar chemistry based ICP-RIE. Then, buffered HF was used to remove the two layers of the hard masks. Figures 6.2(a) and (b) show the SEM image of the defined ring resonator and its sidewall. Subsequently, 130nm Al_2O_3 with atomic layer deposition (ALD) and 1 μm of PECVD SiO_2 were deposited for the cladding layer. For the thermal

microheater, 150nm NiCr was patterned on top of the microring resonator using e-beam lithography, and Ti (10nm) / Al (800nm) / Au (90nm) were evaporated as metal contact pads using photolithography. Finally, dicing and polishing to expose the waveguide facet for edge coupling were performed. Figure 6.2(c) shows the optical microscope image of the fabricated microring resonators.

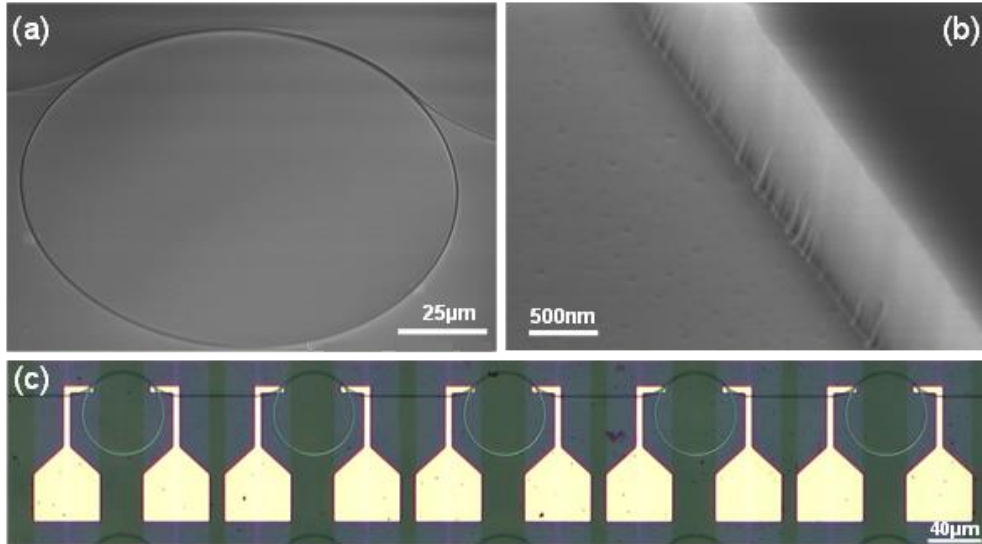


Figure 6.2: SEM image of (a) a fabricated AlN-on-sapphire microring resonator and (b) magnified image of waveguide sidewall. (c) Optical microscope image of demonstrated microring resonators. Five microring resonators with different widths are coupled to one bus waveguide.

6.4 Transmission Characterization of Demonstrated Microring Resonators

To characterize the fabricated resonators at the green (523nm) and UV (369.5) wavelengths, the laser light was sent to the waveguide coupled to these resonators, and light transmission through the waveguide was monitored. Since the laser wavelength is fixed and not tunable, we use the thermo-optic tuning of the resonator and sweep its resonance across the laser wavelength while measuring the optical transmission through the waveguide. To calibrate the thermo-optic relationship at green wavelength, we first characterize the relationship of temperature-based resonance shift at NIR, ~780nm, with a high-performance tunable laser and apply a bias to the

microheater. Figure 6. 3(a) shows the normalized transmission characteristics of the five resonators using a tunable laser source at NIR. After applying a bias at 5V, resonance wavelengths red-shifted due to the thermo-optic effect. In addition, given the relatively high thermal conductivity of the sapphire substrate, resonances of the other four devices shift due to thermal crosstalk. Despite thermal crosstalk, assuming the highest temperature change at the target device, two resonances can be found labeled as TE₀₀ and TE₁₀, showing the highest resonance shift. The fundamental and higher-order modes can be identified with FSR, where higher-order modes have a higher group index and smaller FSR. As shown in Fig. 6.3(a), with 5V applied bias, 16.67mW, the target resonance shifts ~48pm, whereas other resonances from other devices shift ~18pm, which is a factor of 2.67 times lower. Figure 6.3(b) shows the relationship between the applied voltage square and resonance shift, which shows a clear linear relationship.

For resonance characterization using thermo-optic sweeping, we first need the relation between the resonance shift and the applied voltage to the heater and calibrate this relation for the green and UV wavelength. The relation between the resonance and the temperature change can be expressed below.

$$\Delta\lambda_{res} = \lambda_{res} \frac{\Delta n_{res}}{n_{res}} = \frac{\lambda_{res}}{n_g} \frac{\delta n_{res}}{\delta T} \Delta T = \frac{\lambda_{res}}{n_g} \frac{\delta n_{res}}{\delta T} \alpha \frac{\Delta V^2}{R} \quad (\text{Equation 6.1})$$

where $\Delta\lambda_{res}$ is the resonance shift due to ambient temperature change ΔT , n_{res} is the effective refractive index of resonance, $\delta n_{res}/\delta T$ is thermo-optic coefficient [230], n_g and λ_{res} are group index and resonance wavelength, respectively. Here, we assume thermal expansion is negligible. Considering only the TE mode, we used the measured ordinary refractive index for our simulations to calculate the group index needed for Eq. (6.1). For this calculation, we used a finite difference eigenmode solver within Lumerical MODE Solution, where results are listed in

Table 6-1. To define the relationship between resonance wavelength and applied voltage, ΔT can be represented as $a\Delta V^2/R$ where a is conversion efficiency from electrical to thermal heat power, and R and ΔV are microheater resistivity and applied voltage. With the knowledge of the listed values in Table 6-1 for the NIR wavelength, and the gradient of Fig. 6.3 (b), the value of a/R can be extracted, which is constant and independent from laser wavelength. Furthermore, a/R can be used to calculate the wavelength offset as a function of applied voltage at green and UV wavelength along with listed values in Table 6-1 at those wavelengths.

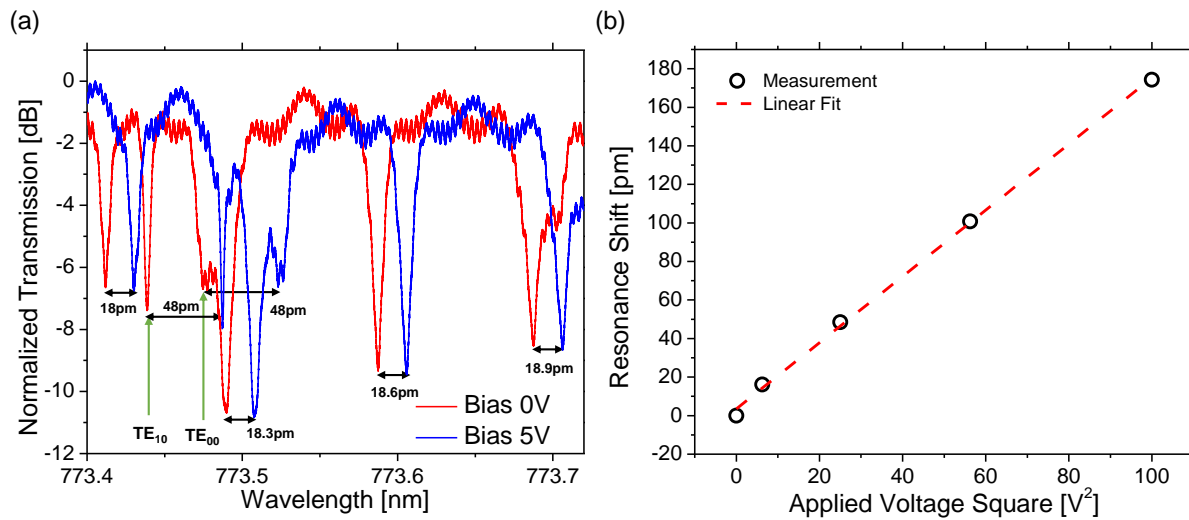


Figure 6.3: (a) Normalized transmission characteristic using tunable laser around 780nm with two different bias voltages, 0V and 5V. (b) Measured resonance wavelength shift as a function of applied voltage square showing a linear relationship.

Resonance characteristics with fixed 532nm laser are observed with a dimension of 1 μ m ring width, 500nm bus waveguide width, 230nm gap, and 90° pulley angle, shown in Fig. 6.4 (a), where red dash line shows the transmission characteristic based on coupled-mode theory. The resonance shows a near-critical coupling condition with extracted Q_{int} of 147,000 and 7.3dB/cm propagation loss at 532nm. To the best of our knowledge, this is the first measured Q_{int} at a green wavelength for the AlN-on-sapphire microring resonator. The same calibration is done at UV

wavelength with fixed 369.5nm laser shown in Fig. 6.4(b). The resonance characteristics are observed with 800nm ring waveguide width, 530nm bus width, 200nm gap, and 90° pulley angle. Since microring resonator design targets green wavelength, the transmission characteristic shows a significant under-coupling condition with extracted Q_{int} of 25,500 with a propagation loss of 60.4dB/cm.

Table 6-1: Parameter values for calibrating resonance characteristics at green and UV wavelengths.

Structure	NIR ($\lambda \sim 780\text{nm}$)	Green ($\lambda \sim 532\text{nm}$)	UV ($\lambda \sim 369.5\text{nm}$)
n_g	2.1071	2.0922	2.0826
$\delta n_{\text{res}}/\delta T$ ($\times 10^{-5}/\text{K}$) [230]	2.9548	3.2833	4.1574

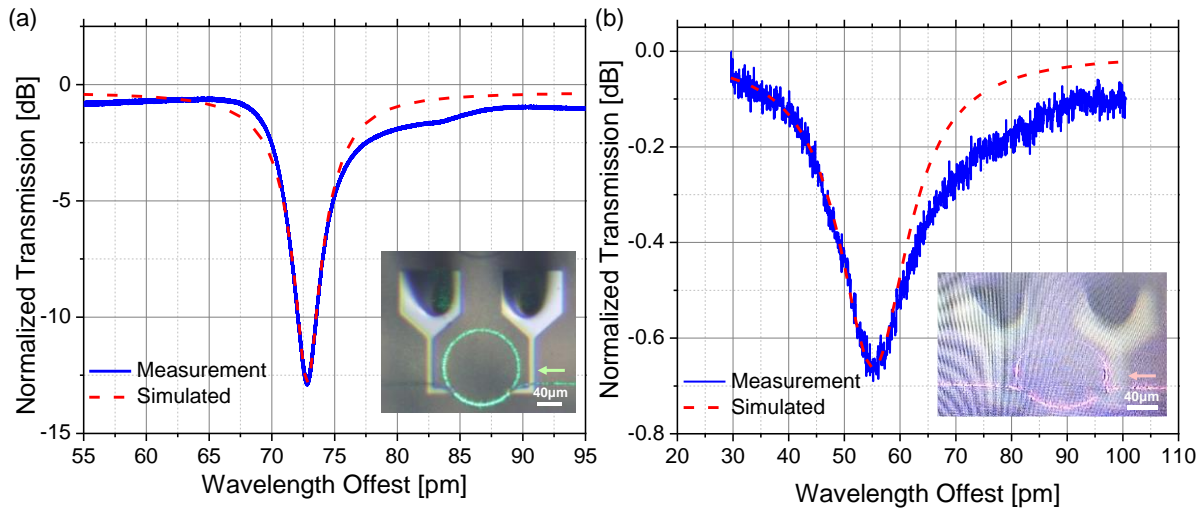


Figure 6.4: (a) Normalized transmission characteristic as a function of calibrated wavelength offset at (a) green wavelength (532nm fixed laser) and (b) UV wavelength (fixed 369.5nm laser). The red dash line shows the simulated transmission characteristic based on coupled-mode theory. The inset of each figure shows the optical microscope image at the resonance condition, where the arrow shows laser input.

Figure 6.5 shows the step response of our thermal heater. The width and thickness of our microheater are $1.5\mu\text{m}$ and 150nm , respectively. To measure the step response, the laser wavelength is fixed in the linear region of resonance spectra, and the output optical power is monitored while applying the pulse signal. To keep the laser wavelength in the linear region, a small pulse signal is applied to the heater. The measured rise time and fall time show a significant difference, which are $11\mu\text{s}$ and $190\mu\text{s}$, respectively.

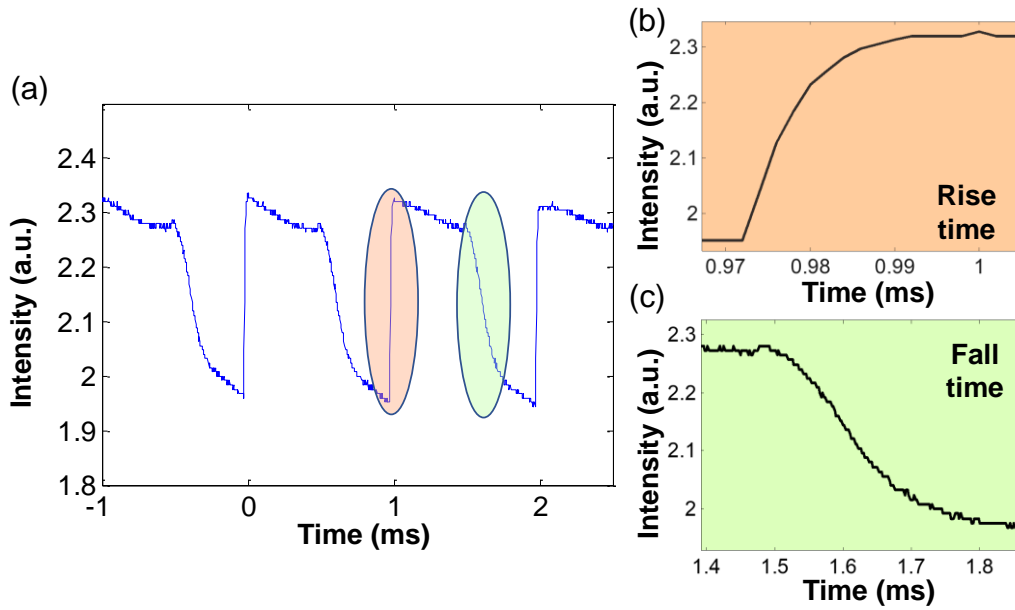


Figure 6.5: (a) Measured step response of the NiCr microheater and magnified view of (b) rise time and (c) fall time response.

6.5 Summary

In summary, we demonstrate a high-Q AlN-on-sapphire microring resonator at green (532 nm) and UV (369.5 nm) wavelengths. For the resonator Q characterization, we employed a thermo-optic resonance tuning technique by integrating microheaters with the resonators to sweep the resonance across these laser wavelengths. Using our calibrated thermo-optic tuning approach, we measured a Q_{int} of 147,000 (~ 7.3 dB/cm propagation loss) at 532nm, which to our

knowledge, is the first demonstration for this wavelength. In addition, with the same calibration technique, we measured a Q_{int} of 25,500 (~ 60.4 dB/cm propagation loss) at 369.5nm. We also investigated the effect of thermal crosstalk on adjacent resonators when heated up by their microheaters. The relatively large thermal conductivity of the sapphire substrate results in considerable thermal crosstalk on resonators at mm distance away from the microheater. Our study shows promises and further insight on using the AlN-on-sapphire platform for large-scale integrated photonics in the UV and visible range.

Chapter 7 Enhanced Pockels Effect AlN Microring Resonator Modulator Based on AlGaN/AlN Multiple Quantum Wells

7.1 Author Contribution and Copyright Disclaimer

The contents of this chapter were submitted to ACS photonics in March 2022. I retain the right to include it in this thesis/dissertation, provided it is not published commercially. The co-authors were Ping Wang, Yi Sun, Sritoma Paul, Jiangnan Liu, Mack Kira and Zetian Mi from the University of Michigan and Moe Soltani from Raytheon. I designed, fabricated, measured, and authored most of the work. P. Wang contributed to the growth of the MQW structure, Y. Sun and J. Liu contributed to the fabrication process, S. Paul contributed to the band structure simulation and M. Kira contributed to manuscript writing. The work was supervised by M. Soltani and Z. Mi, who contributed to the design of the experiments. This work was supported by the College of Engineering at the University of Michigan.

7.2 Introduction

PICs based on III-N materials, which includes $\text{Al}_x\text{Ga}_{1-x}\text{N}$, are an emerging promising technology platform with a wide range of optical transparency from UV to mid-IR wavelengths. This platform enables active and passive PIC components with high power handling properties and second- and third-order nonlinear optical properties [206, 207, 231-236]. These features allow a variety of linear and nonlinear PIC devices operating over a broad range of wavelengths. In the III-N family, AlN PIC has been extensively pursued recently with demonstrated works on high-Q resonators [60, 85, 186, 190, 205, 213], EO modulators [64, 237], on-chip frequency comb, and second/third harmonics generation [189, 191, 198, 204, 238, 239].

Despite the attractive characteristics of AlN, its Pockels EO coefficient, related to second-order susceptibility, is weak and limited to r_{13} and r_{33} around 1 pm/V [64-67]. As a comparison, Fig. 7.1 shows the EO coefficients of some photonic materials and their operational wavelength window. Though materials such as LiNbO₃ or polymers have a strong Pockels effect, they are subject to photorefractive damage at shorter wavelengths and higher optical powers. Therefore, at shorter wavelengths (UV/vis/near IR), AlN remains quite promising, and the enhancement of its EO coefficient will make it more attractive.

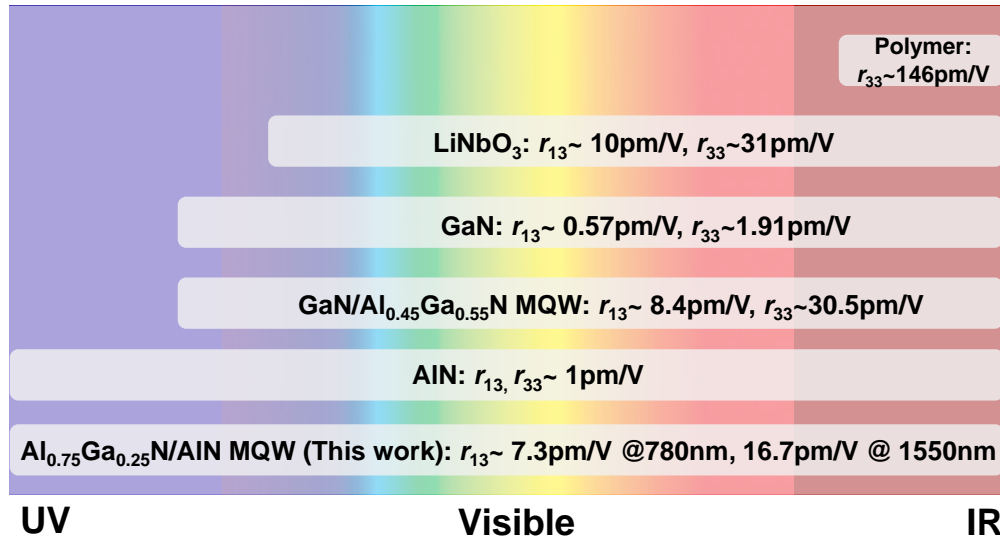


Figure 7.1: Pockels coefficient (r_{13} and r_{33}) for different materials; Polymers [240-243], LiNbO₃ [74-81, 244], GaN [73], GaN/AlGa_N MQWs [71, 72], AlN [65-67] and our study (AlGa_N/AlN MQWs).

Several efforts have been made to increase the EO effect in III-N semiconductors. Although many approaches, such as quantum confined stark effect (QCSE), have been very promising, they have limited the operation near the bandgap of the quantum well [68]. Another method employed the third-order susceptibility of III-N semiconductors and applied an external DC electric field along the optical axis to induce an electric-field induced second-order effect [69, 70]. A more recent work utilized a high internal polarization field based on GaN/AlGa_N superlattices to

produce ten times higher Pockels coefficient than bare GaN, shown in Fig. 7.1, and provided additional freedom for manipulating the EO effect [71, 72]. The Pockels coefficient of GaN/AlGaN MQWs from Ref. 71 is competitive with LiNbO₃ and offers even higher values near the band edge due to the resonance effect. However, most studies are limited to GaN film, with no demonstration of the effect in an integrated photonic platform suitable from UV, visible to IR.

Here, we demonstrate an enhanced Pockels effect in an AlN-integrated photonic platform by employing high Al composition AlGaN/AlN MQW heterostructures regrown on top of an AlN layer on a sapphire substrate. This enhancement is based on the high second-order susceptibility of the MQW layer due to the large built-in polarization field. For the enhancement characterization, we design and fabricate MRMs with MQW layers and measure the resonance shift versus the applied voltage. By comparing AlN MRMs with similar dimensions but without MQWs, we observe 2.16 times and 1.56 times enhancement of resonance shift at 1550nm and 780nm wavelengths, respectively. The extracted second-order susceptibilities of AlGaN/AlN MQWs show an order of magnitude higher than AlN. We also measured the 3dB bandwidth of the demonstrated MRM with the MQW layer, which shows 27 GHz bandwidth for the 1550nm wavelength modulator.

7.3 Material Growth and Characterization

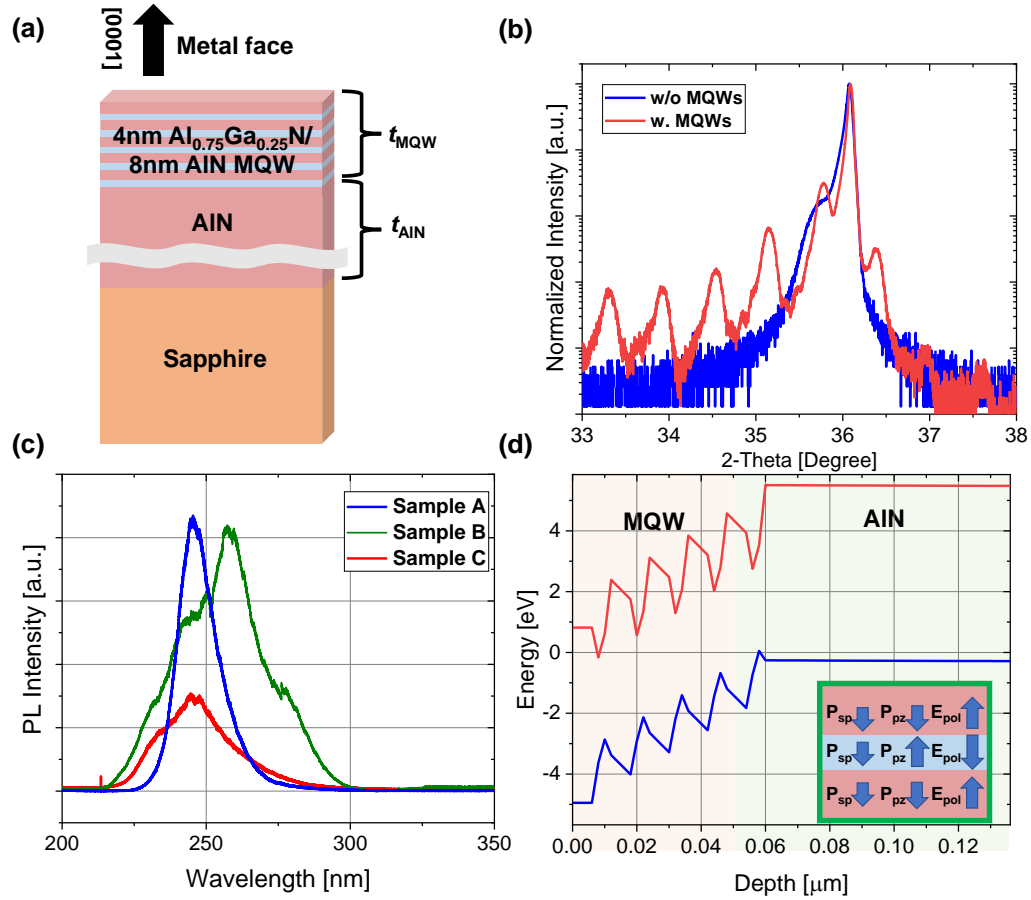


Figure 7.2: (a) Schematic illustration of regrown AlGaIn/AIn MQWs on AIn-on-sapphire. (b) High-resolution XRD patterns of $2\theta/\omega$ scan for samples of with (w.) MQWs and without (w/o) MQWs along the (0002) direction. The satellite diffraction peaks can be observed from the MQW sample, which indicate a good periodicity of MQWs. (c) Photoluminescence spectrum of 3 regrown samples. (d) Simulated band structure of regrown AlGaIn/AIn MQWs on AIn. The inset shows the built-in field in the QW and barriers due to spontaneous and piezoelectric polarization.

Figure 7.2(a) shows a schematic of metal-face AlGaIn/AIn MQWs regrown on the AIn-on-sapphire template from DOWA Holdings Co. Ltd. The MQWs are grown using a Veeco GENxplor MBE system equipped with a radio frequency plasma-assisted nitrogen source and Knudsen effusion cells for Ga and Al sources. Initially, AIn is etched down to $\sim 400\text{nm}$ and, subsequently, a $\sim 100\text{nm}$ AIn buffer layer and AlGaIn/AIn MQWs are grown on top. To investigate the effect of MQWs at different wavelengths, we grow 5 MQWs (Samples A and C) and 3 MQWs (Sample B) with similar growth conditions. The thickness of each QW and barrier are 4 nm and 8 nm, and the

total thickness of all waveguides is ~550nm. The EO effects of Sample A and B are measured at telecom wavelength (1550nm) regime, whereas Sample C is measured at 780nm regime. The characteristics of each sample are listed in Table 7-1. We expect a Pockels coefficient enhancement when using a lower Al composition (i.e., smaller x) in the $\text{Al}_x\text{Ga}_{1-x}\text{N}/\text{AlN}$ MQWs, as it provides a higher internal polarization field. However, due to the larger lattice mismatch, dislocation and defect-based optical loss become significant with low Al composition AlGaN/AlN MQWs. Thus, in this study, the thickness of MQWs and their Al compositions are optimized to provide a larger polarization field and low propagation loss for the waveguide and the resonator.

Figure 7.2(b) shows a high-resolution X-ray diffraction (XRD) 2 theta-omega scans of (0002) plane for representative regrown AlGaN/AlN MQWs (with MQWs) and AlGaN epilayer (without MQWs) on the AlN templates. The same growth conditions are used to obtain an Al composition of AlGaN QWs in the range of 75-80%. Satellite diffraction peaks from MQW samples confirm sharp interfaces between QW and barrier. Figure 7.2 (c) shows the photoluminescence of regrown samples measured using a 193nm ArF excimer laser, where similar emission peaks are found around 250 nm. Sample B and C show shoulder peaks attributed to slightly different Al compositions at the interface of QW and barrier. Figure 7.2(d) shows the band structure of the AlGaN/AlN MQWs structure simulated by Silvaco. Due to the presence of large spontaneous and piezoelectric polarization, a high built-in electric field of 2.4~2.97MV/cm is estimated along the optical axis of the sample [245]. The calculated polarization field is high enough to observe the enhancement of the nonlinear optical signal [72]. In addition, the inset of Fig. 7.2(d) shows the direction of the polarization and the built-in internal field within each layer, with the built-in field in the QW layer pointing downwards to the substrate.

Table 7-1: Specifications of regrown MQWs on the AlN samples

Sample #	Number of MQW layers	* t_{AlN} and t_{MQW}	Wavelength of experiment
A	5	$t_{\text{AlN}} \sim 500\text{nm}$ $t_{\text{MQW}} \sim 60\text{nm}$	Telecom (~1550nm)
B	3	$t_{\text{AlN}} \sim 500\text{nm}$ $t_{\text{MQW}} \sim 36\text{nm}$	Telecom (~1550nm)
C	5	$t_{\text{AlN}} \sim 500\text{nm}$ $t_{\text{MQW}} \sim 60\text{nm}$	~780nm

*Estimated thickness of AlN (t_{AlN}) and MQWs (t_{MQW})

7.4 Design and Fabrication of Microring Resonator Modulator

To measure the enhancement of the Pockels coefficient due to the MQW layer, we design and fabricate the MRMs, measure their resonance shift when applying a voltage, and compare the result with the AlN MRMs of similar dimensions without MQWs. Utilizing a resonator makes the EO measurement easier as the light travels many roundtrips in the ring resonator, and applying a voltage causes a refractive index change due to the Pockels EO effect resulting in a resonance shift.

The relationship between the effective refractive index of ring resonator variation (Δn_{eff}) and linear Pockels effect due to applied bias can be described by [246, 247],

$$\Delta n_{\text{eff}} = \frac{\chi_{\text{eff}}^{(2)} E n_g}{2n_0^2} \quad (\text{Equation 7.1})$$

where $\chi_{\text{eff}}^{(2)}$ represents the modal average effective second-order susceptibility, E is the external electric-field, n_g is the group index, and n_0 is the material refractive index. For each sample,

n_0 is measured with a spectroscopic ellipsometer and extracted by fitting it to a Cauchy dispersion [86].

The effective second-order susceptibility ($\chi_{eff}^{(2)}$), which is the overall effect on the guided mode along with the $\chi^{(2)}$ tensor distributed in the waveguide, can be defined as [246]

$$\chi_{eff}^{(2)} = \frac{\int_{wg} \chi_{mat}^{(2)}(\mathbf{x}_t) n_0^2(\mathbf{x}_t) |e_x(\mathbf{x}_t)|^2 d\mathbf{x}_t}{\int_{\infty} n_0^2(\mathbf{x}_t) |e(\mathbf{x}_t)|^2 d\mathbf{x}_t} \quad (\text{Equation 7.2})$$

where $\mathbf{e}(\mathbf{x}_t)$ is the modal electric field profile and \mathbf{x}_t denotes the transverse coordinates with respect to the light propagation direction and $\chi_{mat}^{(2)}(\mathbf{x}_t)$ represents the second-order susceptibility of materials distributed in the waveguide. Since $\chi_{eff}^{(2)}$ is based on the overlap between the optical guided mode and the second-order susceptibility distributed in the waveguide, high $\chi_{eff}^{(2)}$ is expected by including a high second-order susceptibility layer and increasing its overlap with the optical guided mode. In addition, it allows us to extract $\chi_{mat}^{(2)}$ of each layer based on the measured $\chi_{eff}^{(2)}$ and calculated optical guided mode distribution.

To utilize the highest EO effect, an out-of-plane DC electric field (E_z) is required since r_{13} and r_{33} show the highest EO coefficient for c-axis oriented AlN. Figure 7.3(a) and (b) show the schematics of our demonstrated MRMs, and Fig. 7.3(c) and (d) show the cross-sections of demonstrated ring resonators at telecom and 780nm wavelengths, respectively. The ground metals are placed on the lateral sides of the ring resonator, and the signal metal is placed on top of the ring resonator which is wider than the waveguide width to provide a uniform electric field in the waveguide [64]. The positions of the signal and ground metal are optimized for maximizing the applied electric field in the resonator core and minimizing any optical absorption due to the proximity of these metals to the resonator. The dimension of MRMs made on samples A and B are

the radius of $100\mu\text{m}$, the ring resonator width of $3\mu\text{m}$, the SiO_2 cladding thickness (t_{SiO_2}) of $1.9\mu\text{m}$ and the distance between the ground metal and the ring resonator (g) of $2\mu\text{m}$. For the MRMs made on Sample C, the radius of $30\mu\text{m}$ and the ring resonator width of $0.9\mu\text{m}$, $t_{\text{SiO}_2}=1\mu\text{m}$ and $g=1.3\mu\text{m}$ are used. To increase the coupling efficiency, the pulley coupling scheme is utilized, allowing a wider gap between the two waveguides. Accordingly, the gap between the ring resonator and the bus waveguide, and the width of the bus waveguide are optimized for enhanced waveguide-resonator coupling and their phase-matching condition. Furthermore, for Sample C measured around 780nm wavelength, an 130nm Al_2O_3 is included to additionally increase the coupling efficiency between the ring resonator and the bus waveguide [86].

Based on the MRM designs at telecom (Fig. 7.3(c)) and 780nm (Fig. 7.3(d)) wavelengths, the out-of-plane electric field (E_z) of each layer is simulated by COMSOL. Figure 7.3(e) and (f) show the calculated E_z at different layers following the dashed line, shown in Fig. 7.3 (c) and (d), where the average E_z in the resonator are $E_{\text{avg}}\sim 0.098\text{MV/m}$ (Sample A and B), and $E_{\text{avg}}\sim 0.18\text{MV/m}$ (Sample C) under 1V applied. Calculated E_{avg} can be used to extract the effective second-order susceptibility of the demonstrated MRM along with the measured refractive index variation. Here, we assume that the effective refractive index variation only results from the out-of-plane electric field, where the in-plane EO coefficient (r_{51}) is an order of magnitude lower [64].

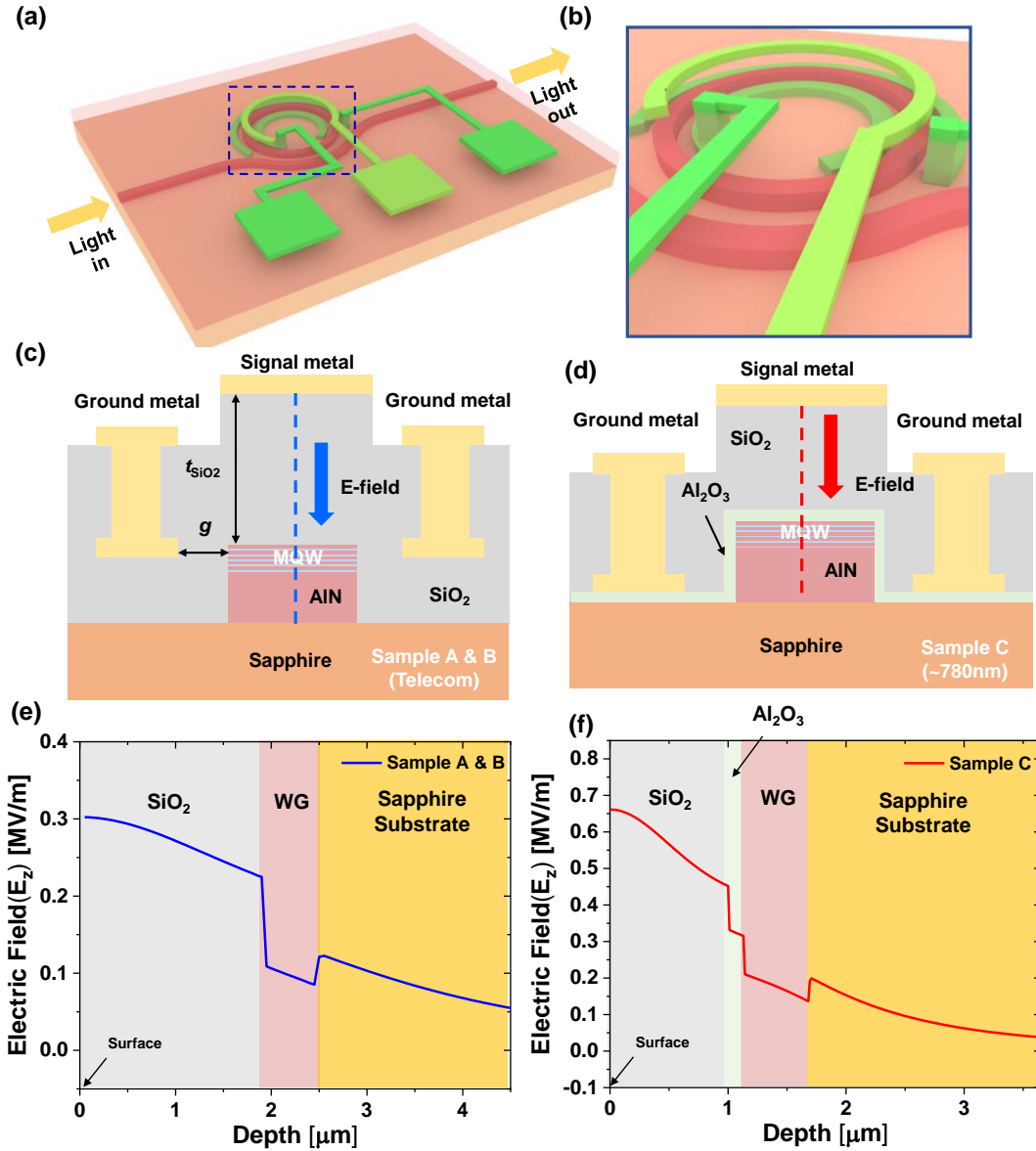


Figure 7.3: (a) Schematic illustration of demonstrated MRMs and (b) magnified ring resonator. (c) and (d) show the cross-sections of MRMs at telecom (Sample A&B) and ~780nm (Sample C) wavelengths, respectively. Thin Al₂O₃ is included for Sample C to increase the coupling efficiency. (e) and (f) show the simulated E_z of each layer, along the dashed line shown in the (c) and (d), respectively.

The fabrication process of the micro-ring resonator can be found in our previous report [86]. In brief, after defining the AIN microring resonator, buffered HF is used to remove the two layers of the hard mask, SiO₂ and Al₂O₃, where Fig. 7.4(a) and the inset show the SEM image of the

defined ring resonator and its sidewall. For Sample A and B, 500nm SiO₂ with PECVD is deposited, whereas, for Sample C, 130nm Al₂O₃ with ALD is deposited. Then Ti(10nm) / Au(140nm) / Al (50nm) layers are directly deposited on the lateral sides of the AlN ring resonator as the ground metals followed by 1.4 μm (Sample A and B) and 1μm PECVD SiO₂ (Sample C) deposition as a cladding layer. The signal metal with Ti(15nm) / Au(85nm) metal stacks are sputtered on top of SiO₂, underneath which the ring resonator is located. After making SiO₂ openings for via contacts, Ti/Al/Au metal stacks are evaporated as a metal via and the GSG contact pads. Finally, dicing and polishing to expose the waveguide facets are performed, with microscope images shown in Fig. 7.4(b).

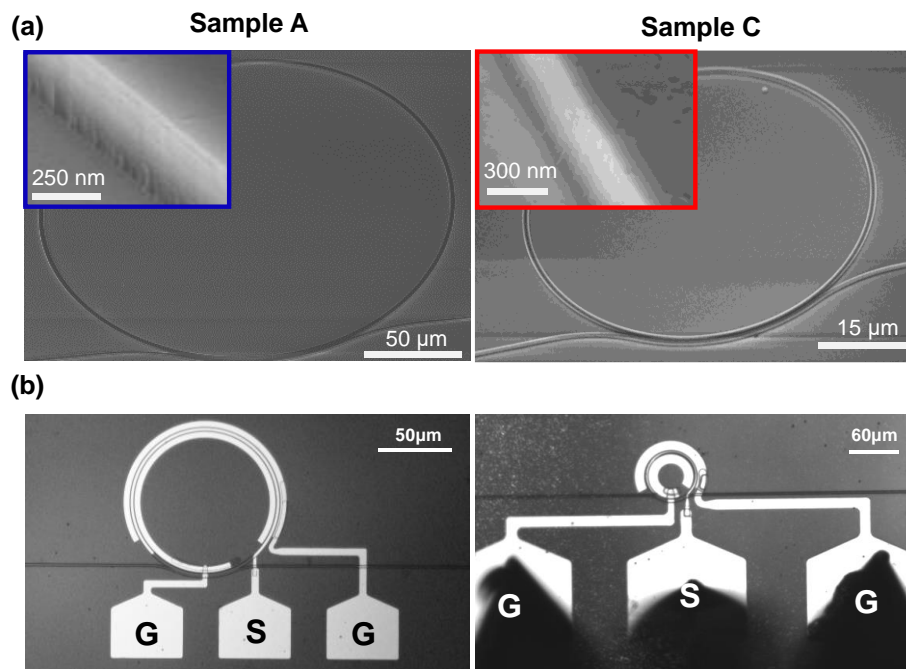


Figure 7.4: SEM images of (a) fabricated microring resonator on Sample A (left) and C (right). Insets show the magnified images of each waveguide sidewall. (b) Optical microscope images of fabricated MRMs on Sample A and C.

7.5 Experimental Result

To characterize the fabricated resonators and their EO effect, laser light from a tunable laser source and an optical tapered lensed fiber is coupled to the chip into a waveguide and travels to reach the waveguide-resonator region. The transmitted light after the waveguide-resonator interaction is collected from the other end of the waveguide. We measure the resonance spectrum by sweeping the laser wavelength and monitoring the transmission. For these experiments, we use the transverse electric (TE) mode of the resonator, which is a more popular polarization for integrated photonics. Figure 7.5(a) shows the TE mode transmission spectrum of Sample A. From this spectrum, we measure a free spectral range (FSR) of 1.8nm, and based on the given relationship, $FSR=\lambda^2/(n_g L)$ with L the round-trip length, we extract the corresponding group index of 2.14. Figure 7.5(b) shows the magnified transmission spectrum around 1553.9nm with an extracted Q_L of 11,460 and an extinction ratio of 25dB, which shows a near critical coupling condition. A positive external bias is applied on the signal metal to observe the EO effect, where E_z and the built-in polarization field are in the same direction. As shown in Fig. 7.5(c), MRM on Sample A (blue) and AlN MRM without MQWs (dashed black) follow a linear relationship between the applied bias and resonance wavelength shift. Based on the following equation, the corresponding effective refractive index variation can be extracted [246].

$$\Delta\lambda_{res} = \lambda_{res} \frac{\Delta n_{eff} \eta}{n_g} \quad (\text{Equation 7.3})$$

where $\Delta\lambda_{res}$ represents resonance wavelength variation, and η is the fraction of the resonator perimeter where the index change occurs. In our design, η is 0.75 for all the samples. Figure 7.5(d) shows the effective refractive index variation as a function of the applied electric field, where $E_z \sim 0.098\text{MV/m}$ at 1V, simulated by COMSOL, is assumed in the resonator.

Based on Eqs. (7.1) and (7.3), MRM on Sample A (5MQWs) shows 2.16 times higher $\chi_{eff}^{(2)}$ compared to bare AlN (w/o MQWs), which can be attributed to the large Pockels coefficient of AlGaIn/AlN MQWs where the huge internal built-in field can perturb the nonlinear optical properties of semiconductor crystal [69, 70]. Similar enhancement is found for MRMs on Sample B. All parameter values for extracting $\chi_{eff}^{(2)}$ of Sample A, B, and bare AlN are listed in Table 7-2.

To extract the second-order susceptibility of the MQW layer, constant second-order susceptibility of AlN and MQWs in the waveguide are assumed, and Eq. (7.2) can be simplified with the mode confinement factor (Γ), a fraction of optical power in each waveguide layer,

$$\chi_{eff}^{(2)} = \chi_{mat1}^{(2)} \Gamma_{mat1} + \chi_{mat2}^{(2)} \Gamma_{mat2} \quad (\text{Equation 7.4})$$

where mat1 is AlN and mat2 is MQW for the regrown samples. The mode confinement factor for each sample is calculated by Lumerical MODE solution, where the inset of Fig. 7.5(c) shows the optical mode profile of Sample A.

First, from the bare AlN MRM resonance shift measurement, $\chi_{AlN}^{(2)}$ ($\sim 15.6 \text{ pm/V}$) is calculated based on the measured $\chi_{eff}^{(2)}$ ($\sim 11.7 \text{ pm/V}$) and the simulated mode confinement factor ($\Gamma_{AlN} \sim 75\%$). With the knowledge of extracted $\chi_{AlN}^{(2)}$ and the simulated mode confinement factor of each layer of the regrown samples, $\chi_{MQW}^{(2)}$ of Sample A and B can be extracted. Calculated $\chi_{MQW}^{(2)}$ of Sample A and B are 308.97 pm/V and 349.44 pm/V , respectively, which are 19.8 and 22.4 times higher than $\chi_{AlN}^{(2)}$. With a relationship given by $r_{ijk} = \chi_{ijk}^{(2)} / n_0^4$ [248, 249], the corresponding Pockels coefficients are calculated as 16.7 pm/V (Sample A), 18.9 pm/V (Sample B) and 0.89 pm/V (bare AlN). The extracted Pockels coefficient of bare AlN is similar to previously reported values, which validates our measurement and analysis [65, 66]. All the parameter values used for extracting $\chi^{(2)}$ of Sample A, B, and bare AlN are listed in Table 7-2.

We also investigate the effect of different dielectric cladding layers, SiO_2 and Al_2O_3 , on the second-order susceptibility of bare AlN MRM at telecom wavelength. For this study, two different AlN MRMs are demonstrated where, for one sample, the SiO_2 cladding layer is deposited directly on the AlN waveguide, shown in Fig. 7.3 (c). In contrast, 130nm Al_2O_3 is included between the AlN waveguide and SiO_2 cladding layer for the other sample. Except for the thin Al_2O_3 cladding layer, other geometries are identical. As shown in Fig. 7.5 (d), a similar magnitude of effective second-order susceptibilities with the different sign of Pockels coefficient is observed. This can be due to the different polarity of fixed charges at the AlN-dielectric cladding interface [250, 251].

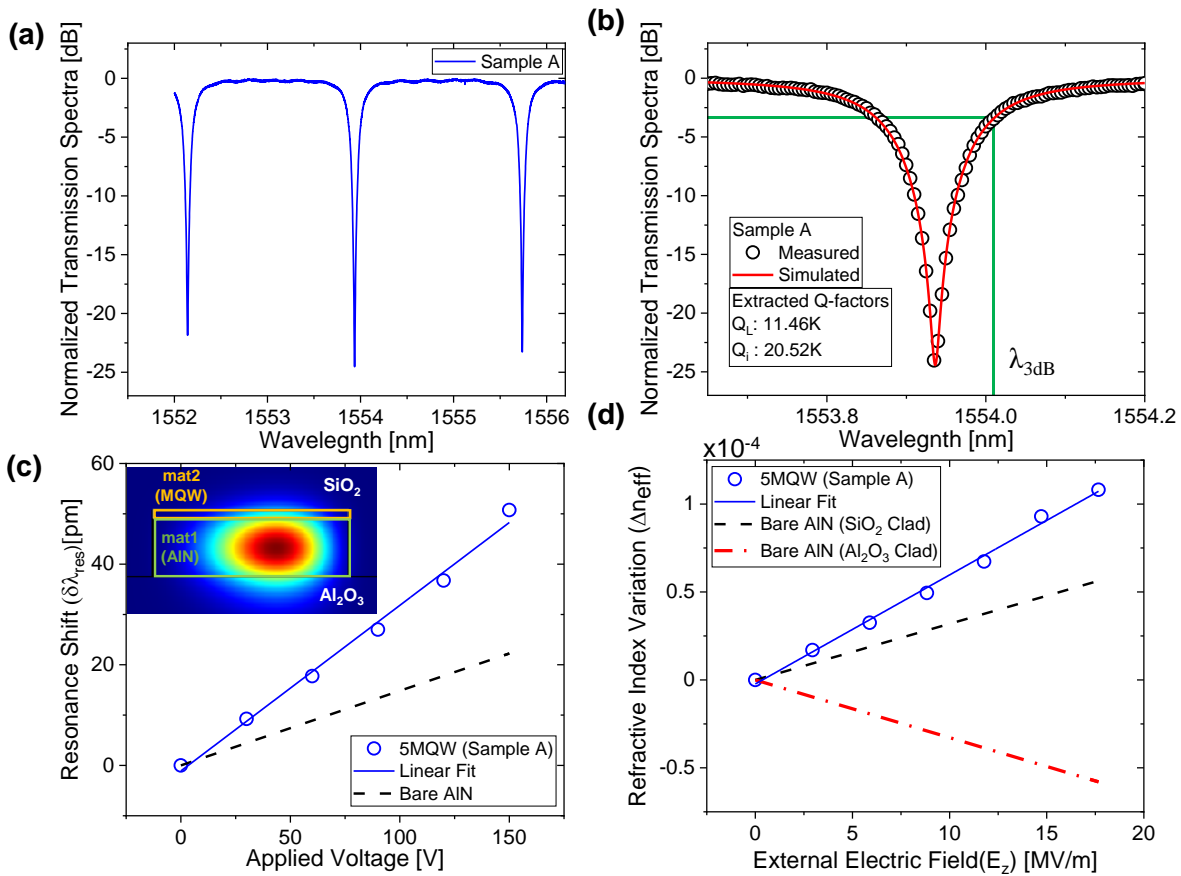


Figure 7.5: (a) Normalized transmission spectrum for a microring resonator made on Sample A (see Table 7-1 for the specifications) and (b) magnified transmission spectrum near 1554nm. λ_{3dB} shows the input wavelength used for frequency response measurement shown in Fig. 7.6. (c) Resonance wavelength shifts as a function of applied voltage of MRMs on Sample A (blue) and bare AlN with SiO_2 cladding (dashed black). The inset shows simulated mode profile of ring resonator on Sample A. (d) Calculated effective refractive index variation of MRMs on Sample A (blue), bare AlN with SiO_2 cladding (dashed black), and bare AlN with Al_2O_3 cladding (dashed red) as a function of applied electric field (E_z). Bare AlN MRM with Al_2O_3 cladding shows a negative relationship between applied electric field and effective index variation.

Table 7-2: Parameter values to extract $\chi^{(2)}$ of Sample A, B, and bare AlN at telecom wavelength

Structure	Sample A	Sample B	AlN (SiO ₂ cladding)
$\chi_{eff}^{(2)}$ (pm/V)	25.36	20.1	11.7
n_g	2.14	2.17	2.17
n_0	2.073	2.073	2.042
Γ_{AIN} (%)	71.13	70.86	75.3
Γ_{MQW} (%)	4.61	2.60	-
$\chi_{AIN}^{(2)}$ (pm/V) / r_{13} (pm/V)	15.6 / 0.89	15.6 / 0.89	15.6 / 0.89
$\chi_{MQW}^{(2)}$ (pm/V) / r_{13} (pm/V)	308.97 / 16.7	349.44 / 18.9	-

Furthermore, the frequency response of the EO resonator modulator is measured. Using a 40GHz network analyzer, we measure the EO modulation amplitude in the frequency domain (S_{21}) of Sample A. The result is shown in Fig. 7.6, where the 3dB cutoff frequency is near 27GHz. This cutoff frequency is limited by the cavity photon lifetime.

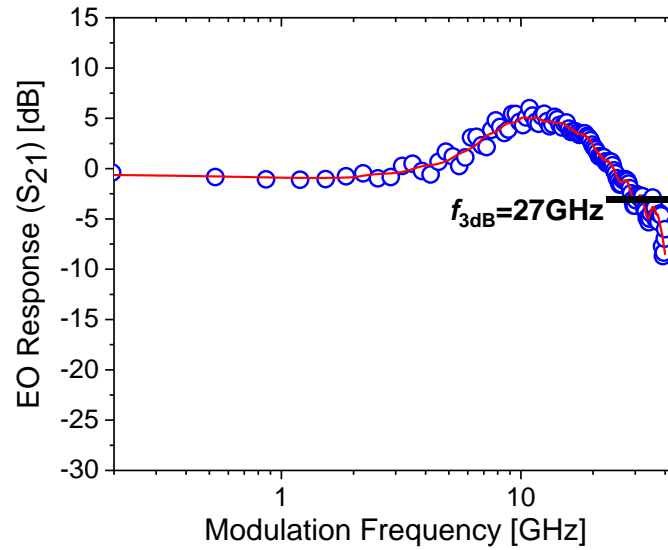


Figure 7.6: Frequency response of EO modulation at telecom wavelength (Sample A) with a 3dB bandwidth of 27 GHz. The laser wavelength is parked at the full-width half-maximum of the resonator.

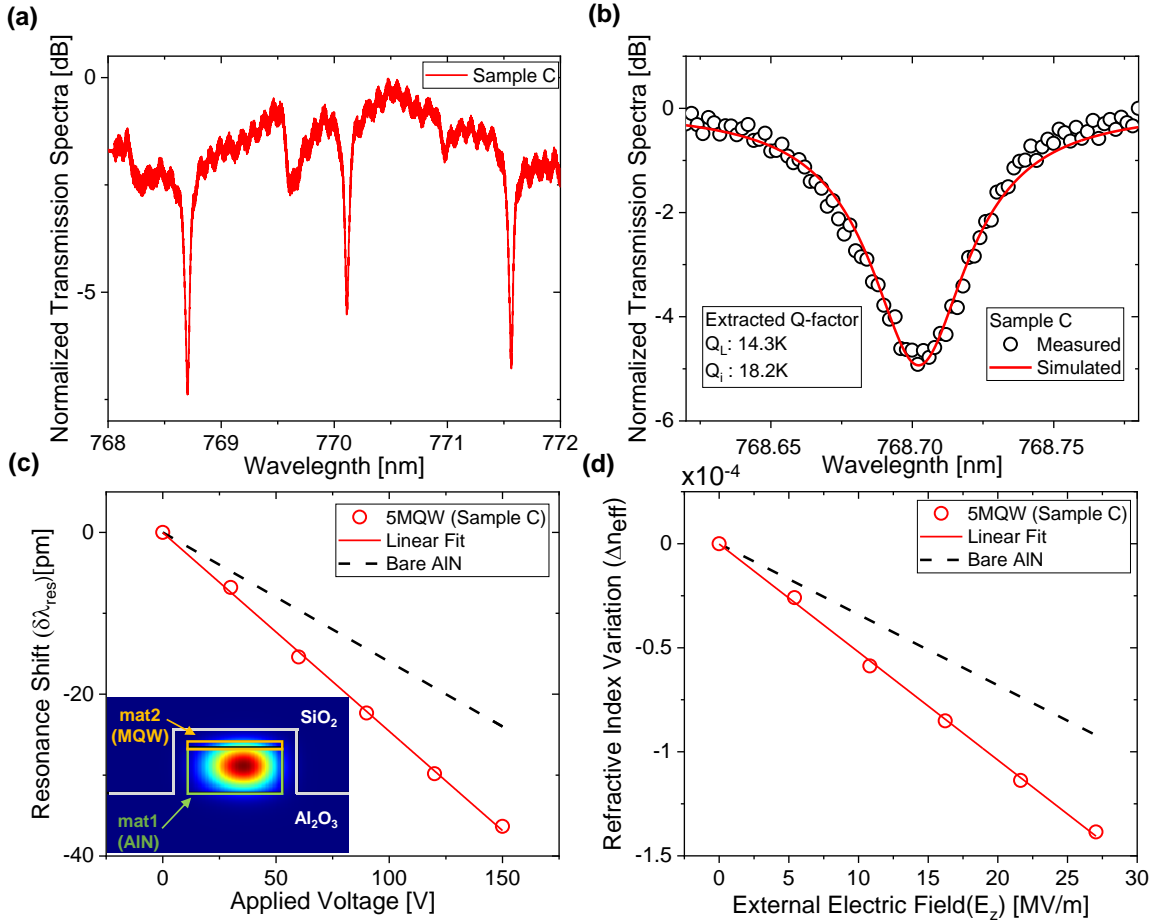


Figure 7.7: (a) Normalized transmission spectrum for a microring resonator made on Sample C (see Table 7-1 for the specifications) and (b) magnified transmission spectrum near 768.7nm. (c) Resonance wavelength shifts as a function of the applied voltage of MRMs on Sample C (red) and bare AlN (black dash). Inset shows the simulated mode profile of ring resonator on Sample C. (d) Calculated effective refractive index variation of MRMs on Sample C (red) and bare AlN (dashed black) as a function of applied electric field (E_z).

Similar investigations are done at 780nm wavelength with Sample C and bare AlN (w/o MQWs) with the similar structure shown in Fig. 7.3(d). Due to the thin Al₂O₃ layer, a negative relationship between the external electric field and the effective refractive index variation is observed. Figure 7.7(a) shows the TE mode transmission spectrum of Sample C. We measure an FSR of 1.43nm from the spectrum and extract the corresponding group index of 2.2. Figure 7.7(b) shows the magnified transmission spectrum around 768.7nm with an extracted Q_L of 14,300. Figure 7.7(c) and (d) show the resonance wavelength shift when applying a voltage and its corresponding effective refractive index variation as a function of the applied electrical field (E_z).

As shown in Fig. 7.3(f), we assume $E_z \sim 0.18 \text{ MV/m}$ at 1V in the waveguide, simulated by COMSOL. From Eq. (7.1) and (7.3), extracted $\chi_{eff}^{(2)}$ of Sample C is -20.4 pm/V , which is 1.56 times higher compared to $\chi_{eff}^{(2)}$ of bare AlN (-13.0 pm/V). Calculated $\chi_{AlN}^{(2)}$ from bare AlN MRM and $\chi_{MQW}^{(2)}$ from MRM of Sample C are -14.3 pm/V and -139.7 pm/V , respectively, where the MQWs shows 9.76 times higher second-order susceptibility than bare AlN. The corresponding Pockels coefficients are -0.79 pm/V (bare AlN) and -7.3 pm/V (Sample C). All the values that are used for extraction are listed in Table 7-3.

Table 7-3: Parameter values to extract $\chi^{(2)}$ of Sample C and bare AlN at 780nm wavelength

Structure	Sample C	AlN
$\chi_{eff}^{(2)} (\text{pm/V})$	-20.4	-13.0
n_g	2.2	2.21
n_0	2.09	2.06
Γ_{AlN}	85.12	91.1
Γ_{MQW}	5.84	-
$\chi_{AlN}^{(2)} (\text{pm/V}) / r_{13} (\text{pm/V})$	-14.3 / -0.79	-14.3 / -0.79
$\chi_{MQW}^{(2)} (\text{pm/V}) / r_{13} (\text{pm/V})$	-139.7 / -7.3	

7.6 Summary

In summary, we investigate the enhancement of the second-order susceptibility and the Pockels EO effect in AlN PICs by employing AlGaN/AlN MQWs on top of the AlN waveguides on a sapphire substrate. To characterize the EO enhancement, we design and fabricate AlN MRMs with and without MQWs on them and measure the resonance shift under the applied voltage for each case. The MRMs with MQWs show the increased resonance shift factors of 2.16 and 1.56 at 1550nm and 780nm wavelengths, respectively, compared to AlN MRMs with similar dimensions but without MQWs. This enhancement can be attributed to the high second-order susceptibility of the MQW layers, which are measured to be 20 (at 1550nm) and 10 (at 780nm) times higher than bare AlN. Our study suggests that a further enhancement in the effective Pockels effect is expected by increasing the overlap between the guided mode of the MRM and MQW layer. We have also investigated the effect of fixed charges at the AlN-dielectric cladding interface on the Pockels coefficient using different cladding layers. The MRMs with Al₂O₃ and SiO₂ cladding layers show a similar magnitude of Pockels effect but a different sign. With existing SiN platforms that can provide ultra-low-loss waveguides but lacks Pockels EO effect, this study offers a new heterogeneous Al(Ga)N PIC platform that can be developed with enhanced EO modulation and low optical loss to operate over a wide wavelength range.

Chapter 8 Summary and Future Work

8.1 Summary

The work presented in the thesis is focused on the demonstration of improved performance Al(Ga)N-based optoelectronic and photonic devices by addressing the challenges of materials and device engineering.

In Chapter 3, we demonstrate backside emitting deep UV LEDs with emission at ~ 265 nm. For high Al composition AlGaIn devices, inefficient hole injection is the main bottleneck to the device performance. With an optimized tunnel junction structure, the hole injection efficiency significantly increases, and improved current-voltage characteristics are measured. Our demonstrated AlGaIn-based deep UV LEDs show EQE of 11% and WPE of 7.6%, respectively.

In Chapter 4, we report on the demonstration of top-emitting AlGaIn tunnel junction deep UV LEDs operating at ~ 267 nm. We show, both theoretically and experimentally, that the light extraction efficiency can be enhanced by nearly a factor of two with the incorporation of AlGaIn nanowire PhC structures. A peak WPE of $\sim 3.5\%$ and EQE of $\sim 5.4\%$ are measured for AlGaIn LEDs directly from the wafer without any packaging. This work demonstrates a viable path for achieving high efficiency deep UV LEDs through the integration of AlGaIn planar and nanoscale structures.

In Chapter 5, we demonstrate ultra-high Q_{int} microring resonators utilizing single-crystal AlN grown on a sapphire substrate with an optimized design and fabrication process. A record high Q_{int} up to 2.8×10^6 at the wavelength of 1550 nm is achieved with a fully etched structure, indicating a low propagation loss of less than 0.13 dB/cm. Such high- Q_{int} AlN resonators on a

sapphire substrate with their wide bandgap and nonlinear optical properties are promising for a wide range of low/high power compact on-chip applications over a broad spectral range.

In Chapter 6, we demonstrate high-Q AlN microring resonators on a sapphire substrate at green (532 nm) and ultraviolet (369.5 nm) wavelengths, which are two important wavelengths for sensing and quantum information processing. The Q-factors of these resonators are characterized using integrated micro-heaters and based on thermo-optic resonance sweeping around those wavelengths for which tunable lasers are typically less available. We measure a record high Q_{int} of 147,000 with a propagation loss of 7.3dB/cm at 532 nm wavelength and a Q_{int} of 25,500 with a propagation loss of 60.4dB/cm at UV 369.5nm wavelength. Due to high thermal conductivity, a large thermal crosstalk and resonance shift are observed on other microring resonators even at a millimeter(s) distance away from a microheater. This study provides further insight into the functionalities and capabilities of this promising integrated photonics platform for the UV and visible range.

In Chapter 7, we demonstrate AlN-based microring resonator modulators at telecom (1550nm) and 780nm wavelengths with enhanced Pockels effect by utilizing AlGaIn/AlN MQWs regrown on AlN waveguide. The modulators with AlGaIn/AlN MQWs show a factor of 2.16 and 1.56 higher resonance wavelength shift than AlN modulators at telecom and 780nm wavelengths, respectively. This enhancement is attributed to the polar nature of III-N materials and the enhanced polarization fields in the MQWs, resulting in higher second-order susceptibility at the MQW layer. Considering the overlap between each layer and the optical guided mode, the second-order susceptibility of AlGaIn/AlN MQWs are ~20 and 10 times higher than that of AlN at telecom and 780nm wavelengths, respectively. This study shows a viable path to realize the enhanced Pockels

effect of AlN-based modulators by engineering the polarization field in MQWs and increasing the overlap between the optical mode and MQWs.

8.2 Overview and Perspective on Al(Ga)N based Optoelectronics and Integrated Photonics

In this thesis, we have discussed and presented the high-performance Al(Ga)N-based deep UV LEDs and microring resonators based on their promising characteristics. However, despite our effort to overcome its limitations discussed in Chapter 1, the EQEs of our demonstrated LEDs and Q_{int} of microring resonators are still much below than that of well-developed materials. Shown in Chapter 3 and 4, a dominant limiting factor of AlGaN deep UV LED is an electron overflow, attributed to the asymmetric carrier transport between electrons and holes and cause the efficiency droop. This effect was also confirmed with Ayush's study [252] by performing detailed electrical and optical analyses of AlGaN UV LEDs emitting at 245nm wavelength. There, to rule out the effect of carrier transport and investigate the radiative recombination from the active region, the sample was optically pumped using a frequency tripled Ti:Sapphire laser. Different from electrically injected conditions, no significant efficiency droop was found confirming the droop is directly from the electron overflow not from the optical phenomenon.

The electron overflow can be somewhat improved by utilizing the electron blocking layer and including an optimized tunnel junction to balance the electron and hole injections. However, the essential improvement of p-type doping on high Al composition AlGaN is necessary to resolve this issue. By solving the asymmetric carrier transport and improving the TM polarized LEE of AlGaN UV LEDs, the EQE comparable to InGaN blue-emitting QW LEDs can be achieved.

For the emerging AlN-based PIC platform, despite several efforts to improve the fabrication process, the reported Q_{int} of AlN MRR is still lower than other materials such as LiNbO₃ and SiN, shown in Fig. 8.1.

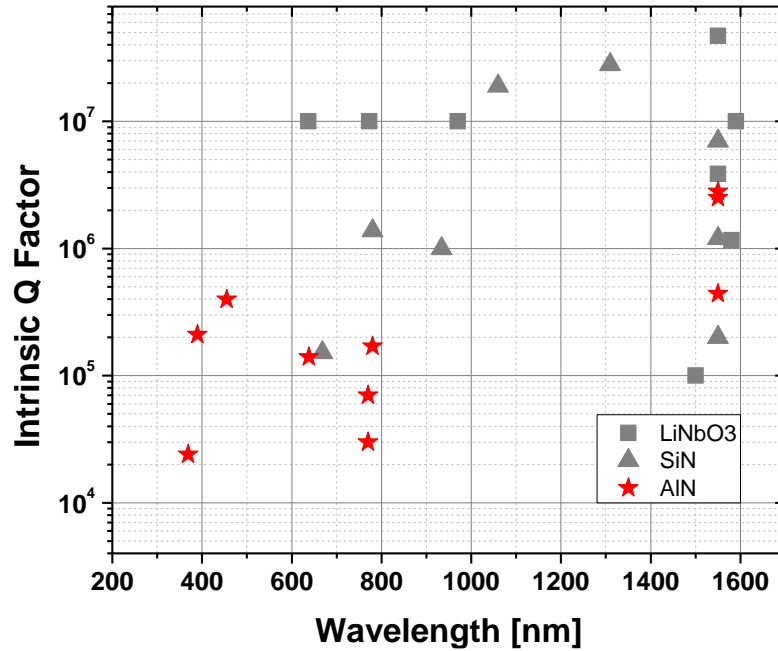


Figure 8.1: Reported Q_{int} of AlN [60, 186, 190, 205], SiN [253-256] and LiNbO₃ [58, 257-262] MRR.

This is due to the premature fabrication process and the low material quality of AlN discussed in Chapter 1. Recently, there was a report with an ultra-high-Q UV microring resonator utilizing a single-crystalline AlN [205]. There, they performed a detailed investigation by characterizing the different widths of MRR at different wavelengths. With the wide width of the microring resonator, sidewall scattering can be relatively addressed and they suggest that their Q_{int} is mainly dominated by Rayleigh scattering ($\propto \lambda^{-4}$). This can be also understood that the material quality of single-crystalline AlN is at the stage to provide low-loss photonic devices, but the current limiting factor is mostly interface scattering due to the fabrication process. Therefore, with a more detailed study to optimize the sidewall roughness of AlN, or by using the wide width of microring resonator, a similar Q_{int} with SiN and LiNbO₃ will be achieved.

We also discussed the enhanced Pockels effect by utilizing AlGaIn/AlN MQW on the AlN platform in Chapter 7. Based on this study, a more enhanced Pockels effect is expected by

engineering the built-in polarization field and increasing the overlap between MQW and its guided optical mode. However, because of increased propagation loss due to the limited material qualities of QW/barrier layers and interface scattering, much degraded Q_{int} was found from the devices as a tradeoff. MRM performance can be represented by its optical modulation amplitude (OMA) and modulation bandwidth (BW) where the figure of merit (FOM) can be defined as [263],

$$FOM = \text{Normalized OMA} \times f(BW), \quad (\text{Equation 8.1})$$

However, it is not only related to effective Pockels coefficient and Q_{int} but other parameters such as coupling efficiency, input detuning, and target data rate also play a critical role. Thus, calculating the FOM of our demonstrated devices does not provide any meaningful insight into MRM design guidelines. However, considering that Q_{int} can be significantly improved by optimizing the growth condition of each layer, I believe our study is valuable that shows the possibility to improve the intrinsic Pockels effect of AlN and makes it a promising platform for UV/Vis PIC platform.

8.3 Future Work

8.3.1 Mode-locked Frequency Comb Based on AlN Microring Resonator

As we discussed in the previous studies, due to noncentrosymmetric crystal structure, the AlN platform shows high $\chi^{(2)}$ and $\chi^{(3)}$ nonlinearities, which is not only suitable for Pockels effect and second harmonic generation but also allows four-wave mixing (FWM), which enables frequency comb generation on chip-scale.

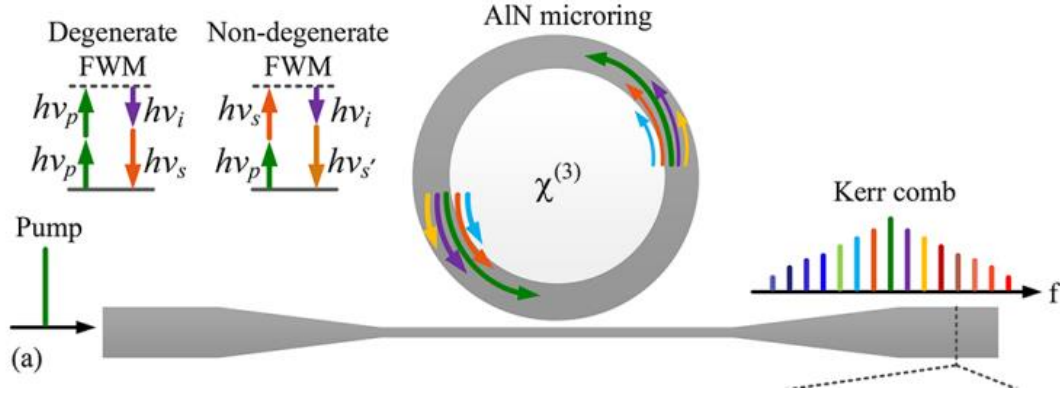


Figure 8.2: Schematic of principle for Kerr comb generation [189].

Figure 8.2 shows the principle of Kerr comb generation based on degenerate FWM and non-degenerate FWM. It is widely known that a high-Q factor with near zero group velocity dispersion is necessary to generate frequency comb using microring resonators [264]. The dispersion of the microring resonator depends on both inherent material dispersion and geometry dispersion, where the latter can be engineered by changing the geometry of the resonator [265]. In addition, high-Q and small mode volume of microring resonator is related to the threshold optical power for comb generation given by [189, 266],

$$P_{th} \sim 1.54 \left(\frac{\pi}{2}\right) \frac{\pi Q_C}{2Q_L} \frac{n^2 V}{n_2 \lambda_p Q_L^2} \quad (\text{Equation 8.2})$$

where V is the effective mode volume, λ_p is the pump wavelength, n_2 represents the nonlinear refractive index.

With the optimized fabrication process of the microring resonator described in Chapter 5, we perform preliminary measurements on frequency comb generation. The commercially available 1 μm thick AlN-on-sapphire substrates from DOWA Holdings Co. Ltd are used to demonstrate microring resonators. To achieve near-zero group velocity dispersion (GVD), which satisfies the phase-matching condition, Lumerical MODE solution is used to optimize the waveguide width where 1.75 μm showed near zero dispersion at 1550nm wavelength.

Figure 8.3 shows the normalized transmission characteristics of demonstrated microring resonator with Q_L of $\sim 300K$.

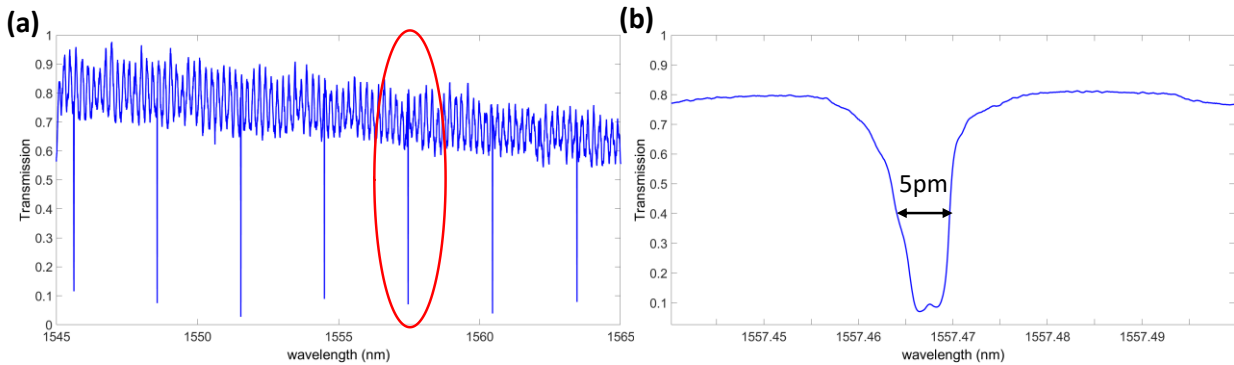


Figure 8.3: (a) Normalized transmission characteristic of demonstrated microring resonator and (b) magnified transmission near 1557.47.

The high-performance tunable laser is used to generate frequency comb, and the EDFA amplifies the input optical power where output is detected by an optical spectrum analyzer (OSA). The input wavelength is slowly detuned from shorter to longer wavelengths and when circulating optical power in the ring resonator becomes higher than the threshold, we start to observe the frequency comb. Subsequently, the input wavelength is tuned toward the resonance wavelength, and more peaks are observed.

Our future study is to demonstrate a mode-locked micro comb, a phase-coherent microcomb that can be utilized for broad applications. However, these states lie on the red-detuned side of the resonance wavelength of the microring resonator, which is very challenging to achieve due to the thermo-refractive effect [267-269]. Several approaches have been reported to achieve a soliton state, such as slow scanning of pump frequency [268, 270, 271], a “power kicking” technique [272, 273], a bidirectional scanning [274], and thermal control [275].

Our approach is to use electro-optical tuning based on Pockels effect under cryogenic conditions. Some reports show that the thermo-refractive coefficient ($\delta n/\delta T$) drops significantly

under cryogenic conditions and makes it easier to achieve soliton states [276]. Currently, microring resonators with electrodes are demonstrated, which can utilize its EO effect. With an optimized fabrication process, demonstrated microring resonator shows Q_L of 600K and will be measured under cryogenic conditions.

8.3.2 Broadband IR to Visible Up-conversion based on III-N Semiconductors

Nonlinear IR up-conversion imaging where an ambient IR light is converted to a shorter visible wavelength is a promising technique for detecting purposes in terms of sensitivity, speed, and noise performance. However, miniaturization of this technology has been challenging due to weak nonlinearity of the materials, bulk size of optical components, and inefficient frequency conversion from broad IR to a single visible wavelength. To overcome these challenges, we plan to use the following techniques,

- 1) III-N quantum dot (QD) structures will be utilized on a transparent sapphire substrate that provides three different energy levels corresponding to pump wavelength, target visible wavelength, and ambient IR. Since it is based on the resonant three-wave mixing, giant nonlinear optical enhancement is expected.

- 2) Metasurface will be utilized to increase the effective optical interaction length over a small mode volume.

Regarding the demonstration of metasurface and III-N QD growth, our group already has significant experience on selective area growth (SAG) of InGaN QW and QD on GaN template, shown in Fig. 8.4, where the same process can be utilized to demonstrate metasurface. Initially, based on the design, 10nm Ti is deposited and patterned with e-beam lithography. Subsequently, Ti is etched with e-beam resist as a mask to open the GaN template where III-N growth will be only formed on the opened area. Currently, Prof. Yu's group at Columbia University is optimizing

the metasurface design, which will be later demonstrated based on our SAG patterning and growth techniques.

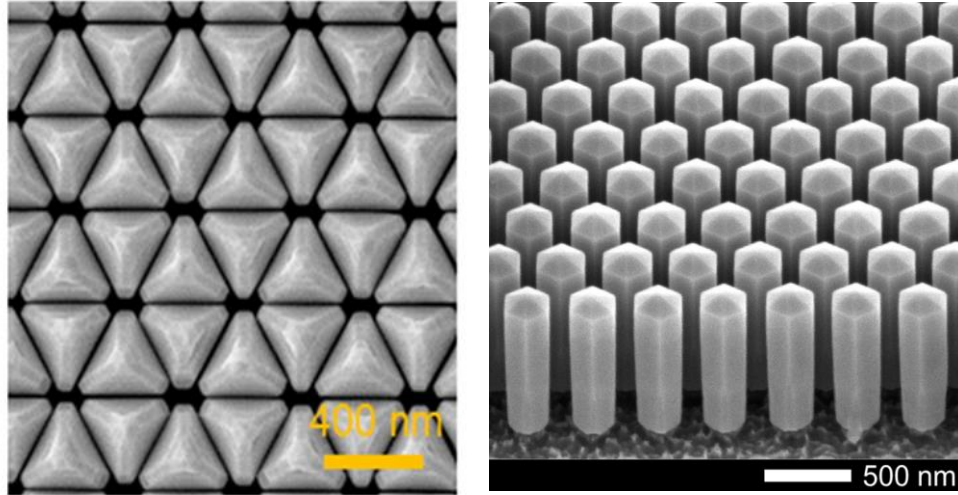


Figure 8.4: SEM image of previously demonstrated selective area growth nanowires with different designs [277].

8.3.3 Investigation of Enhanced Nonlinearity of III-N Semiconductors

In Chapter 7, we already observed the enhanced Pockels coefficient of AlN by utilizing the AlGaN/AlN MQW layer. To expand this work, we are investigating other techniques to enhance III-N semiconductors' nonlinearity, including intersubband transitions in symmetric/asymmetric quantum wells. Another approach includes the ScAlN layer, which provides a much higher piezoelectric and spontaneous polarization field than other III-N semiconductors. Considering the lattice constant and its high spontaneous polarization field, including the ScAlN layer will provide additional freedom for polarization engineering and improve the nonlinearity of III-N semiconductor-based devices.

Appendices

Appendix A Fabrication Procedure for AlGaN Epilayer LEDs

1. Sample Preparation

For MBE growth, we use indium (In) mounting process where the backside of the samples are covered with In after the growth. Therefore, removing In and any other particles is necessary before starting the fabrication process. For backside emitting LEDs, the Mo layer also needs to be removed.

- a. Put the sample in HCl until all the In is etched away.
- b. For backside emitting LEDs, put the sample in Aluminum Etchant Type A until all the Mo is etched away.
- c. Solvent clean using PG remover, acetone, and methanol.
- d. Rinse the sample using DI water.

2. Defining Mesa

The first step is to define the mesa, and the outer part of the mesa is etched down to the n-AlGaN layer, where n-contact will be defined.

- a. Spin coating SPR 220 3.0 at 4000 RPM for 30 seconds. Pre-bake it at 115 °C for 1 min.
- b. Expose using the MJB-3 contact aligner for 8 seconds.
- c. Develop the photoresist using AZ 726 sp 45.

- d. Verify the photolithography process under the optical microscope.
- e. Etch down to the bottom n-AlGaIn contact layer using Oxford ICP RIE (Cl_2 : 20 sccm / Ar: 10 sccm / temp: 50°C / RF power: 40W / ICP: 150W).
- f. Clean the photoresist using PG remover, acetone, methanol, DI water, and dry with an N2 gun.
- g. Verify the etching process under SEM.

3. Deposition of the Insulation Layer

After defining mesa, the bottom and top contact layers must be insulated by 300nm of PECVD SiO_2 . For top-emitting LED, an insulation layer is not included.

- a. Solvent clean the sample using PG remover, acetone, methanol, DI water, and dry with N2 gun.
- b. Load the sample into the Plasmatherm 790 and deposit 300 nm of SiO_2 at 350°C .

4. Etching of Vias and Contact Deposition

To define the metal pad on each contact layer, vias are etched to open each contact layer, and metals are deposited for both top and bottom contact layers.

- a. Solvent clean the sample using PG remover, acetone, methanol, DI water, and dry with N2 gun.
- b. Spin coating SPR 220 3.0 at 4000 RPM for 30 seconds. Pre-bake it at 115°C for 1 min.
- c. Expose using the MJB-3 contact aligner for 8 seconds (Via opening).
- d. Develop the photoresist using AZ 726 sp 45.

- e. Verify the photolithography process under the optical microscope.
- f. Etch SiO₂ using LAM 9400 recipe (Pressure: 10mTorr / temp: 50°C / TCP Power: 500W / Bias Power: 100W / Ar: 45 sccm / C₄F₈: 45sccm / He: 45 sccm / SF₆ 7.2 sccm).
- g. Put it in buffer HF for 5sec.
- h. Clean the photoresist using PG remover, acetone, methanol, DI water, and dry with an N₂ gun.
- i. Spin coating SPR 220 3.0 at 4000 RPM for 30 seconds. Pre-bake it at 115 °C for 1min.
- j. Expose using the MJB-3 contact aligner for 8 seconds (Bottom metal contact).
- k. Develop the photoresist using AZ 726 sp 45.
- l. Verify the photolithography process under the optical microscope.
- m. For the bottom n-contact, Ti (40 nm)/Al (120 nm)/Ni (40 nm)/Au (100 nm) is deposited using e-beam evaporation.
- n. Perform lift-off using remover PG at 80°C.
- o. The metal contacts are then annealed at 700 °C in N₂ for 30 seconds.
- p. Steps h-l are then repeated for the top-contact.
- q. For the top-contact, if the device has a p-type contact layer as a topmost layer, Ni (20 nm)/Au (100 nm) is used, and if the device is a tunnel junction with an n-type top contact layer as a topmost layer, Ti (40 nm)/Al (120 nm)/Ni (40 nm)/Au (100 nm) is deposited.
- r. Perform lift-off using remover PG at 80°C.
- s. For Ni/Au metal stack, 60 seconds annealing at 500 °C in air conditions, and for Ti/Al/Ni/Au metal stack, 30 seconds annealing at 700 °C in N₂ conditions are used.
- t. The wafer is diced into dies for measurement.

Appendix B Fabrication Procedure for AlN Microring Resonator and Modulator

1. Sample Preparation

It is very important to have a cleaned sample before SiO₂ deposition since any particle can act as a micromask for AlN etching which is critical to demonstrate a high-Q microring resonator.

- a. Rinse the sample using DI water, spin coating the 2-inch AlN wafer with SPR220 using 4K RPM and prebake at 115 °C for 1 min and dice the 2-inch wafer into 1.1 cm x 1.1 cm pieces (1 cm x 1 cm pieces for MBE regrowth).
- b. Put the samples in PG remover at 85 °C for 10 mins and change to another beaker with PG remover for another 10 mins.
- c. Put the samples in IPA at 72 °C for 3 mins.
- d. Rinse the samples with DI water and blow dry.
- e. Put the samples in Aluminum Etch for 8 mins to remove Mo on the backside of the samples and rinse with DI water.
- f. Put the samples in HCl for 10 mins to remove Ga droplet if any, rinse with DI water and blow dry.
- g. Check under a microscope and make sure no particles on the surface after cleaning.
- h. If there are still some particles after cleaning mentioned above, try RCA clean as follows in steps i and j.
- i. Put the samples in NH₄OH:H₂O₂:H₂O=1:1:5 for 5 mins, rinse with DI water and blow dry.

- j. Put the samples in HCl:H₂O₂:H₂O=1:1:6 for 5 mins, rinse with DI water, and blow dry.
- k. Put the samples in Nanostrip for 10 mins, rinse with DI water and blow dry.
- l. Put the samples in Acetone at 72 °C for 5 mins.
- m. Put the samples in Methanol at 72 °C for 3 mins.
- n. Rinse the samples with DI water and blow dry.
- o. Load the samples into GSI PECVD to deposit 500 nm SiO₂. Use Si bare dummy wafers to calibrate the thickness of SiO₂.

2. Defining Al₂O₃ Hard Masks

The first step in the device fabrication is to define the Al₂O₃ mask with electron beam lithography, which shows 20:1 etching selectivity with SiO₂. After defining the Al₂O₃ mask, the SiO₂ mask will be defined based on Al₂O₃.

- a. Put the samples in Acetone and Methanol at 72 °C for 3 mins, respectively. Rinse with DI water and blow dry. Inspect and make sure the sample surface is clean. Load the samples in YES plasma (O₂: 80 sccm / Power: 300 W / Temperature 60 °C) for 2mins. Leave the samples at 180 °C for 2 mins for dehydration bake and let the samples cooldown.
- b. Take the PMMA 495 A2, PMMA 950 A2, and Discharge H₂Ox2 bottle from the private cabinet.
- c. Spin coating PMMA 495 A2 using the recipe 1600 RPM. Bake at 180 °C for 3 mins and cool down. Spin coating PMMA 950 A2 using the recipe 4K RPM. Bake at 180 °C for 3 mins and cool down.

- d. Spin coating Discharge H₂O_x2 using recipe 1500 RPM and put some Ni beads on the top edge of the samples.
- e. Start EBL writing based on the design layout.
- f. Put the sample in the mixture MIBK:IPA=1:3 for 90 seconds without stirring.
- g. Put the sample in IPA, gently stir for the 30s in IPA, and quickly dry with an N₂ gun. Check the patterns and alignment under a microscope.
- h. Use single side tape to cover the four sides of the sample and load it into the AE evaporator.
- i. Use 2 Å/s deposition rate to deposit 30 nm Al₂O₃ and do lift-off process immediately.
- j. Put the sample in PG remover for 20 mins at 85 °C. Change the beaker and keep it in PG remover for 20mins at 85 °C.
- k. Put the sample into acetone at 72 °C for another 30 mins. Using a pipette to agitate the lift-off process, check the patterns under a microscope and ensure no residue is left after lift-off.
- l. Put it in methanol and rinse the sample with DI water and blow dry with an N₂ gun.
- m. Check the Al₂O₃ mask or PMMA leftovers on the samples under SEM.

3. Defining SiO₂ mask and AlN Waveguide

The next step is to define the SiO₂ mask and etch AlN, where SiO₂ showed 3:1 etching selectivity. For the AlN etching, an optimized ICP-RIE recipe is required to have a smooth and vertical sidewall.

- a. Put the samples in Acetone at 72 °C for 5 mins and put the samples in Methanol at 72 °C for 3 mins. Rinse the samples with DI water and blow dry.

- b. Etch SiO₂ using Al₂O₃ mask, with ICP-RIE (Pressure: 10mTorr / temp: 50°C / TCP Power: 500W / Bias Power: 100W / Ar: 45 sccm / C₄F₈: 45sccm / He: 45 sccm / SF₆ 7.2 sccm).
- c. Put the samples in Nanostrip for 10 mins to remove any etching residuals, rinse it with DI water and blow dry.
- d. Put the samples in Acetone at 72°C for 5 mins. Put the samples in Methanol at 72 °C for 3 mins. Rinse the samples with DI water and blow dry.
- e. Check the SiO₂ masks sidewalls and particle density under SEM.
- f. Dry etching AlN using Oxford ICP-RIE (Cl₂: 20 sccm / Ar: 10 sccm / temp: 50°C / RF power: 40W / ICP: 150W).
- g. Put the samples in BHF for 2min ~ 2 mins 10 seconds to remove the SiO₂ mask (Check under SEM to make sure the SiO₂ mask is all etched away).
- h. Check the sidewall profile and particle density under SEM.

4. For High-Q Resonator or Frequency Comb

After defining the AlN waveguide (Step 3), for passive devices such as high-Q resonator (Ch.5) or frequency comb (Ch. 8), which doesn't need a metal pad, cladding layer can be directly deposited.

- a. Put the samples in Acetone at 72 °C for 5 mins and put the samples in Methanol at 72 °C for 3 mins. Rinse the samples with DI water and blow dry.
- b. Load the samples into GSI PECVD to deposit 3μm SiO₂. Use Si bare dummy wafers to calibrate the thickness of SiO₂.

- c. Spin coating the samples with SPR220 or S1813 at 4K rpm and prebake at 115 °C for 1 min.
Dice each sample into two chips and perform the polishing for edge coupling.

5. For Green and UV Wavelength Device with Micro-heater

After defining the AlN waveguide (Step 3), NiCr needs to be deposited on top of the cladding layer for devices with microheater (Ch. 6). In addition, for microring resonators operating at visible and UV wavelengths, a thin Al₂O₃ layer is deposited before the SiO₂ layer to increase the coupling efficiency between resonator and bus waveguide.

- a. Put the samples in Acetone at 72 °C for 5 mins and put the samples in Methanol at 72 °C for 3 mins. Rinse the samples with DI water and blow dry.
- b. Load the samples into Veeco Fiji ALD and deposit 130 nm Al₂O₃ at 250 °C (Al₂O₃ Thermal).
- c. Load the samples into GSI PECVD to deposit 1 μm SiO₂. Use Si bare dummy wafers to calibrate the thickness of SiO₂.
- d. Put the samples in Acetone and Methanol at 72 °C for 3 mins, respectively. Rinse with DI water and blow dry. Inspect and make sure the sample surface is clean. Load the samples in YES plasma (O₂: 80 sccm / Power: 300 W / Temperature 60 °C) for 2mins. Leave the samples at 180 °C for 2 mins for dehydration bake and let the samples cooldown.
- e. Spin coating PMMA 950 A6 using the recipe 4K RPM. Bake at 180 °C for 3 mins and cool down.
- f. Spin coating Discharge H₂O₂ (No baking!) using recipe 1500 RPM.
- g. Start EBL writing based on the design layout.
- h. Put the sample in the mixture MIBK:IPA=1:3 for 90 seconds without stirring.

- i. Put the sample in IPA, gently stir for the 30s in IPA, and dry with an N₂ gun. Check the patterns and alignment under a microscope.
- j. Load the samples into Cooke Evaporator to deposit 150 nm NiCr using 5 A/s (Microheater).
- k. Put the samples in PG remover for 20 mins at 85 °C with 3 different beakers. Put the samples into acetone at 72 °C for another 30 mins. Using a pipette to agitate the lift-off process, check the patterns under a microscope and ensure no residues are left after lift-off. Rinse the sample with Methanol, DI water and blow dry with an N₂ gun.
- l. Check under microscope and SEM and make sure the lift-off process and alignment are good for the heaters on top of the resonators.
- m. Spin coating the samples with Lor 10b using recipe 3K RPM and bake at 150 °C for 3 mins. Spin coating with SPR 220 3.0 using 4K RPM and bake at 115 °C for 1 min.
- n. Expose the samples using MJB3 for 8.5 s and develop using SP30.
- o. Load the samples into an AE evaporator and deposit 10 nm Ti/ 900 nm Al /90 nm Au (Metal pad).
- p. Put the samples in PG remover for 20 mins at 85 °C with 3 different beakers. Put the samples into acetone at 72 °C for another 30 mins. Using a pipette to agitate the lift-off process, check the patterns under a microscope and ensure no residues are left after lift-off. Rinse the sample with Methanol, DI water, and blow dry with an N₂ gun.
- q. Spin coating the samples with SPR220 or S1813 at 4K rpm and prebake at 115 °C for 1 min. Dice each sample into two chips and polish each side of the chip.

6. For Enhanced Pockels or Frequency Comb with Electrode Devices

After defining the AlN waveguide (Step 3), for devices with ground-signal-ground (GSG) metal pad such as enhanced Pockels effect devices (Ch. 7) or frequency comb with the electrodes (Ch.8), additional lithography and metal depositions are needed before and after SiO₂ cladding layer.

- a. Put the samples in Acetone and Methanol at 72 °C for 3 mins, respectively. Rinse with DI water and blow dry. Inspect and make sure the sample surface is clean. Load the samples in YES plasma (O₂: 80 sccm / Power: 300 W / Temperature 60°C) for 2mins. Leave the samples at 180 °C for 2 mins for dehydration bake and let the samples cooldown on the heat sink.
- b. Spin coating PMMA 950 A6 using the recipe 4K RPM. Bake at 180 °C for 3 mins and cool down.
- c. Spin coating Discharge H₂Ox₂ using recipe 1500 RPM.
- d. Start EBL writing based on the design layout.
- e. Put the sample in the mixture MIBK:IPA=1:3 for 90 seconds without stirring.
- f. Put the sample in IPA and gently stir for the 30s in IPA and dry with an N₂ gun. Check the patterns and alignment under a microscope.
- g. Load the samples into an AE evaporator to deposit 10 nm Ti/40 nm Au/50 nm Al (Ground metal).
- h. Put the samples in PG remover for 20 mins at 85 °C with 3 different beakers. Put the samples into acetone at 72 °C for another 30 mins. Using a pipette to agitate the lift-off process, check the patterns under a microscope and ensure no residues are left after lift-off. Rinse the sample with Methanol, DI water, and blow dry with an N₂ gun.

- i. Check under microscope and SEM and ensure the lift-off and alignment are good.
- j. Load the samples into GSI PECVD to deposit $1\mu\text{m}$ SiO_2 . Use Si bare dummy wafers to calibrate the thickness of SiO_2 .
- k. Spin coating with SPR 220 3.0 using 4K RPM and prebake at $115\text{ }^\circ\text{C}$ for 1 min.
- l. Expose the samples using MJB3 for 8 s and develop using SP30 (Via opening).
- m. Load the samples into LAM 9400 and etch SiO_2 for $1\mu\text{m}$ via opening (Pressure: 10mTorr / temp: $50\text{ }^\circ\text{C}$ / TCP Power: 500W / Bias Power: 100W / Ar: 45 sccm / C_4F_8 : 45sccm / He: 45 sccm / SF_6 7.2 sccm).
- n. Dip the samples into BHF for 5~10s and check the SiO_2 window opening under SEM. Using EDS to make sure SiO_2 is all etched away.
- o. Put the samples in Acetone and Methanol at $72\text{ }^\circ\text{C}$ for 3 mins, respectively. Rinse with DI water and blow dry. Inspect and make sure the sample surface is clean. Load the samples in YES plasma (O_2 : 80 sccm / Power: 300 W / $60\text{ }^\circ\text{C}$) for 2mins. Leave the samples at $180\text{ }^\circ\text{C}$ for 2 mins for dehydration bake and let the samples cooldown on the heat sink.
- p. Spin coating PMMA 950 A6 using the recipe 4K RPM. Bake at $180\text{ }^\circ\text{C}$ for 3 mins and cool down.
- q. Spin coating Discharge H_2O_x2 using recipe 1500 RPM (No baking!).
- r. Start EBL writing based on the design layout.
- s. Put the sample in the mixture MIBK:IPA=1:3 for 90 seconds without stirring.
- t. Put the sample in IPA and gently stir for the 30s in IPA and dry with an N_2 gun. Check the patterns and alignment under a microscope.
- u. Load the samples into Lab18_2 to deposit 10 nm Ti/60 nm Au/30 nm Al using sputtering (Signal metal).

- v. Put the samples in PG remover for 20 mins at 85 °C with 3 different beakers. Put the samples into acetone at 72 °C for another 30 mins. Using a pipette to agitate the lift-off process, check the patterns under a microscope and ensure no residues are left after lift-off. Rinse the sample with Methanol, DI water, and blow dry with an N2 gun.
- w. Check under microscope and SEM and make sure the lift and alignment are good.
- x. Spin coating the samples with Lor 10b using recipe 3K RPM and bake at 150 °C for 3 mins. Spin coating with SPR 220 3.0 using 4K RPM and bake at 115 °C for 1 min.
- y. Expose the samples using MJB3 for 8.5 s and develop using SP30.
- z. Load the samples into an AE evaporator and deposit 10 nm Ti/900 nm Al/90 nm Au (Metal pad).
- aa. Put the samples in PG remover for 20 mins at 85 °C with 3 different beakers. Put the samples into acetone at 72 °C for another 30 mins. Using a pipette to agitate the lift-off process, check the patterns under a microscope and ensure no residues are left after lift-off. Rinse the sample with Methanol, DI water, and blow dry with an N2 gun.
- bb. Spin coating the samples with SPR220 or S1813 at 4K rpm and prebake at 115 °C for 1 min. Dice each sample into two chips and polish each side of the chip.

Bibliography

1. Schubert, E.F., *Light-emitting diodes Cambridge University Press*. New York, 2006: p. 35-40.
2. Taniyasu, Y. and M. Kasu, *Improved emission efficiency of 210-nm deep-ultraviolet aluminum nitride light-emitting diode*. NTT Tech. Rev, 2010. **8**(1).
3. Vurgaftman, I. and J.n. Meyer, *Band parameters for nitrogen-containing semiconductors*. Journal of Applied Physics, 2003. **94**(6): p. 3675-3696.
4. Bernardini, F., V. Fiorentini, and D. Vanderbilt, *Spontaneous polarization and piezoelectric constants of III-V nitrides*. Physical Review B, 1997. **56**(16): p. R10024.
5. Arnaudov, B., et al., *Energy position of near-band-edge emission spectra of InN epitaxial layers with different doping levels*. Physical Review B, 2004. **69**(11): p. 115216.
6. Ryou, J.-H., et al., *Control of quantum-confined stark effect in InGaN-based quantum wells*. IEEE Journal of Selected Topics in Quantum Electronics, 2009. **15**(4): p. 1080-1091.
7. Ambacher, O., et al., *Two-dimensional electron gases induced by spontaneous and piezoelectric polarization charges in N- and Ga-face AlGaIn/GaN heterostructures*. Journal of applied physics, 1999. **85**(6): p. 3222-3233.
8. Park, S.-H. and S.-L. Chuang, *Spontaneous polarization effects in wurtzite GaN/AlGaIn quantum wells and comparison with experiment*. Applied Physics Letters, 2000. **76**(15): p. 1981-1983.
9. Takeuchi, T., H. Amano, and I. Akasaki, *Theoretical study of orientation dependence of piezoelectric effects in wurtzite strained GaInN/GaN heterostructures and quantum wells*. Japanese Journal of Applied Physics, 2000. **39**(2R): p. 413.
10. Schwarz, U.T., et al., *Interplay of built-in potential and piezoelectric field on carrier recombination in green light emitting InGaIn quantum wells*. Applied Physics Letters, 2007. **91**(12): p. 123503.
11. Grundmann, M.J. and U.K. Mishra, *Multi-color light emitting diode using polarization-induced tunnel junctions*. physica status solidi (c), 2007. **4**(7): p. 2830-2833.
12. Krishnamoorthy, S., et al., *Polarization-engineered GaN/InGaIn/GaN tunnel diodes*. Applied Physics Letters, 2010. **97**(20): p. 203502.
13. Simon, J., et al., *Polarization-induced Zener tunnel junctions in wide-band-gap heterostructures*. Physical Review Letters, 2009. **103**(2): p. 026801.
14. Schubert, M.F., *Interband tunnel junctions for wurtzite III-nitride semiconductors based on heterointerface polarization charges*. Physical Review B, 2010. **81**(3): p. 035303.
15. *Light Emitting Diode (LED)*. Available from: <https://www.physics-and-radio-electronics.com/electronic-devices-and-circuits/semiconductor-diodes/lightemittingdiodeledconstructionworking.html>.
16. Amano, H., et al., *Metalorganic vapor phase epitaxial growth of a high quality GaN film using an AlN buffer layer*. Applied Physics Letters, 1986. **48**(5): p. 353-355.

17. Amano, H., et al., *P-type conduction in Mg-doped GaN treated with low-energy electron beam irradiation (LEEBI)*. Japanese Journal of Applied Physics, 1989. **28**(12A): p. L2112.
18. Nakamura, S., et al., *Thermal annealing effects on p-type Mg-doped GaN films*. Japanese Journal of Applied Physics, 1992. **31**(2B): p. L139.
19. Hirayama, H., et al., *Recent progress and future prospects of AlGaIn-based high-efficiency deep-ultraviolet light-emitting diodes*. Japanese Journal of Applied Physics, 2014. **53**(10): p. 100209.
20. Khan, A., K. Balakrishnan, and T. Katona, *Ultraviolet light-emitting diodes based on group three nitrides*. Nature photonics, 2008. **2**(2): p. 77.
21. Nagasawa, Y. and A. Hirano, *A review of AlGaIn-based deep-ultraviolet light-emitting diodes on sapphire*. Applied Sciences, 2018. **8**(8): p. 1264.
22. Asif Khan, M., *AlGaIn multiple quantum well based deep UV LEDs and their applications*. physica status solidi (a), 2006. **203**(7): p. 1764-1770.
23. Kneissl, M., et al., *The emergence and prospects of deep-ultraviolet light-emitting diode technologies*. nature photonics, 2019. **13**(4): p. 233-244.
24. Li, D., et al., *AlGaIn photonics: recent advances in materials and ultraviolet devices*. Advances in Optics and Photonics, 2018. **10**(1): p. 43-110.
25. Ban, K., et al., *Internal quantum efficiency of whole-composition-range AlGaIn multi-quantum wells*. Applied physics express, 2011. **4**(5): p. 052101.
26. Yan, J., et al., *AlGaIn-based deep-ultraviolet light-emitting diodes grown on high-quality AlN template using MOVPE*. Journal of Crystal Growth, 2015. **414**: p. 254-257.
27. Kueller, V., et al., *Growth of AlGaIn and AlN on patterned AlN/sapphire templates*. Journal of Crystal Growth, 2011. **315**(1): p. 200-203.
28. Laleyan, D.A., et al., *Strain-free ultrathin AlN epilayers grown directly on sapphire by high-temperature molecular beam epitaxy*. Applied Physics Letters, 2020. **116**(15): p. 152102.
29. Taniyasu, Y., M. Kasu, and N. Kobayashi, *Intentional control of n-type conduction for Si-doped AlN and Al_xGa_{1-x}N (0.42 ≤ x < 1)*. Applied physics letters, 2002. **81**(7): p. 1255-1257.
30. Li, S., et al., *Polarization induced hole doping in graded Al_xGa_{1-x}N (x = 0.7 ~ 1) layer grown by molecular beam epitaxy*. Applied Physics Letters, 2013. **102**(6): p. 062108.
31. Mattila, T. and R.M. Nieminen, *Point-defect complexes and broadband luminescence in GaN and AlN*. Physical Review B, 1997. **55**(15): p. 9571.
32. Zheng, T., et al., *High Mg effective incorporation in Al-rich Al_xGa_{1-x}N by periodic repetition of ultimate V/III ratio conditions*. Nanoscale research letters, 2014. **9**(1): p. 1-7.
33. Zhao, C.-Z., et al., *The activation energy for Mg acceptor in Al_xGa_{1-x}N alloys in the whole composition range*. Superlattices and Microstructures, 2017. **109**: p. 758-762.
34. Kinoshita, T., et al., *High p-type conduction in high-Al content Mg-doped AlGaIn*. Applied Physics Letters, 2013. **102**(1): p. 012105.
35. Nakarmi, M., et al., *Enhanced p-type conduction in GaN and AlGaIn by Mg-δ-doping*. Applied physics letters, 2003. **82**(18): p. 3041-3043.
36. Taniyasu, Y., M. Kasu, and T. Makimoto, *An aluminium nitride light-emitting diode with a wavelength of 210 nanometres*. nature, 2006. **441**(7091): p. 325-328.

37. Luo, W., et al., *Enhanced p-type conduction in AlGa_N grown by metal-source flow-rate modulation epitaxy*. Applied Physics Letters, 2018. **113**(7): p. 072107.
38. Li, S., et al., *Polarization induced pn-junction without dopant in graded AlGa_N coherently strained on Ga_N*. Applied Physics Letters, 2012. **101**(12): p. 122103.
39. Simon, J., et al., *Polarization-induced hole doping in wide-band-gap uniaxial semiconductor heterostructures*. Science, 2010. **327**(5961): p. 60-64.
40. Pandey, A., et al., *Enhanced doping efficiency of ultrawide band gap semiconductors by metal-semiconductor junction assisted epitaxy*. Physical Review Materials, 2019. **3**(5): p. 053401.
41. Dai, Q., et al., *Carrier recombination mechanisms and efficiency droop in GaInN/GaN light-emitting diodes*. Applied Physics Letters, 2010. **97**(13): p. 133507.
42. So, B., et al., *Efficiency improvement of deep-ultraviolet light emitting diodes with gradient electron blocking layers*. physica status solidi (a), 2018. **215**(10): p. 1700677.
43. Li, L., et al., *On the hole injection for III-nitride based deep ultraviolet light-emitting diodes*. Materials, 2017. **10**(10): p. 1221.
44. Zhang, Z.-H., et al., *Hole transport manipulation to improve the hole injection for deep ultraviolet light-emitting diodes*. Acs Photonics, 2017. **4**(7): p. 1846-1850.
45. Pandey, A., et al., *Effect of electron blocking layer on the efficiency of AlGa_N mid-ultraviolet light emitting diodes*. Optics express, 2019. **27**(12): p. A738-A745.
46. Taniyasu, Y., M. Kasu, and T. Makimoto, *Radiation and polarization properties of free-exciton emission from AlN (0001) surface*. Applied physics letters, 2007. **90**(26): p. 261911.
47. Lee, Y.-J., et al., *Improvement in light-output efficiency of near-ultraviolet InGa_N-Ga_N LEDs fabricated on stripe patterned sapphire substrates*. Materials Science and Engineering: B, 2005. **122**(3): p. 184-187.
48. Lee, C., et al., *Output power enhancement of vertical-injection ultraviolet light-emitting diodes by Ga_N-free and surface roughness structures*. Electrochemical and Solid State Letters, 2008. **12**(2): p. H44.
49. Guo, W., et al., *KOH based selective wet chemical etching of AlN, Al_xGa_{1-x}N, and Ga_N crystals: A way towards substrate removal in deep ultraviolet-light emitting diode*. Applied Physics Letters, 2015. **106**(8): p. 082110.
50. Li, Z., et al., *High-power AlGa_N-based near-ultraviolet light-emitting diodes grown on Si (111)*. Applied Physics Express, 2017. **10**(7): p. 072101.
51. Takano, T., et al., *Deep-ultraviolet light-emitting diodes with external quantum efficiency higher than 20% at 275 nm achieved by improving light-extraction efficiency*. Applied Physics Express, 2017. **10**(3): p. 031002.
52. Shen, C., et al. *Laser-based visible light communications and underwater wireless optical communications: a device perspective*. in *Novel In-Plane Semiconductor Lasers XVIII*. 2019. International Society for Optics and Photonics.
53. Hoffman, L., et al., *Low loss CMOS-compatible PECVD silicon nitride waveguides and grating couplers for blue light optogenetic applications*. IEEE Photonics Journal, 2016. **8**(5): p. 1-11.
54. Ozaki, Y. and S. Kawata, *Far-and Deep-ultraviolet spectroscopy*. 2015: Springer.
55. Nissen, M., et al., *UV absorption spectroscopy in water-filled antiresonant hollow core fibers for pharmaceutical detection*. Sensors, 2018. **18**(2): p. 478.

56. Krischek, R., et al., *Ultraviolet enhancement cavity for ultrafast nonlinear optics and high-rate multiphoton entanglement experiments*. Nature Photonics, 2010. **4**(3): p. 170-173.
57. Soltani, M., et al., *AlGa_N/AlN integrated photonics platform for the ultraviolet and visible spectral range*. Optics express, 2016. **24**(22): p. 25415-25423.
58. Zhang, M., et al., *Monolithic ultra-high-Q lithium niobate microring resonator*. Optica, 2017. **4**(12): p. 1536-1537.
59. Kong, Y., et al., *Recent progress in lithium niobate: optical damage, defect simulation, and on-chip devices*. Advanced Materials, 2020. **32**(3): p. 1806452.
60. Lu, T.-J., et al., *Aluminum nitride integrated photonics platform for the ultraviolet to visible spectrum*. Optics express, 2018. **26**(9): p. 11147-11160.
61. Karunagaran, B., et al., *Effect of rapid thermal annealing on the properties of PECVD Si_Nx thin films*. Materials Chemistry and Physics, 2007. **106**(1): p. 130-133.
62. Slack, G.A., et al., *The intrinsic thermal conductivity of AlN*. Journal of Physics and Chemistry of Solids, 1987. **48**(7): p. 641-647.
63. Watanabe, N., T. Kimoto, and J. Suda, *The temperature dependence of the refractive indices of GaN and AlN from room temperature up to 515 C*. 2008, American Institute of Physics.
64. Xiong, C., W.H. Pernice, and H.X. Tang, *Low-loss, silicon integrated, aluminum nitride photonic circuits and their use for electro-optic signal processing*. Nano letters, 2012. **12**(7): p. 3562-3568.
65. Gräupner, P., et al., *Electro-optical effect in aluminum nitride waveguides*. Journal of applied physics, 1992. **71**(9): p. 4136-4139.
66. Dogheche, E., et al., *Growth and optical characterization of aluminum nitride thin films deposited on silicon by radio-frequency sputtering*. Applied physics letters, 1999. **74**(9): p. 1209-1211.
67. Majkić, A., et al., *Optical nonlinear and electro-optical coefficients in bulk aluminium nitride single crystals*. physica status solidi (b), 2017. **254**(9): p. 1700077.
68. Jiang, H. and J. Singh, *Linear electro-optic effect due to the built-in electric field in InGa_N/Ga_N quantum wells*. Applied physics letters, 1999. **75**(13): p. 1932-1934.
69. Miragliotta, J., et al., *Linear-and nonlinear-optical properties of Ga_N thin films*. JOSA B, 1993. **10**(8): p. 1447-1456.
70. Miragliotta, J. and D. Wickenden, *Nonlinear electroreflectance from gallium nitride using optical second-harmonic generation*. Physical Review B, 1996. **53**(3): p. 1388.
71. Jiang, W., et al., *Electro-optic Coefficient Enhancement of Al_xGa_{1-x}N via Multiple Field Modulations*. ACS applied materials & interfaces, 2015. **7**(32): p. 17707-17712.
72. Chen, P., et al., *Enhanced Pockels effect in Ga_N/Al_xGa_{1-x}N superlattice measured by polarization-maintaining fiber Mach-Zehnder interferometer*. Applied Physics Letters, 2007. **91**(3): p. 031103.
73. Long, X.C., et al., *GaN linear electro-optic effect*. Applied physics letters, 1995. **67**(10): p. 1349-1351.
74. Yonekura, K., L. Jin, and K. Takizawa, *Measurement of dispersion of effective electro-optic coefficients r_{13E} and r_{33E} of non-doped congruent LiNbO₃ crystal*. Japanese Journal of Applied Physics, 2008. **47**(7R): p. 5503.

75. Nakano, S., K. Akiyama, and I. Shoji, *Accurate measurement of electro-optic coefficients of undoped and MgO-doped stoichiometric LiNbO₃*. *Optical Materials Express*, 2017. **7**(3): p. 939-944.
76. Arizmendi, L., *Photonic applications of lithium niobate crystals*. *physica status solidi (a)*, 2004. **201**(2): p. 253-283.
77. Sones, C., et al., *Spectral and electro-optic response of UV-written waveguides in LiNbO₃ single crystals*. *Optics express*, 2009. **17**(26): p. 23755-23764.
78. Méndez, A., et al., *Wavelength dependence of electro-optic coefficients in congruent and quasistoichiometric LiNbO₃*. *Electronics Letters*, 1999. **35**(6): p. 498-499.
79. Sánchez-Dena, O., et al., *Lithium Niobate Single Crystals and Powders Reviewed—Part I. Crystals*, 2020. **10**(11): p. 973.
80. Fujiwara, T., et al., *Comparison of electro-optic effect between stoichiometric and congruent LiNbO₃*. *Electronics letters*, 1999. **35**(6): p. 499-501.
81. De Toro, J., et al., *Accurate interferometric measurement of electro-optic coefficients: application to quasi-stoichiometric LiNbO₃*. *Optics communications*, 1998. **154**(1-3): p. 23-27.
82. Soltani, M., *Novel integrated silicon nanophotonic structures using ultra-high Q resonators*. 2009, Georgia Institute of Technology.
83. Pandey, A., et al., *High-efficiency AlGaIn/GaN/AlGaIn tunnel junction ultraviolet light-emitting diodes*. *Photonics Research*, 2020. **8**(3): p. 331-337.
84. Shin, W., et al., *Photonic crystal tunnel junction deep ultraviolet light emitting diodes with enhanced light extraction efficiency*. *Optics express*, 2019. **27**(26): p. 38413-38420.
85. Sun, Y., et al., *Ultrahigh Q microring resonators using a single-crystal aluminum-nitride-on-sapphire platform*. *Optics letters*, 2019. **44**(23): p. 5679-5682.
86. Shin, W., et al., *Demonstration of green and UV wavelength high Q aluminum nitride on sapphire microring resonators integrated with microheaters*. *Applied Physics Letters*, 2021. **118**(21): p. 211103.
87. Amar, J.G. and F. Family, *Critical cluster size: Island morphology and size distribution in submonolayer epitaxial growth*. *MRS Online Proceedings Library (OPL)*, 1994. **367**.
88. McCray, W.P., *MBE deserves a place in the history books*. *Nature nanotechnology*, 2007. **2**(5): p. 259-261.
89. Singh, J., et al., *Role of kinetics and thermodynamics in alloy clustering and surface quality in InAlAs grown by molecular-beam epitaxy: Consequences for optical and transport properties*. *Journal of applied physics*, 1986. **60**(9): p. 3167-3171.
90. <https://www.staibinstruments.com/products/rheed/>.
91. [https://www.staibinstruments.com/products/rheed/#iLightbox\[image_carousel_1\]/0](https://www.staibinstruments.com/products/rheed/#iLightbox[image_carousel_1]/0).
92. *Excitation of Photoluminescence*. Available from: <https://ned.ipac.caltech.edu/level5/Sept03/Li/frames.html>.
93. Hilfiker, J., *In situ spectroscopic ellipsometry (SE) for characterization of thin film growth*, in *In situ characterization of thin film growth*. 2011, Elsevier. p. 99-151.
94. *X-Ray Diffraction*. Available from: <https://www.veqter.co.uk/residual-stress-measurement/x-ray-diffraction>.
95. *WHO Guidelines Approved by the Guidelines Review Committee*, in *Global Guidelines for the Prevention of Surgical Site Infection*. 2018, World Health Organization: Geneva.

96. WHO Guidelines Approved by the Guidelines Review Committee, in *Guidelines for Drinking-Water Quality: Fourth Edition Incorporating the First Addendum*. 2017, World Health Organization: Geneva.
97. Shakya, J., et al., *Polarization of III-nitride blue and ultraviolet light-emitting diodes*. Applied Physics Letters, 2005. **86**(9): p. 091107.
98. Zhao, P., et al., *Analysis of TM mode light extraction efficiency enhancement for deep ultraviolet AlGaIn quantum wells light-emitting diodes with III-nitride micro-domes*. Optical Materials Express, 2012. **2**(10): p. 1397-1406.
99. Guttman, M., et al., *Optical light polarization and light extraction efficiency of AlGaIn-based LEDs emitting between 264 and 220 nm*. Japanese Journal of Applied Physics, 2019. **58**(SC): p. SCCB20.
100. Northrup, J., et al., *Effect of strain and barrier composition on the polarization of light emission from AlGaIn/AlN quantum wells*. Applied Physics Letters, 2012. **100**(2): p. 021101.
101. Hirayama, H., et al., *222–282 nm AlGaIn and InAlGaIn-based deep-UV LEDs fabricated on high-quality AlN on sapphire*. physica status solidi (a), 2009. **206**(6): p. 1176-1182.
102. Nakarmi, M., et al., *Correlation between optical and electrical properties of Mg-doped AlN epilayers*. Applied Physics Letters, 2006. **89**(15): p. 152120.
103. Taniyasu, Y., M. Kasu, and T. Makimoto, *An aluminium nitride light-emitting diode with a wavelength of 210 nanometres*. Nature, 2006. **441**(7091): p. 325.
104. Stampfl, C. and C. Van de Walle, *Theoretical investigation of native defects, impurities, and complexes in aluminum nitride*. Physical Review B, 2002. **65**(15): p. 155212.
105. Mymrin, V., et al., *Bandgap engineering of electronic and optoelectronic devices on native AlN and GaN substrates: A modelling insight*. Journal of Crystal Growth, 2005. **281**(1): p. 115-124.
106. Shur, M.S. and R. Gaska, *Deep-ultraviolet light-emitting diodes*. IEEE Transactions on Electron Devices, 2009. **57**(1): p. 12-25.
107. Kashima, Y., et al., *High external quantum efficiency (10%) AlGaIn-based deep-ultraviolet light-emitting diodes achieved by using highly reflective photonic crystal on p-AlGaIn contact layer*. Applied Physics Express, 2018. **11**(1).
108. Djavid, M. and Z. Mi, *Enhancing the light extraction efficiency of AlGaIn deep ultraviolet light emitting diodes by using nanowire structures*. Applied Physics Letters, 2016. **108**(5): p. 051102.
109. Liu, X., et al., *Improving the efficiency of transverse magnetic polarized emission from AlGaIn based LEDs by using nanowire photonic crystal*. IEEE Photonics Journal, 2018. **10**(4): p. 1-11.
110. Zhao, S., et al., *III-Nitride nanowire optoelectronics*. Progress in Quantum Electronics, 2015. **44**: p. 14-68.
111. Dong, P., et al., *282-nm AlGaIn-based deep ultraviolet light-emitting diodes with improved performance on nano-patterned sapphire substrates*. Applied Physics Letters, 2013. **102**(24): p. 241113.
112. Hirayama, H., et al., *231–261 nm AlGaIn deep-ultraviolet light-emitting diodes fabricated on AlN multilayer buffers grown by ammonia pulse-flow method on sapphire*. Applied Physics Letters, 2007. **91**(7): p. 071901.
113. Susilo, N., et al., *AlGaIn-based deep UV LEDs grown on sputtered and high temperature annealed AlN/sapphire*. Applied Physics Letters, 2018. **112**(4): p. 041110.

114. Zhang, J., et al., *AlGa_N-based 280 nm light-emitting diodes with continuous-wave power exceeding 1 mW at 25 mA*. Applied Physics Letters, 2004. **85**(23): p. 5532-5534.
115. Vilhunen, S., H. Särkkä, and M. Sillanpää, *Ultraviolet light-emitting diodes in water disinfection*. Environmental Science and Pollution Research, 2009. **16**(4): p. 439-442.
116. Inoue, S.-i., et al., *Light extraction enhancement of 265 nm deep-ultraviolet light-emitting diodes with over 90 mW output power via an AlN hybrid nanostructure*. Applied Physics Letters, 2015. **106**(13): p. 131104.
117. Inoue, S.-i., N. Tamari, and M. Taniguchi, *150 mW deep-ultraviolet light-emitting diodes with large-area AlN nanophotonic light-extraction structure emitting at 265 nm*. Applied Physics Letters, 2017. **110**(14): p. 141106.
118. Hao, G.-D., et al., *Electrical determination of current injection and internal quantum efficiencies in AlGa_N-based deep-ultraviolet light-emitting diodes*. Optics Express, 2017. **25**(16): p. A639-A648.
119. Liao, Y., et al., *Recent progress of efficient deep UV-LEDs by plasma-assisted molecular beam epitaxy*. Physica Status Solidi (c), 2012. **9**(3-4): p. 798-801.
120. Lin, G.-B., et al., *Analytic model for the efficiency droop in semiconductors with asymmetric carrier-transport properties based on drift-induced reduction of injection efficiency*. Applied Physics Letters, 2012. **100**(16): p. 161106.
121. Hirayama, H., et al., *Marked enhancement in the efficiency of deep-ultraviolet AlGa_N light-emitting diodes by using a multiquantum-barrier electron blocking layer*. Applied Physics Express, 2010. **3**(3): p. 031002.
122. Zhang, J., et al., *Influence of pulse width on electroluminescence and junction temperature of AlInGa_N deep ultraviolet light-emitting diodes*. Applied Physics Letters, 2008. **92**(19): p. 191917.
123. Chitnis, A., et al., *Self-heating effects at high pump currents in deep ultraviolet light-emitting diodes at 324 nm*. Applied Physics Letters, 2002. **81**(18): p. 3491-3493.
124. Yun, J., J.-I. Shim, and H. Hirayama, *Analysis of efficiency droop in 280-nm AlGa_N multiple-quantum-well light-emitting diodes based on carrier rate equation*. Applied Physics Express, 2015. **8**(2): p. 022104.
125. Sun, W., et al., *Efficiency droop in 245–247 nm AlGa_N light-emitting diodes with continuous wave 2 mW output power*. Applied Physics Letters, 2010. **96**(6): p. 061102.
126. Maeda, N., M. Jo, and H. Hirayama, *Improving the Efficiency of AlGa_N Deep-UV LEDs by Using Highly Reflective Ni/Al p-Type Electrodes*. Physica Status Solidi (a), 2018. **215**(8): p. 1700435.
127. Zhang, Y., et al., *Tunnel-injected sub 290 nm ultra-violet light emitting diodes with 2.8% external quantum efficiency*. Applied Physics Letters, 2018. **112**(7): p. 071107.
128. Zhang, Y., et al., *Tunnel-injected sub-260 nm ultraviolet light emitting diodes*. Applied Physics Letters, 2017. **110**(20): p. 201102.
129. Akyol, F., et al., *Low-resistance Ga_N tunnel homojunctions with 150 kA/cm² current and repeatable negative differential resistance*. Applied Physics Letters, 2016. **108**(13): p. 131103.
130. Clinton, E.A., et al., *Negative differential resistance in Ga_N homojunction tunnel diodes and low voltage loss tunnel contacts*. Applied Physics Letters, 2018. **112**(25): p. 252103.
131. Jeon, S.-R., et al., *Lateral current spreading in Ga_N-based light-emitting diodes utilizing tunnel contact junctions*. Applied Physics Letters, 2001. **78**(21): p. 3265-3267.

132. Zhang, Z.-H., et al., *InGaN/GaN light-emitting diode with a polarization tunnel junction*. Applied Physics Letters, 2013. **102**(19): p. 193508.
133. Diagne, M., et al., *Vertical cavity violet light emitting diode incorporating an aluminum gallium nitride distributed Bragg mirror and a tunnel junction*. Applied Physics Letters, 2001. **79**(22): p. 3720-3722.
134. Takeuchi, T., et al., *GaN-based light emitting diodes with tunnel junctions*. Japanese Journal of Applied Physics, 2001. **40**(8B): p. L861.
135. Lee, S., et al., *GaN-based vertical-cavity surface-emitting lasers with tunnel junction contacts grown by metal-organic chemical vapor deposition*. Applied Physics Express, 2018. **11**(6): p. 062703.
136. Zhang, Y., et al., *Design of p-type cladding layers for tunnel-injected UV-A light emitting diodes*. Applied Physics Letters, 2016. **109**(19): p. 191105.
137. Kuhn, C., et al., *MOVPE-grown AlGaIn-based tunnel heterojunctions enabling fully transparent UVC LEDs*. Photonics Research, 2019. **7**(5): p. B7-B11.
138. Zhang, Y., et al., *Design and demonstration of ultra-wide bandgap AlGaIn tunnel junctions*. Applied Physics Letters, 2016. **109**(12): p. 121102.
139. Auf der Maur, M., et al., *Trap-assisted tunneling in InGaIn/GaN single-quantum-well light-emitting diodes*. Applied Physics Letters, 2014. **105**(13): p. 133504.
140. Cao, X., et al., *Diffusion and tunneling currents in GaIn/InGaIn multiple quantum well light-emitting diodes*. IEEE Electron Device Letters, 2002. **23**(9): p. 535-537.
141. Bayram, C., Z. Vashaei, and M. Razeghi, *Reliability in room-temperature negative differential resistance characteristics of low-aluminum content AlGaIn/GaN double-barrier resonant tunneling diodes*. Applied Physics Letters, 2010. **97**(18): p. 181109.
142. Fan Arcara, V., et al., *Ge doped GaIn and AlO₃ GaIn_{0.5}N_{0.5}-based tunnel junctions on top of visible and UV light emitting diodes*. Journal of Applied Physics, 2019. **126**(22): p. 224503.
143. Vadiiee, E., et al., *InGaIn solar cells with regrown GaIn homojunction tunnel contacts*. Applied Physics Express, 2018. **11**(8): p. 082304.
144. Young, E.C., et al., *Hybrid tunnel junction contacts to III–nitride light-emitting diodes*. Applied Physics Express, 2016. **9**(2): p. 022102.
145. Lee, Y.-J., C.-H. Chen, and C.-J. Lee, *Reduction in the efficiency-droop effect of InGaIn green light-emitting diodes using gradual quantum wells*. IEEE Photonics Technology Letters, 2010. **22**(20): p. 1506-1508.
146. Piprek, J., *Efficiency droop in nitride-based light-emitting diodes*. Physica Status Solidi (a), 2010. **207**(10): p. 2217-2225.
147. Kim, M.-H., et al., *Origin of efficiency droop in GaIn-based light-emitting diodes*. Applied Physics Letters, 2007. **91**(18): p. 183507.
148. Kioupakis, E., et al., *Indirect Auger recombination as a cause of efficiency droop in nitride light-emitting diodes*. Applied Physics Letters, 2011. **98**(16): p. 161107.
149. Hai, X., et al., *Effect of low hole mobility on the efficiency droop of AlGaIn nanowire deep ultraviolet light emitting diodes*. Applied Physics Letters, 2019. **114**(10): p. 101104.
150. Meyaard, D.S., et al., *Asymmetry of carrier transport leading to efficiency droop in GaInN based light-emitting diodes*. Applied Physics Letters, 2011. **99**(25): p. 251115.
151. Tran, N.H., et al., *On the mechanism of highly efficient p-type conduction of Mg-doped ultra-wide-bandgap AlN nanostructures*. Applied Physics Letters, 2017. **110**(3): p. 032102.

152. Collazo, R., et al., *Progress on n-type doping of AlGa_N alloys on AlN single crystal substrates for UV optoelectronic applications*. *physica status solidi (c)*, 2011. **8**(7-8): p. 2031-2033.
153. Liu, X., et al., *Charge carrier transport properties of Mg-doped Al_{0.6}Ga_{0.4}N grown by molecular beam epitaxy*. *Semiconductor Science and Technology*, 2018. **33**(8): p. 085005.
154. Bhattacharyya, A., et al., *Deep ultraviolet emitting AlGa_N quantum wells with high internal quantum efficiency*. *Applied Physics Letters*, 2009. **94**(18): p. 181907.
155. Liao, Y., et al., *AlGa_N based deep ultraviolet light emitting diodes with high internal quantum efficiency grown by molecular beam epitaxy*. *Applied Physics Letters*, 2011. **98**(8): p. 081110.
156. Wang, Y., et al., *Complex and incommensurate ordering in Al_{0.72}Ga_{0.28}N thin films grown by plasma-assisted molecular beam epitaxy*. *Applied physics letters*, 2006. **88**(18): p. 181915.
157. Ambacher, O., et al., *Two dimensional electron gases induced by spontaneous and piezoelectric polarization in undoped and doped AlGa_N/Ga_N heterostructures*. *Journal of Applied Physics*, 2000. **87**(1): p. 334-344.
158. Gu, Y., et al. *Spectral and luminous efficacy change of high-power LEDs under different dimming methods*. in *Sixth International Conference on Solid State Lighting*. 2006. International Society for Optics and Photonics.
159. Cho, J., E.F. Schubert, and J.K. Kim, *Efficiency droop in light-emitting diodes: Challenges and countermeasures*. *Laser Photonics Reviews*, 2013. **7**(3): p. 408-421.
160. Karpov, S., *ABC-model for interpretation of internal quantum efficiency and its droop in III-nitride LEDs: a review*. *Optical Quantum Electronics*, 2015. **47**(6): p. 1293-1303.
161. Nippert, F., et al., *Auger recombination in AlGa_N quantum wells for UV light-emitting diodes*. *Applied Physics Letters*, 2018. **113**(7): p. 071107.
162. Kamiyama, S., et al., *Low-temperature-deposited AlGa_N interlayer for improvement of AlGa_N/Ga_N heterostructure*. *Journal of crystal growth*, 2001. **223**(1-2): p. 83-91.
163. Li, J., et al., *Optical and electrical properties of Mg-doped p-type Al_xGa_{1-x}N*. *Applied physics letters*, 2002. **80**(7): p. 1210-1212.
164. Nakarmi, M., et al., *Electrical and optical properties of Mg-doped Al_{0.7}Ga_{0.3}N alloys*. *Applied Physics Letters*, 2005. **86**(9): p. 092108.
165. Fujita, M., et al., *Simultaneous inhibition and redistribution of spontaneous light emission in photonic crystals*. *Science*, 2005. **308**(5726): p. 1296-1298.
166. Wiesmann, C., et al., *Photonic crystal LEDs—designing light extraction*. *Laser & Photonics Reviews*, 2009. **3**(3): p. 262-286.
167. Shakya, J., et al., *Enhanced light extraction in III-nitride ultraviolet photonic crystal light-emitting diodes*. *Applied Physics Letters*, 2004. **85**(1): p. 142-144.
168. Philip, M.R., et al., *Molecular Beam Epitaxial Growth and Device Characterization of AlGa_N Nanowire Ultraviolet-B Light-Emitting Diodes*. *Journal of advanced optics and photonics*, 2018. **1**(1).
169. Li, K., et al., *Ultralow-threshold electrically injected AlGa_N nanowire ultraviolet lasers on Si operating at low temperature*. *Nature nanotechnology*, 2015. **10**(2): p. 140.
170. Oder, T., et al., *III-nitride blue and ultraviolet photonic crystal light emitting diodes*. *Applied Physics Letters*, 2004. **84**(4): p. 466-468.

171. Oder, T., et al., *III-nitride photonic crystals*. Applied Physics Letters, 2003. **83**(6): p. 1231-1233.
172. Wierer Jr, J.J., A. David, and M.M. Megens, *III-nitride photonic-crystal light-emitting diodes with high extraction efficiency*. Nature Photonics, 2009. **3**(3): p. 163.
173. Kwon, M.-K., et al., *Enhanced emission efficiency of GaN/InGaN multiple quantum well light-emitting diode with an embedded photonic crystal*. Applied Physics Letters, 2008. **92**(25): p. 251110.
174. Kashima, Y., et al., *High external quantum efficiency (10%) AlGaIn-based deep-ultraviolet light-emitting diodes achieved by using highly reflective photonic crystal on p-AlGaIn contact layer*. Applied Physics Express, 2018. **11**(1): p. 012101.
175. Gunning, B., et al., *Negligible carrier freeze-out facilitated by impurity band conduction in highly p-type GaN*. Applied Physics Letters, 2012. **101**(8): p. 082106.
176. Zhang, Y., et al., *Tunnel-injected sub 290 nm ultra-violet light emitting diodes with 2.8% external quantum efficiency*. Applied Physics Letters, 2018. **112**(7): p. 071107.
177. Grundmann, M.J. and U.K. Mishra, *Multi-color light emitting diode using polarization-induced tunnel junctions*. physica status solidi c, 2007. **4**(7): p. 2830-2833.
178. Detchprohm, T., et al., *Sub 250 nm deep-UV AlGaIn/AlN distributed Bragg reflectors*. Applied Physics Letters, 2017. **110**(1): p. 011105.
179. Bérenger, J.-P., *Perfectly matched layer (PML) for computational electromagnetics*. Synthesis Lectures on Computational Electromagnetics, 2007. **2**(1): p. 1-117.
180. Gedney, S.D., *An anisotropic perfectly matched layer-absorbing medium for the truncation of FDTD lattices*. IEEE transactions on Antennas and Propagation, 1996. **44**(12): p. 1630-1639.
181. Zhao, P. and H. Zhao, *Analysis of light extraction efficiency enhancement for thin-film-flip-chip InGaIn quantum wells light-emitting diodes with GaIn micro-domes*. Optics express, 2012. **20**(105): p. A765-A776.
182. Iveland, J., et al., *Direct measurement of Auger electrons emitted from a semiconductor light-emitting diode under electrical injection: identification of the dominant mechanism for efficiency droop*. Physical review letters, 2013. **110**(17): p. 177406.
183. De Santi, C., et al., *Recombination mechanisms and thermal droop in AlGaIn-based UV-B LEDs*. Photonics Research, 2017. **5**(2): p. A44-A51.
184. Xiong, C., et al., *Aluminum nitride as a new material for chip-scale optomechanics and nonlinear optics*. New Journal of Physics, 2012. **14**(9): p. 095014.
185. Liu, X., et al., *Broadband tunable microwave photonic phase shifter with low RF power variation in a high-Q AlN microring*. Optics letters, 2016. **41**(15): p. 3599-3602.
186. Liu, X., et al., *Aluminum nitride-on-sapphire platform for integrated high-Q microresonators*. Optics express, 2017. **25**(2): p. 587-594.
187. Bruch, A.W., et al., *17 000%/W second-harmonic conversion efficiency in single-crystalline aluminum nitride microresonators*. Applied Physics Letters, 2018. **113**(13): p. 131102.
188. Liu, X., et al., *Generation of multiple near-visible comb lines in an AlN microring via χ (2) and χ (3) optical nonlinearities*. Applied Physics Letters, 2018. **113**(17): p. 171106.
189. Liu, X., et al., *Integrated high-Q crystalline AlN microresonators for broadband Kerr and Raman frequency combs*. ACS Photonics, 2018. **5**(5): p. 1943-1950.

190. Pernice, W.H., C. Xiong, and H.X. Tang, *High Q micro-ring resonators fabricated from polycrystalline aluminum nitride films for near infrared and visible photonics*. Optics express, 2012. **20**(11): p. 12261-12269.
191. Jung, H., et al., *Optical frequency comb generation from aluminum nitride microring resonator*. Optics letters, 2013. **38**(15): p. 2810-2813.
192. Pernice, W., et al., *Second harmonic generation in phase matched aluminum nitride waveguides and micro-ring resonators*. Applied Physics Letters, 2012. **100**(22): p. 223501.
193. Xiong, C., et al., *Integrated high frequency aluminum nitride optomechanical resonators*. Applied Physics Letters, 2012. **100**(17): p. 171111.
194. Fujii, Y., et al., *Nonlinear optical susceptibilities of AlN film*. Applied Physics Letters, 1977. **31**(12): p. 815-816.
195. Guo, X., et al., *On-chip strong coupling and efficient frequency conversion between telecom and visible optical modes*. Physical review letters, 2016. **117**(12): p. 123902.
196. Liu, X., et al., *Integrated continuous-wave aluminum nitride Raman laser*. Optica, 2017. **4**(8): p. 893-896.
197. Troha, T., et al., *UV second harmonic generation in AlN waveguides with modal phase matching*. Optical Materials Express, 2016. **6**(6): p. 2014-2023.
198. Jung, H. and H.X. Tang, *Aluminum nitride as nonlinear optical material for on-chip frequency comb generation and frequency conversion*. Nanophotonics, 2016. **5**(2): p. 263-271.
199. Guo, X., et al., *Parametric down-conversion photon-pair source on a nanophotonic chip*. Light: Science & Applications, 2017. **6**(5): p. e16249-e16249.
200. Lin, P.T., et al., *Low-loss aluminium nitride thin film for mid-infrared microphotonics*. Laser & Photonics Reviews, 2014. **8**(2): p. L23-L28.
201. Stegmaier, M., et al., *Aluminum nitride nanophotonic circuits operating at ultraviolet wavelengths*. Applied Physics Letters, 2014. **104**(9): p. 091108.
202. Lueng, C., et al., *Piezoelectric coefficient of aluminum nitride and gallium nitride*. Journal of applied physics, 2000. **88**(9): p. 5360-5363.
203. Chen, H., et al., *Study of crystalline defect induced optical scattering loss inside photonic waveguides in UV-visible spectral wavelengths using volume current method*. Optics express, 2019. **27**(12): p. 17262-17273.
204. Jung, H., et al., *Green, red, and IR frequency comb line generation from single IR pump in AlN microring resonator*. Optica, 2014. **1**(6): p. 396-399.
205. Liu, X., et al., *Ultra-high-Q UV microring resonators based on a single-crystalline AlN platform*. Optica, 2018. **5**(10): p. 1279-1282.
206. Feng, M., et al., *On-chip integration of GaN-based laser, modulator, and photodetector grown on Si*. IEEE Journal of Selected Topics in Quantum Electronics, 2018. **24**(6): p. 1-5.
207. Cai, W., et al., *On-chip integration of suspended InGaN/GaN multiple-quantum-well devices with versatile functionalities*. Optics express, 2016. **24**(6): p. 6004-6010.
208. Zhang, L., et al., *High-quality AlN epitaxy on nano-patterned sapphire substrates prepared by nano-imprint lithography*. Scientific reports, 2016. **6**(1): p. 1-8.
209. Miyake, H., et al., *Preparation of high-quality AlN on sapphire by high-temperature face-to-face annealing*. Journal of Crystal Growth, 2016. **456**: p. 155-159.

210. Hosseini, E.S., et al., *Systematic design and fabrication of high-Q single-mode pulley-coupled planar silicon nitride microdisk resonators at visible wavelengths*. Optics express, 2010. **18**(3): p. 2127-2136.
211. Soltani, M., S. Yegnanarayanan, and A. Adibi, *Ultra-high Q planar silicon microdisk resonators for chip-scale silicon photonics*. Optics express, 2007. **15**(8): p. 4694-4704.
212. Chang, C., T. Abe, and M. Esashi, *Trench filling characteristics of low stress TEOS/ozone oxide deposited by PECVD and SACVD*. Microsystem technologies, 2004. **10**(2): p. 97-102.
213. Liu, X., et al. *Improvement of thermal properties in epitaxial aluminum nitride pedestal microring*. in *2015 14th International Conference on Optical Communications and Networks (ICOON)*. 2015. IEEE.
214. Luke, K., et al., *Wafer-scale low-loss lithium niobate photonic integrated circuits*. Optics Express, 2020. **28**(17): p. 24452-24458.
215. Desiatov, B., et al., *Ultra-low-loss integrated visible photonics using thin-film lithium niobate*. Optica, 2019. **6**(3): p. 380-384.
216. Wang, C., et al., *Nanophotonic lithium niobate electro-optic modulators*. Optics express, 2018. **26**(2): p. 1547-1555.
217. Hermans, A., et al., *Integrated silicon nitride electro-optic modulators with atomic layer deposited overlays*. Optics letters, 2019. **44**(5): p. 1112-1115.
218. Sorace-Agaskar, C., et al. *Multi-layer integrated photonics from the ultraviolet to the infrared*. in *Frontiers in Biological Detection: From Nanosensors to Systems X*. 2018. International Society for Optics and Photonics.
219. Van Emmerik, C.I., et al., *Single-layer active-passive Al₂O₃ photonic integration platform*. Optical materials express, 2018. **8**(10): p. 3049-3054.
220. West, G.N., et al., *Low-loss integrated photonics for the blue and ultraviolet regime*. APL Photonics, 2019. **4**(2): p. 026101.
221. Evans, C.C., C. Liu, and J. Suntivich, *TiO₂ nanophotonic sensors for efficient integrated evanescent Raman spectroscopy*. Acs Photonics, 2016. **3**(9): p. 1662-1669.
222. Lamy, M., et al. *Exploring titanium dioxide as a new photonic platform*. in *European Conference on Integrated Optics*. 2019.
223. Choy, J.T., et al., *Integrated TiO₂ resonators for visible photonics*. Optics letters, 2012. **37**(4): p. 539-541.
224. Mi, S., et al., *Integrated photonic devices in single crystal diamond*. Journal of Physics: Photonics, 2020. **2**(4): p. 042001.
225. Dréau, A., et al., *Quantum frequency conversion of single photons from a nitrogen-vacancy center in diamond to telecommunication wavelengths*. Physical Review Applied, 2018. **9**(6): p. 064031.
226. Lu, T.J., et al., *Aluminum nitride integrated photonics platform for the ultraviolet to visible spectrum*. Opt. Express, 2018. **26**(9): p. 11147-11160.
227. Jiang, W., et al., *Optical anisotropy of AlN epilayer on sapphire substrate investigated by variable-angle spectroscopic ellipsometry*. Optical Materials, 2010. **32**(9): p. 891-895.
228. Shokhovets, S., et al., *Determination of the anisotropic dielectric function for wurtzite AlN and GaN by spectroscopic ellipsometry*. Journal of Applied Physics, 2003. **94**(1): p. 307-312.
229. Xiao, S., et al., *Improvement mechanism of sputtered AlN films by high-temperature annealing*. Journal of Crystal Growth, 2018. **502**: p. 41-44.

230. Watanabe, N., T. Kimoto, and J. Suda, *The temperature dependence of the refractive indices of GaN and AlN from room temperature up to 515 C*. Journal of Applied Physics, 2008. **104**(10).
231. Roland, I., et al., *Phase-matched second harmonic generation with on-chip GaN-on-Si microdisks*. Scientific reports, 2016. **6**(1): p. 1-8.
232. Angerer, W., et al., *Ultrafast second-harmonic generation spectroscopy of GaN thin films on sapphire*. Physical Review B, 1999. **59**(4): p. 2932.
233. Gromovyi, M., et al., *Efficient second harmonic generation in low-loss planar GaN waveguides*. Optics express, 2017. **25**(19): p. 23035-23044.
234. Xiong, C., et al., *Integrated GaN photonic circuits on silicon (100) for second harmonic generation*. Optics express, 2011. **19**(11): p. 10462-10470.
235. Petris, A., et al., *Ultrafast Third-Order Nonlinear Optical Response Excited by fs Laser Pulses at 1550 nm in GaN Crystals*. Materials, 2021. **14**(12): p. 3194.
236. Munk, D., et al., *Four-wave mixing and nonlinear parameter measurement in a gallium-nitride ridge waveguide*. Optical Materials Express, 2018. **8**(1): p. 66-72.
237. Liu, S., et al., *Design of mid-infrared electro-optic modulators based on aluminum nitride waveguides*. Journal of Lightwave Technology, 2016. **34**(16): p. 3837-3842.
238. Liu, J., et al., *Photolithography allows high-Q AlN microresonators for near octave-spanning frequency comb and harmonic generation*. Optics Express, 2020. **28**(13): p. 19270-19280.
239. Liu, X., et al., *Aluminum nitride nanophotonics for beyond-octave soliton microcomb generation and self-referencing*. Nature communications, 2021. **12**(1): p. 1-7.
240. Ullah, F., N. Deng, and F. Qiu, *Recent progress in electro-optic polymer for ultra-fast communication*. Photonix, 2021. **2**(1): p. 1-18.
241. Shi, Z., et al., *Achieving excellent electro-optic activity and thermal stability in poled polymers through an expeditious crosslinking process*. Journal of Materials Chemistry, 2012. **22**(3): p. 951-959.
242. Shi, Z., et al., *Dipolar chromophore facilitated huisgen cross-linking reactions for highly efficient and thermally stable electrooptic polymers*. ACS Macro Letters, 2012. **1**(7): p. 793-796.
243. Liu, J., et al., *Synthesis of novel polyarylate with electrooptical chromophores as side chain as electro-optic host polymer*. Colloid and Polymer Science, 2012. **290**(12): p. 1215-1220.
244. Lee, S.H., et al., *A novel method for measuring continuous dispersion spectrum of electro-optic coefficients of nonlinear materials*. Optics express, 2009. **17**(12): p. 9828-9833.
245. Bernardini, F. and V. Fiorentini, *Macroscopic polarization and band offsets at nitride heterojunctions*. Physical Review B, 1998. **57**(16): p. R9427.
246. Borghi, M., et al., *Homodyne detection of free carrier induced electro-optic modulation in strained silicon resonators*. Journal of Lightwave Technology, 2016. **34**(24): p. 5657-5668.
247. Castellan, C., et al., *Field-induced nonlinearities in silicon waveguides embedded in lateral pn junctions*. Frontiers in Physics, 2019. **7**: p. 104.
248. Damas, P., et al., *Wavelength dependence of Pockels effect in strained silicon waveguides*. Optics express, 2014. **22**(18): p. 22095-22100.

249. Izdebski, M., W. Kucharczyk, and R. Raab, *On relationships between electro-optic coefficients for impermeability and nonlinear electric susceptibilities*. Journal of Optics A: Pure and Applied Optics, 2004. **6**(4): p. 421.
250. Sharma, R., et al., *Characterizing the effects of free carriers in fully etched, dielectric-clad silicon waveguides*. Applied Physics Letters, 2015. **106**(24): p. 241104.
251. Sharma, R., et al., *Effect of dielectric claddings on the electro-optic behavior of silicon waveguides*. Optics letters, 2016. **41**(6): p. 1185-1188.
252. Pandey, A., et al., *Electron overflow of AlGaIn deep ultraviolet light emitting diodes*. Applied Physics Letters, 2021. **118**(24): p. 241109.
253. Lu, X., et al., *Chip-integrated visible–telecom entangled photon pair source for quantum communication*. Nature physics, 2019. **15**(4): p. 373-381.
254. Sinclair, M., et al., *1.4 million Q factor Si₃N₄ micro-ring resonator at 780 nm wavelength for chip-scale atomic systems*. Optics express, 2020. **28**(3): p. 4010-4020.
255. Tien, M.-C., et al., *Ultra-high quality factor planar Si₃N₄ ring resonators on Si substrates*. Optics express, 2011. **19**(14): p. 13551-13556.
256. Gruhler, N., et al., *High-quality Si₃N₄ circuits as a platform for graphene-based nanophotonic devices*. Optics Express, 2013. **21**(25): p. 31678-31689.
257. Desiatov, B., et al. *Ultra-Low Loss Integrated Lithium Niobate Photonics in Visible Wavelengths*. in *CLEO: Science and Innovations*. 2019. Optical Society of America.
258. Wu, R., et al., *Lithium niobate micro-disk resonators of quality factors above 10⁷*. Optics letters, 2018. **43**(17): p. 4116-4119.
259. Fang, Z., et al., *Real-time electrical tuning of an optical spring on a monolithically integrated ultrahigh Q lithium niobate microresonator*. Optics letters, 2019. **44**(5): p. 1214-1217.
260. Wang, C., et al., *Integrated high quality factor lithium niobate microdisk resonators*. Optics express, 2014. **22**(25): p. 30924-30933.
261. Zhou, Z. and S. Zhang, *Electro-optically tunable racetrack dual microring resonator with a high quality factor based on a lithium niobate-on-insulator*. Optics Communications, 2020. **458**: p. 124718.
262. Zhang, J., et al., *Fabrication of crystalline microresonators of high quality factors with a controllable wedge angle on lithium niobate on insulator*. Nanomaterials, 2019. **9**(9): p. 1218.
263. Kim, Y., et al., *Parametric optimization of depletion-type Si micro-ring modulator performances*. Japanese Journal of Applied Physics, 2019. **58**(6): p. 062006.
264. Jung, H., et al., *Electrical tuning and switching of an optical frequency comb generated in aluminum nitride microring resonators*. Optics letters, 2014. **39**(1): p. 84-87.
265. Kippenberg, T.J., et al., *Dissipative Kerr solitons in optical microresonators*. Science, 2018. **361**(6402).
266. Hausmann, B., et al., *Diamond nonlinear photonics*. Nature Photonics, 2014. **8**(5): p. 369-374.
267. Gong, Z., et al., *High-fidelity cavity soliton generation in crystalline AlN micro-ring resonators*. Optics letters, 2018. **43**(18): p. 4366-4369.
268. Herr, T., et al., *Temporal solitons in optical microresonators*. Nature Photonics, 2014. **8**(2): p. 145-152.

269. Godey, C., et al., *Stability analysis of the spatiotemporal Lugiato-Lefever model for Kerr optical frequency combs in the anomalous and normal dispersion regimes*. Physical Review A, 2014. **89**(6): p. 063814.
270. Bao, C., et al., *Direct soliton generation in microresonators*. Optics letters, 2017. **42**(13): p. 2519-2522.
271. Li, Q., et al., *Stably accessing octave-spanning microresonator frequency combs in the soliton regime*. Optica, 2017. **4**(2): p. 193-203.
272. Brasch, V., et al., *Bringing short-lived dissipative Kerr soliton states in microresonators into a steady state*. Optics express, 2016. **24**(25): p. 29312-29320.
273. Brasch, V., et al., *Photonic chip-based optical frequency comb using soliton Cherenkov radiation*. Science, 2016. **351**(6271): p. 357-360.
274. Guo, H., et al., *Universal dynamics and deterministic switching of dissipative Kerr solitons in optical microresonators*. Nature Physics, 2017. **13**(1): p. 94-102.
275. Joshi, C., et al., *Thermally controlled comb generation and soliton modelocking in microresonators*. Optics letters, 2016. **41**(11): p. 2565-2568.
276. Moille, G., et al., *Kerr-microresonator soliton frequency combs at cryogenic temperatures*. Physical review applied, 2019. **12**(3): p. 034057.
277. Ra, Y.H., et al., *Scalable nanowire photonic crystals: Molding the light emission of InGaN*. Advanced Functional Materials, 2017. **27**(38): p. 1702364.